EXPERIMENTAL AND NUMERICAL INVESTIGATION OF THE THERMAL PERFORMANCE OF THE GAS-COOLED DIVERTOR PLATE CONCEPT

A Thesis
Presented to
The Academic Faculty

by

Elisabeth Faye Gayton

In Partial Fulfillment
of the Requirements for the Degree
Master of Science in Nuclear Engineering

Georgia Institute of Technology

December 2008

EXPERIMENTAL AND NUMERICAL INVESTIGATION OF THE THERMAL PERFORMANCE OF THE GAS-COOLED DIVERTOR PLATE CONCEPT

Approved by:

Dr. Said I. Abdel-Khalik, Advisor
School of Mechanical Engineering
Georgia Institute of Technology

Dr. Minami Yoda, Co-Advisor
School of Mechanical Engineering
Georgia Institute of Technology

Dr. S. Mostafa Ghiaasiaan
School of Mechanical Engineering
Georgia Institute of Technology

Date Approved: November 13, 2008

To my amazing mom Faye Gayton
&
My wonderful fiancé T. J. Dunn

I love you with all my heart.
Thank you for your love, prayers,
and unconditional support.

ACKNOWLEDGEMENTS

First and foremost, I would like to thank my advisors, Dr. Said Abdel-Khalik and Dr. Minami Yoda for their support, advice, and encouragement. I feel extremely privileged to have worked in such close corners with these brilliant scholars. I would also like to thank Dr. Mostafa Ghiaasiaan for his time and contributions to this thesis as a committee member.

A great deal of thanks goes to Mr. Dennis Sadowski for his especially helpful role in designing, fabricating, and instrumenting the test module. I owe everything I know about tools and fittings to him. I would also like to thank my colleague and laboratory partner, Lorenzo Crosatti, who spent many hours teaching me how to setup and run my experiments and numerical calculations. I am extremely grateful for his ability to solve problems and willingness to help. I would also like to thank all of my laboratory colleagues for their assistance and camaraderie: Frank Hope, C.C. Hu, Bo Lu, Jason Horne, and Mitch Hageman.

Above all, I am grateful for the support of my family and my fiancé. Particularly, I would like to thank my mom for all her time, love, and prayers; my Dad for his financial and professional support; and my sister, Mary, for her friendship.

TABLE OF CONTENTS

LIST OF TABLES

LIST OF FIGURES

LIST OF SYMBOLS AND ABBREVIATIONS

A	Area (m^2, mm^2)
A_h	Total area of the holes (m^2, mm^2)
A_{sl}	Area of the slot (m^2, mm^2)
BCs	Boundary Conditions
c	Specific heat (solids) (J/(kg-K))
c_p	Specific heat at constant pressure (J/(kg-K))
CFD	Computational Fluid Dynamics
D	Holes diameter (m, mm)
D_h	Hydraulic diameter of the slot (m, mm)
h_{avg}	Experimental average heat transfer coefficient (W/(m^2-K))
h_{CFD_avg}	Numerical average heat transfer coefficient (W/(m^2-K))
h_{CFD_max}	Numerical peak heat transfer coefficient (W/(m^2-K))
h_{exp}	Experimental local heat transfer coefficient (W/(m^2-K))
HCFP	Helium-cooled flat plate
He	Helium
HTC	Heat transfer coefficient (W/(m^2-K))
k	Thermal conductivity (W/(m-K))
$\dot{m}$	Mass flow rate (g/s)
L	Length (m, mm)
M	Mach number
MFR	Mass flow rate (g/s)
Nu	Nusselt number

Nu_{sg}	Stagnation Nusselt number
ΔP	Pressure drop across the test section (kPa, psi)
$\Delta P'$	Normalized pressure drop across the test section (kPa, psi)
P_{in}	Coolant inlet pressure - gauge (kPa, psi)
P_{nom}	Nominal system pressure (60 psia, 414 kPa)
P_{out}	Coolant outlet pressure - gauge (kPa, psi)
P_{sys}	Coolant system (average) pressure (kPa, psi)
Pr	Prandtl number
PM	Porous medium
Q	Heater power input (W)
q''_{net}	Measured incident heat flux (MW/m^2)
q''_{nom}	Nominal incident heat flux (MW/m^2)
Re	Reynolds number
RNV	RNG k-e, non-equilibrium wall functions, w/ viscous heating
SAVV	Spalart-Allmaras, vorticity-Based Production, w/viscous heating
scfm	"Uncorrected" volume flow rate (ft^3/min)
SNV	Standard k-e, non-equilibrium wall functions, w/ viscous heating
SNVL	Standard k-e, non-equilibrium wall functions, w/ viscous heating, and piece-wise linear air properties
SNVP	Standard k-e, non-equilibrium wall functions, w/ viscous heating, artificially lowered outlet pressure
SS	Stainless steel
SS0	Standard k-e, standard wall functions, no viscous heating

SS0L	Low Pressure, standard k-e, standard wall functions, no viscous heating
SSV	Standard k-e, standard wall functions, w/ viscous heating
SSV2	Standard k-e, standard wall functions, w/ viscous heating, and 2^{nd} order Pressure discretization
SSVP	Standard k-e, standard wall functions, w/ viscous heating, and Pressure Inlet
T	Temperature (^oC)
T_{in}	Coolant inlet temperature (^oC)
T_{out}	Coolant outlet temperature (^oC)
TC	Thermocouple
U	Uncertainty
$\bar{V}$	Average speed (m/s)
W	Slot width (m, mm)

Greek Letters

m	Dynamic viscosity (kg/(m-s))
r	Density (kg/m^3)
s	Standard deviation

Subscripts

avg	Average value
CFD	FLUENT prediction value
exp	Experimentally measured/calculated quantity

f	Film
h	Holes
In	Inlet
max	Maximum
net	Measured (experimental) value
nominal	No heat loss due to convection
Out	Outlet
Sl	Slot

SUMMARY

Experimental and numerical studies simulating the gas-cooled divertor plate design concept have been carried out. While thermo-fluid and thermo-mechanical analyses have been previously performed to show the feasibility of the divertor plate design and its ability to accommodate a maximum heat flux of up to 10 MW/m^2, no experimental data have heretofore been published to support or validate such analyses. To that end, this investigation has been undertaken.

A test module with prototypical cross-sectional geometry has been designed, constructed, and instrumented. Experiments spanning the prototypical Reynolds numbers of the helium-cooled divertor have been conducted using pressurized air as the coolant. A second test module where the planar jet exiting the inlet manifold is replaced by a two-dimensional hexagonal array of circular jets over the entire top surface of the inlet manifold has also been tested. The thermal performance of both test modules with and without a porous metallic foam layer in the gap between the outer surface of the inlet manifold and the cooled surfaces of the pressure boundary were directly compared. For a given mass flow rate, the slot design with the metallic foam insert showed the highest heat transfer coefficient, with a pressure drop lower than that of the array of circular jets without foam. Additionally, numerical simulations matching the experimental operating conditions for the two cases without foam were performed using the computational fluid dynamics software package, FLUENT® v6.2. Comparisons of the experimental and numerical pressure drop, temperature, and heat transfer coefficient were made.

CHAPTER I

INTRODUCTION

1.1 Motivation and Objectives

1.1.1 Magnetic Confinement Fusion Energy

Fusion energy has a nearly infinite fuel supply and has the potential of satisfying much of the world's energy demands if its power can ever be harnessed (ITER, 2008). Therefore, fusion research is critical to the future of mankind.

In a fusion reaction, two light atomic nuclei fuse together to form a heavier one that is lighter than the sum of the two individual atoms. This difference in mass results in the release of a large amount of energy, through Einstein's mass-energy equivalence formula: $E=mc^2$. The fusion of 1 g of tritium and 2/3 g of deuterium produces 160 MW-hrs of thermal energy (Stacey, 1984). This reaction occurs because the combined nucleus is at a lower energy state than the individual nucleons. However, a natural barrier to fusion exists because of the positive charge of both nuclei, which creates a repulsive electrostatic force. In order to overcome this barrier, the atoms have to possess an extremely high amount of kinetic energy. This is achieved by applying external energy to heat the atoms to temperatures exceeding 10^7 K, at which point the atoms exist in a macroscopically neutral collection of ions and unbound electrons known as a plasma (Stacey, 1984). Additionally, this plasma must be confined at a relatively high density

such that fusion reactions occur at high enough rates to achieve a net positive energy balance. The two leading technologies for plasma confinement are magnetic confinement and laser inertial confinement. Laser inertial confinement utilizes the technique of implosion of a microcapsule irradiated by laser beams. Until recently, however, the laser implosion technique was hampered by the high power input required. As a result, magnetic confinement reactor concepts are more highly developed at this time. Magnetic confinement is based on the principle that charged particles spiral around magnetic field lines.

The tokamak concept shown in Figure 1 is the most extensively investigated design and the most advanced. The toroidal field is produced by a set of toroidal field magnets which encircle the plasma. The poloidal field and plasma heating is produced by an axial current induced by the transformer action of primary poloidal field coils (Stacey, 1984). This is the method used in ITER, the 500 MW experimental reactor currently under construction in Cadarache, France, which is scheduled to begin operation in 2018. Additionally, plans for a demonstration power plant, DEMO, and several advanced tokamak concepts are underway. This thesis considers the heat removal systems proposed for these advanced tokamak power plant concepts.

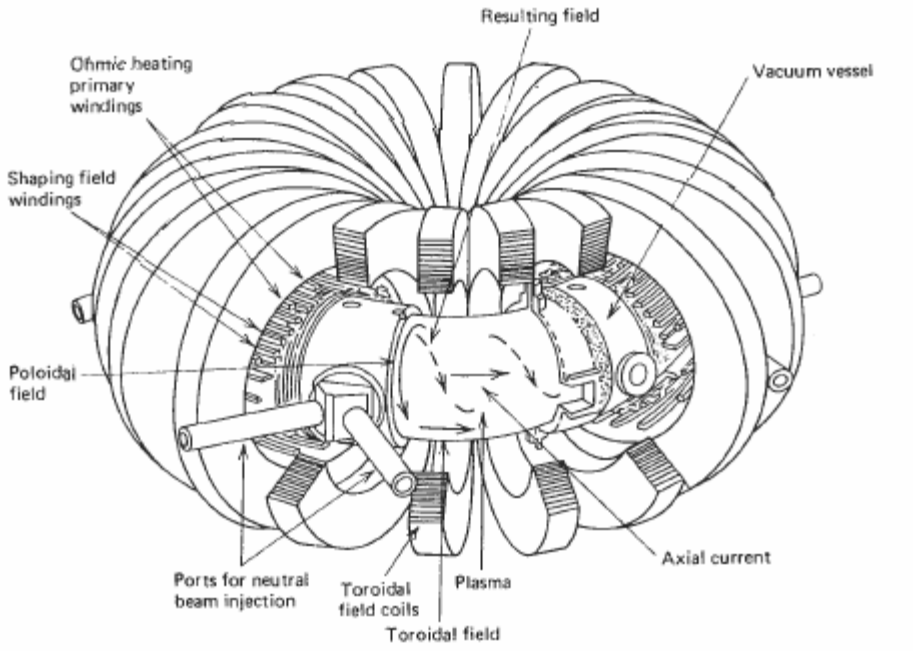

Figure 1.1: Tokamak Schematic (Stacey, 1984)

1.1.2 Proposed Divertors

When a fusion reaction occurs, the light nuclei (fuel) are converted to heavier nuclei. These heavy nuclei contaminate and cool the plasma, hindering further fusion reactions. Additionally, particles eroded from the reactor walls gradually enter the plasma during operation causing further cooling. To remove these contaminants, magnetic fields are used to "divert" particles escaping the main plasma onto a separate collection surface, named the divertor. Extremely high heat loads are expected on the divertor plates, on the order of 10 MW/m^2, since, in this region, the plasma is focused directly on the divertor target. As a result, a significant fraction (~15%) of the total fusion thermal power is removed by the divertor coolant. To cool the divertor plates and utilize this energy, a high efficiency coolant system is needed.

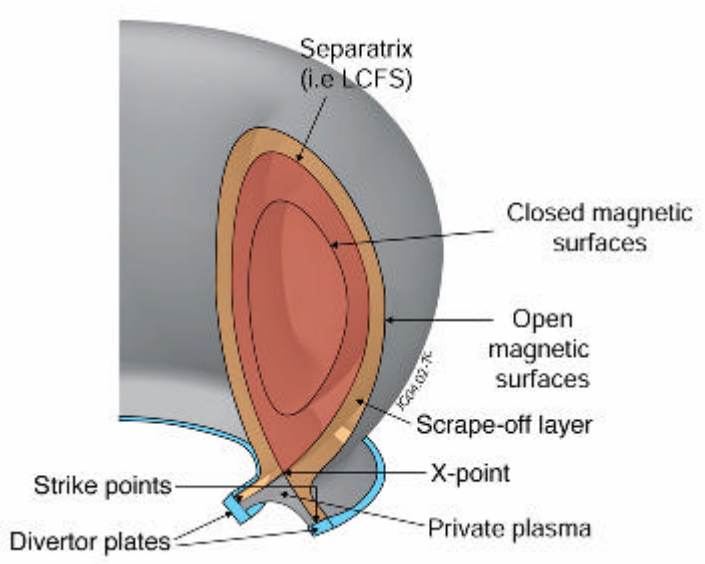

Figure 1.2: Geometry of Tokamak showing location of Divertor plates (EFDA-JET, 2008)

Divertors for fusion power plants must meet three main requirements: (1) they must be capable of handling exceptionally high heat fluxes; (2) they must deliver heat to the power conversion system at a temperature suitable for high efficiency; and (3) they must use a coolant compatible with the blanket system (Hermsmeyer and Malang, 2002).

In an experimental reactor, such as ITER, the requirements are less stringent. Since thermal efficiency and tritium extraction are not of concern, water can be used as the coolant and copper can be used as a heat sink. In a power plant, however, the use of cold water as divertor coolant would waste 10-20% of the total output power, with a comparable reduction of overall plant thermal efficiency. Additionally, water cooling is not well-suited for tritium production and extraction (Hermsmeyer and Malang, 2002). Many power plant studies have found helium (He) to be the most suitable coolant due to its chemical and neutronic inertness, compatibility with blanket materials, and ability to

achieve higher plant efficiencies. However, to withstand peak incident heat fluxes of 10 MW/m^2 using gas as a coolant requires significant heat transfer enhancement.

1.1.2.1 The Helium-cooled Flat Plate Divertor Concept

A conceptual design for a helium-cooled flat plate divertor (HCFP), capable of withstanding the required incident heat load of 10 MW/m^2, has been developed at the Karlsruhe Research Center (FZK) in Karlsruhe, Germany (Wang et al., 2008). The proposed design uses helium as a coolant with an inlet temperature of 600 ^oC and a pressure of 10 MPa. The HCFP uses planar jet impingement as the primary means of heat transfer enhancement. Its main advantage over other helium-cooled divertor target concepts derives from the fact that it offers the opportunity to construct the divertor using relatively large modules without exceeding the maximum temperature or stress limits for the structure.

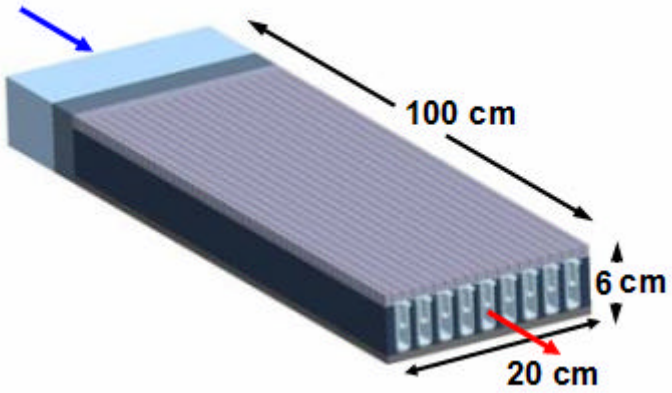

Figure 1.3: Schematic of ARIES HCFP divertor concept (Wang et al., 2008)

Each plate module covers an area of 2000 cm^2 based on toroidal and poloidal dimensions of 20 cm and 100 cm, respectively. Only about 750 plates are therefore needed for the 150 m^2 divertor of an ARIES-AT type power plant (Wang et al., 2008). Given that alternative divertor concepts such as the T-tube design (Ihli et al., 2007) and the helium-cooled multi-jet (HEMJ) finger design (Norajitra et al., 2006) cover areas of about 13 cm^2 and 2.5 cm^2 per module, respectively, the plate design reduces the total number of modules by more than two orders of magnitude for a given divertor area. The resultant reduction in the complexity of the manifold system required to supply coolant, along with the ease of manufacturing and installation of the divertor modules, is a major advantage for a power plant.

Nine inlet/outlet manifold units, separated by tungsten-alloy side plates are brazed together with a castellated tungsten (W) front plate to create the flat plate (Figure 1.3). The inlet and outlet manifolds are made of oxide dispersion-strengthened (ODS) steel (Wang et al., 2008). The inlet manifold is designed with a flattened top, as opposed to tubular designs such as the T-tube. Although, more difficult to manufacture, this design has the advantage of providing a nearly uniform thermal pathlength from the coolant to the heated surface. A 2 mm gap filled with stagnant helium is placed along the sides of each outlet manifold. This has the effect of raising the side wall temperature to eliminate thermal stresses caused by significant temperature gradients in the W structure (Wang et al., 2008).

The coolant, gaseous He, enters through the inlet manifolds near the top of the cartridge, and is then accelerated through the narrow (0.5 mm wide) rectangular slot along the entire length at the top of the inlet manifold (Figure 1.4). The planar He jet

impinges upon and cools the heated surface, then flows down along the sides of the inner cartridge to the outlet manifold on the bottom of the cartridge.

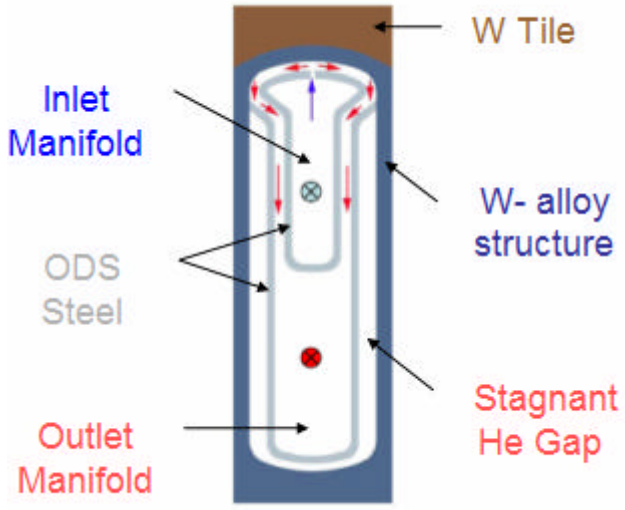

Figure 1.4: Schematic of single inlet/outlet manifold unit of the ARIES HCFP (Wang et al., 2008)

The HCFP concept being considered for the ARIES-Pathways study has undergone multiple iterations of thermo-fluid and thermo-mechanical analysis to improve cooling performance while reducing pumping power and thermal stresses (Wang et al., 2008). The most recent analyses predict that this design can achieve heat transfer coefficients as high as 39 kW/(m^2-K) at a pumping power of less than 10% of the thermal power. However, no experimental data have been published to date to support or validate these predictions. An experimental study of the flat-plate divertor was therefore performed in this investigation using air as the coolant.

1.1.2.2 The Short Flow-path Foam-in-Tube Divertor Concept

A new class of helium-cooled divertor concepts is under development, using an open-cell metallic foam inside of a tungsten tube. High heat flux tests conducted at Sandia National Laboratories of a tungsten tube filled with a tungsten open-cell foam measured maximum heat loads of ~22.4 MW/m^2. Sandia described this result as "a world-record heat flux for a helium-cooled refractory device." The heat flux performance of the tungsten foam/tungsten tube structure was approximately five times better than that of a tungsten tube with no foam (Ultramet, 2008).

As a result of this excellent heat transfer performance, an advanced and ultra low-pressure drop short flow-path (SOFIT) concept was designed by researchers at UCLA (Sharafat et al., 2007). The primary advantage of the SOFIT divertor concept is that the surface temperatures and the pressure drop through the porous medium are nearly independent of the length of the divertor. The concept is modular in design and can be customized to meet divertor size requirements. Foam has the added advantage, compared to a pin array, that it minimizes the need for joining to other functional materials, which eases manufacturability and improves performance reliability. At a heat load of 10 MW/m^2 the maximum surface temperature of a typical flat face SOFIT HX is estimated to be less than ~1100 °C (Sharafat et al., 2007).

The SOFIT concept consists of two concentric W-tubes with W foam sandwiched between them. The W-foam is selectively located to minimize the flow-path length through the porous media, maximize heat transfer, and minimize stress while maintaining an ultra-low pressure drop. The helium flow path of the SOFIT concept is illustrated in Figure 1.5. The pressurized coolant enters the inlet tube, which is capped at the opposite

end, so that the coolant is forced through a wide (2 - 4 mm) slot at the top of the inlet tube. It then flows through and cools the foam located in the annulus between the two tubes, before exiting the channel (Figure 1.5 right).

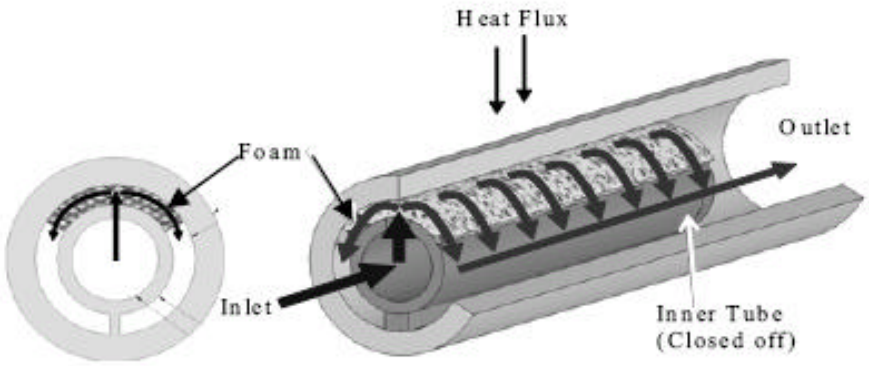

Figure 1.5: Schematic of a single channel of the SOFIT divertor (Sharafat et al., 2007)

It is of interest to experimentally test the theoretical predictions of the SOFIT concept as well as compare the thermal performance of the HCFP divertor module with and without foam between the cooled surface and the inlet manifold. The pressure drop comparison is also of key importance, since CFD codes often have difficulty modeling complex geometries and calculating pressure drop in the complex flow fields typically found in amorphous foams. As a result, experimental studies have been performed at Georgia Tech to obtain a direct comparison between the two concepts.

1.1.3 Objectives

This Master's thesis aims to experimentally validate and compare the high convective heat transfer coefficients associated with two of the leading jet impingement techniques for plate-type divertor designs; the effectiveness of the metallic foam concept will also be examined. The two jet impingement techniques examined are a planar jet issuing from a slot and a series of interacting circular jets issuing from a hexagonal array of round holes. The investigation will be performed by comparing experimentally measured temperature distributions of the cooled surface and overall pressure drop for both jet configurations in the presence and absence of a molybdenum foam layer between the outer surface of the inlet manifold and the cooled surface. Additionally, the effect of pore size on heat transfer performance will be evaluated by performing experiments with three different foam inserts: 45 pores per inch (ppi), 65 ppi, and 100 ppi. Finally, numerical results from the computational fluid dynamics software package, FLUENT®, will be compared to the experimental data obtained from the air flow loop tests for the array of holes test module (without foam insert).

The test section is designed to closely simulate the important features of the proposed HCFP divertor. The materials and heating system for the test module have been selected to match the actual material properties and directionality of the incident heat flux. Experimental data have been collected over a wide range of operating conditions that span the expected non-dimensional parameter range for prototypical operating conditions. A summary of the test module configurations examined is presented in Table 1.1.

Table 1.1: Summary of experimental test module configurations

NAME	DESCRIPTION
Holes	Array of circular jets – no foam
Holes-65	Array of circular jets – 65 ppi foam
Slot	Planar jet – no foam
Slot-45	Planar jet – 45 ppi foam
Slot-65	Planar jet – 65 ppi foam
Slot-100	Planar jet – 100 ppi foam

Several parameters are of interest for successful validation of the heat transfer coefficient for the HCFP divertor design. The variation of the convective heat transfer coefficient along the normal and axial directions of the cooled surface is important to prevent hot spots and thermal stresses. The behavior of the heat transfer coefficient under varying flow rates and incident heat fluxes provides important information for developing a robust design. Additionally, agreement between the predicted and measured pressure drop is desired.

This work is part of an ongoing experimental and numerical effort at Georgia Tech (GT) on evaluating the thermal-hydraulics of various plasma-facing components. Over the last four years, a wide range of experimental and numerical studies simulating various planar and circular jet impingement divertor cooling configurations have been performed at Reynolds numbers spanning prototypical values (Abdel-Khalik et al., 2008 and Crosatti, 2008)

1.2 Literature Review

This section is organized as follows. Section 1.2.1 introduces the early divertor design concepts. Advanced divertor designs are presented in Section 1.2.2. A detailed literature review can also be found in Weathers (2007).

1.2.1 Early Helium-cooled Divertor Designs

1.2.1.1 Porous Medium Concept

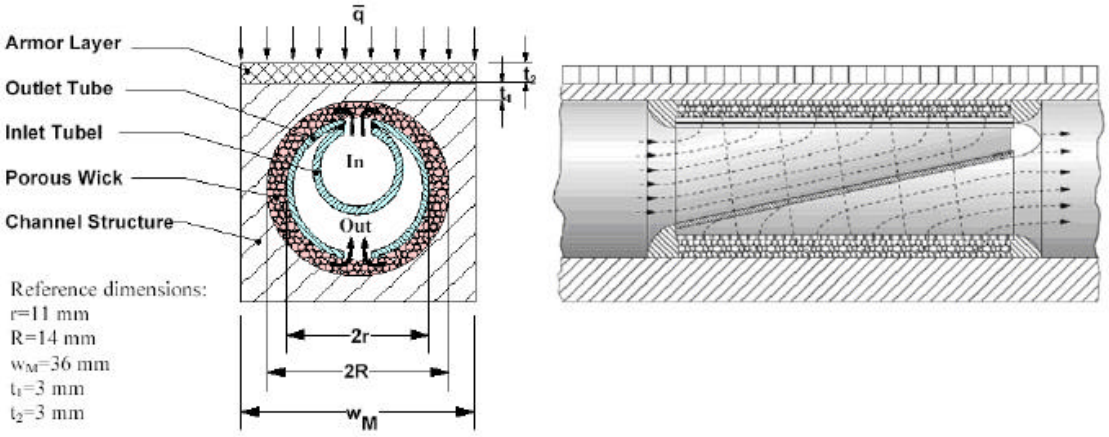

Figure 1.6: Cross-section (left) and longitudinal (right) views of the porous medium divertor (Hermsmeyer and Kleefeldt, 2001).

Porous media can increase heat transfer performance through two mechanisms: increase in cooling surface area (similar to the idea of heat exchanger fins) and increase in turbulent mixing due to the irregular coolant flow pattern. In this design, helium coolant enters the inlet tube and flows through a slot at the top of the inlet tube into a circular porous wick that has a void fraction of 40% (Hermsmeyer and Kleefeldt, 2001). The helium travels through the wick around the outer circumference of the coolant outlet tube and exits through a slot at the bottom of the outlet tube (Figure 1.7 left). The coolant

in the porous medium heats up in the circumferential direction due to the local energy deposition rather than accumulating heat along the entire channel length. This feature is desirable for non-uniform heating profiles (Hermsmeyer and Kleefeldt, 2001). To balance the flow velocities, the coolant inlet tube flow area is decreased while the coolant outlet tube flow area is increased along the length of the divertor channel (Figure 1.6 right). A molybdenum or tungsten alloy is the proposed material for constructing this divertor channel. Since this enhancement method relies in part on an increase in surface area, its effectiveness depends on the thermal conductivity of the porous medium material [Baxi and Wong, 2000]. This divertor is designed to operate at a pressure of 8 MPa, with a helium inlet and exit temperature of 632 ^{o}C and 800 ^{o}C, respectively. The predicted effective heat transfer coefficient is 20,000 W/(m^2-K) allowing the divertor to withstand an incident heat flux of 5.5 MW/m^2 (Hermsmeyer and Kleefeldt, 2001).

1.2.1.2 Multi-channel Concept

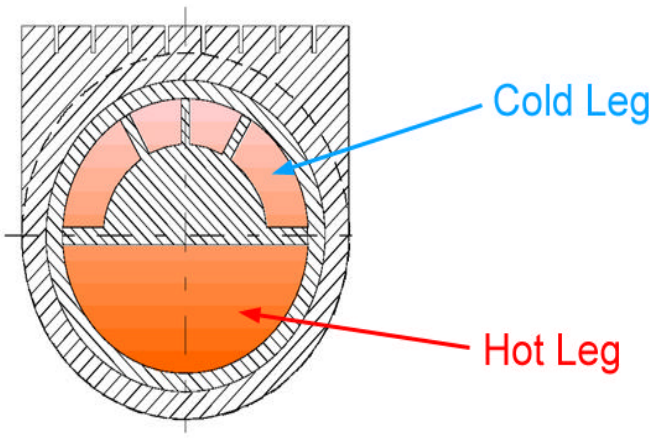

Figure 1.7: Cross-section of the multi-channel concept (Herm. and Kleefeldt, 2001).

The idea behind the multi-channel divertor concept was to minimize thermal stresses by reducing temperature differences across the divertor channel. A double-wall coolant pipe is divided into halves with an insert to create a cold leg that consists of four sub-channels and a hot leg consisting of a single channel (Figure 1.7). The heat transfer coefficient is enhanced by the larger coolant velocities through the sub-channels of the cold leg. The larger relative hydraulic diameter of the hot leg section helps minimize the pressure drop across the channel (Hermsmeyer and Kleefeldt, 2001). However, the exit temperature of 551 ^{o}C is colder than the desired input temperature range for the gas turbine power conversion system. This design can withstand an incident heat flux of 5 MW/m^2, when operated at 14 MPa with helium input at 500 ^{o}C. The typical effective heat transfer coefficient is 15,000 to 20,000 W/(m^2-K) (Hermsmeyer and Kleefeldt, 2001).

1.2.1.3 Eccentric Swirl Promoter Concept

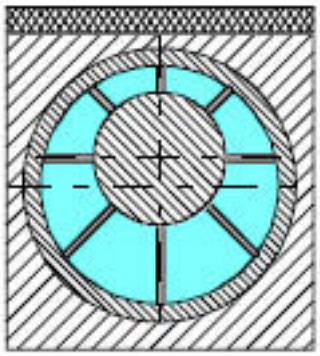

Figure 1.8: Cross-section of the eccentric swirl promoter concept (Hermsmeyer and Kleefeldt, 2001).

The eccentric swirl promoter concept enhances heat transfer by increasing the coolant velocity on the heated side of the coolant channel. A non-axisymmetric insert

with helical fins that vary periodically around the spiral direction of the coolant channel is used to create the enhancement (Figure 1.8). This design is capable of withstanding an incident heat flux of 5 MW/m^2 when operated with helium at 14 MPa. Helium enters the coolant channel at 600 ^oC and exits at 800 ^oC. An effective heat transfer coefficient of 21,000 W/(m^2-K) can be obtained with this design (Hermsmeyer and Kleefeldt, 2001).

1.2.1.4 Slot Concept

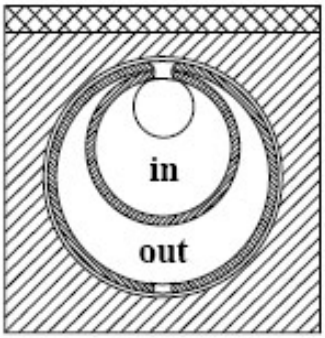

Figure 1.9: Cross-section of the slot concept (Hermsmeyer and Kleefeldt, 2001).

The slot concept developed out of the porous medium design. Instead of having the coolant flow through a porous medium, increased turbulent mixing is achieved simply by increasing velocity (jet impingement) by reducing the width of the slot to 0.1–0.2 mm (Figure 1.9). This approach simplifies the coolant channel, saving on manufacturing costs and time, and eliminates bonding issues of the porous medium (Hermsmeyer and Kleefeldt, 2001). The coolant channel diameters are tapered longitudinally in the same manner as for the PM design (Figure 1.6 right). The slot concept operates at 14 MPa, with helium inlet and exit temperatures of 600 ^oC and 800 ^oC, respectively, and is able to

withstand an incident heat flux of 5 MW/m^2. The typical effective heat transfer coefficient is 14,000 W/(m^2-K) (Hermsmeyer and Kleefeldt, 2001).

1.2.2 Advanced Helium-cooled Divertor Designs

1.2.2.1 Modified Slot Concept

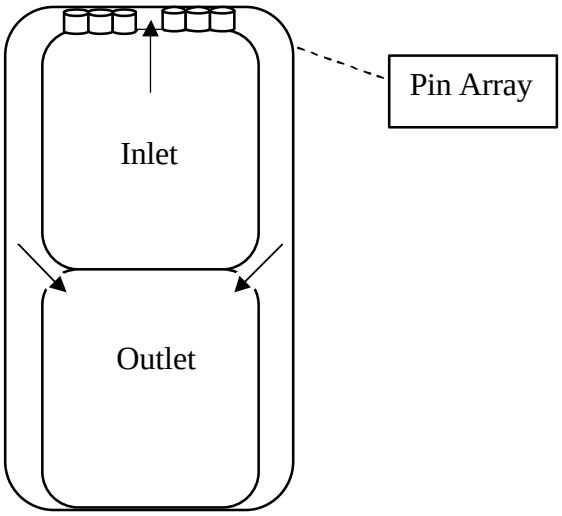

Figure 1.10: Cross-section of the modified slot concept

The "modified slot" design (Figure 1.10) was born out of the realization that all previously developed concepts were incapable of meeting the heat flux requirements predicted by power plant studies. After evaluating the various divertor concepts, Hermsmeyer and Malang regarded the PM concept as most promising, but found that there was a large scope for improving heat load capability.

The major improvements introduced by the modified slot are: (i) increased heat transfer to the target plate; (ii) reduced thermal pathlength from coolant to corners of target plate; (iii) insulating the coolant/structure interface around the outlet; and (iv)

reducing the PM to the region of large fluxes. Heat transfer to the target plate is enhanced by an array of tungsten pins sandwiched between the cooled surface and the inlet channel. The pin-fin array may be regarded as a special case of the PM concept. Pins were initially chosen over PM solely for analysis purposes, since no reliable correlations exist for He flowing through an amorphous tungsten structure. However, it is now believed optimized pin-fin arrays may outperform PM in heat transfer enhancement and pressure drop (Hermsmeyer and Malang, 2002). The inlet channel is rectangular in shape to eliminate the large variation in thermal pathlength present in the original PM and slot designs. The outlet structure is insulated with stagnant helium to prevent cooling of the lower structure which would create large temperature gradients and thermal stresses. Finally, pressure drop is reduced by limiting the pin fins to a relatively small flow section compared to the original PM design. The maximum local heat transfer coefficient expected from the modified slot design is 56,000 W/(m^2-K) when operated with 10 MPa He coolant at 640 ^oC inlet temperature, allowing a peak heat flux capability of 10 MW/m^2 (Hermsmeyer and Malang, 2002). The continued evolution of this design has led to the flat plate designs discussed in subsections 1.1.2 and 1.1.3.

1.2.2.2 High Efficiency Thermal Shield Concept

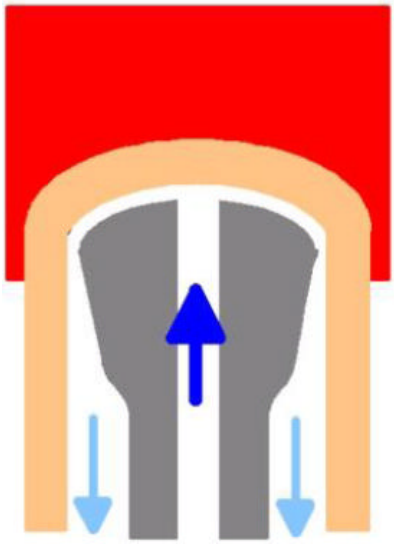

Figure 1.11: Cross-section of the HETS concept (Boccaccini et al., 2005).

The high efficiency thermal shield (HETS) concept utilizes a large number of small modules with a central impinging jet. The HETS is in the shape of an axi-symmetric cap. Helium coolant enters through the bottom of the module, at 10 MPa and 600 ^{o}C, and is accelerated through a 7 mm diameter nozzle before impinging on the curved heated surface (Norajitra et al., 2005a). The coolant then flows down the differential area between the inner nozzle structure and the cap (Figure 1.11). The HETS design was originally developed for a water coolant, but has been adopted for use with a helium coolant (Norajitra et al., 2005a). It is capable of sustaining an incident heat flux of 10 MW/m^2 and delivering helium at an exit temperature of 669 ^{o}C (Boccaccini et al., 2005). The maximum local heat transfer coefficient for the HETS concept is predicted to

be between 55,000 and 60,000 W/(m^2-K) (Norajitra et al., 2005a; Karditsas and Taylor, 2002) and the typical average value is 30,000 W/(m2·K) (Boccaccini et al., 2005).

1.2.2.3 T-Tube concept

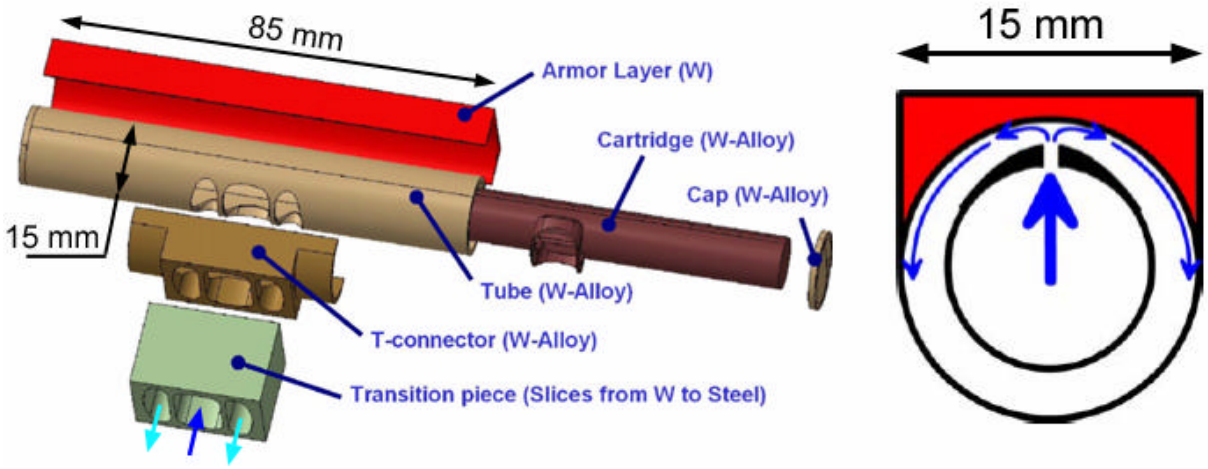

Figure 1.12: Diagram of the T-tube module (left) and cross-sectional view (right) (Ihli et al., 2005).

The T-tube slot jet divertor concept was selected for the ARIES-CS (Compact Stellarator) power plant study because of its ability to accommodate a heat flux up to 10 MW/m^2 using intermediate size modules (Abdel-Khalik et al., 2007). Helium coolant enters a concentric cartridge in each T-tube divertor module through an inlet port located mid-way along its length (Figure 1.12 left, dark blue arrow). The coolant admitted to the inner tube is accelerated through a narrow (0.5 mm wide) slit along its entire length toward the inner surface of the outer tube (Figure 1.12 right). The stagnation point flow generated by the impingement of the nearly two-dimensional rectangular jet on this heated surface cools the divertor with a moderate pressure drop. Downstream of the stagnation location, the helium forms a turbulent wall jet along the inside surface of the

outer tube and is then removed through the two exit ports near the center of the module (Figure 1.12 left, light blue arrows) (Crosatti, 2008).

Maximum local heat transfer coefficients in excess of 40,000 W/(m^2-K) are predicted near the stagnation point for operation with helium at 10 MPa and an inlet temperature of 600 ^{o}C. The high heat transfer coefficient predicted for this design has been experimentally validated with an air coolant corresponding to the non-dimensional parameters anticipated for its helium operating conditions (Crosatti, 2008).

1.2.2.4 Helium-cooled Modular Divertor Concept with Pin Array

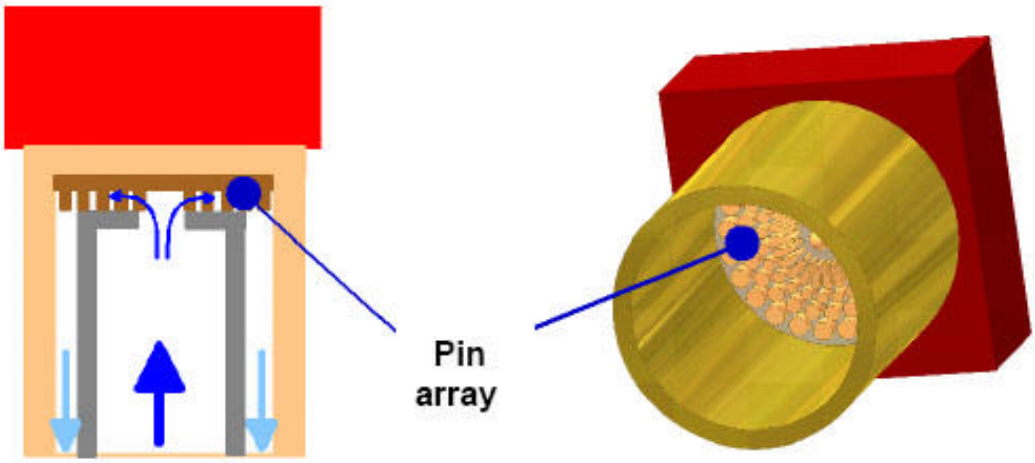

Figure 1.13: Diagram of the HEMP concept (Norajitra et al., 2005b).

The helium-cooled modular divertor concept with pin array (HEMP) is a hybrid of the HETS and modified slot divertor concepts. The geometry is nearly identical to that of the HETS concept, with the addition of a scattered array of W pins sandwiched between the inlet channel and cooled surface (Figure 1.13). Like the PM and modified slot concepts, heat transfer enhancement is achieved through both an increase in turbulent

mixing and in cooling surface area. Based on the findings of Hermsmeyer and Malang, who analyzed the use of a pin-fin array in the modified slot concept, a maximum local heat transfer coefficient of 56,000 W/(m^2-K) can be achieved with this method of heat transfer. It is capable of withstanding an incident heat flux up to 10 MW/m^2 using helium at 600 ^oC inlet temperature and 10 MPa. The exit temperature is predicted to be as high as 700 ^oC (Kruessmann et al., 2004). A challenge for the HEMP, as well as the PM and modified slot concepts, is the effect of manufacturing tolerances on the pin array.

1.2.2.5 Helium-cooled Modular Divertor Concept with Slot Array

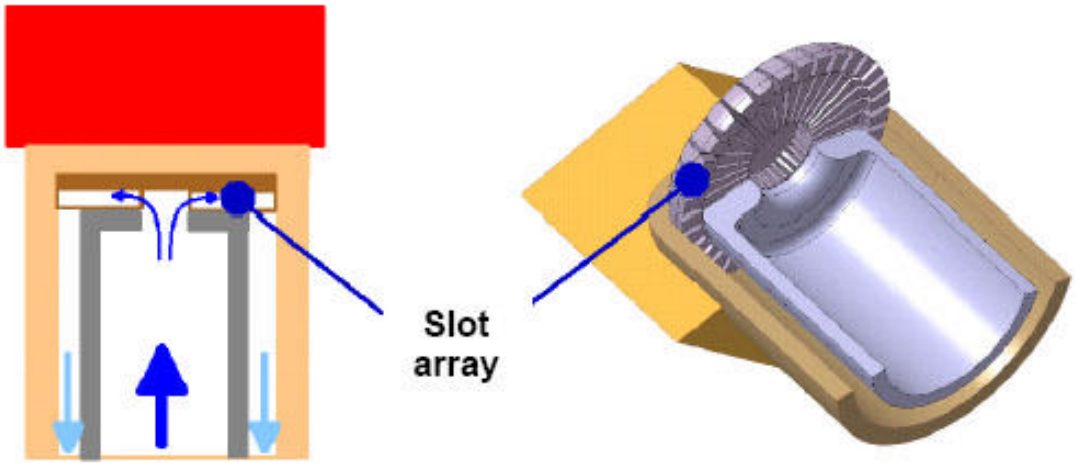

Figure 1.14: Diagram of the HEMS concept (Norajitra et al., 2005b).

Another variation of the cap-shaped, helium-cooled modular divertor is the HEMS, or helium-cooled modular divertor with slot array. This design was proposed as an improvement upon the HEMP concept. The HEMS concept increases the surface area with a W radial slot formation, as shown in Figure 1.14, rather than a pin array. This

design is considerably easier to manufacture with reasonable tolerances compared to the pins. One disadvantage of this design, however, is the lower turbulent mixing expected in an organized array of fins.

The coolant flow path is shown in Figure 1.14. Helium enters through the bottom of the module and into the slot array from the center of the module. After flowing radially outward through the tungsten slots, the coolant exits the module by flowing down along the outside of the inlet channel. The HEMS concept is capable of withstanding an incident heat flux of 10 MW/m^2 under operating conditions of 10 MPa and a helium inlet temperature of 634 ^oC. The maximum local heat transfer coefficient predicted for this design is 43,000 W/(m^2-K) and the average effective value is 24,000 W/(m^2-K). Helium would exit at an outlet temperature of 713 ^oC (Kruessmann et al., 2004).

1.2.2.6 Helium-cooled Modular Divertor Concept with Jet Array

Finally, the leading helium-cooled modular divertor design for the EU community is the helium-cooled Multi-Jet divertor (HEMJ). Extensive numerical and experimental analyses have been performed at FZK and Georgia Tech to characterize the divertor geometry, select appropriate materials, simulate heat removal capability, and validate the extremely high predicted HTC.

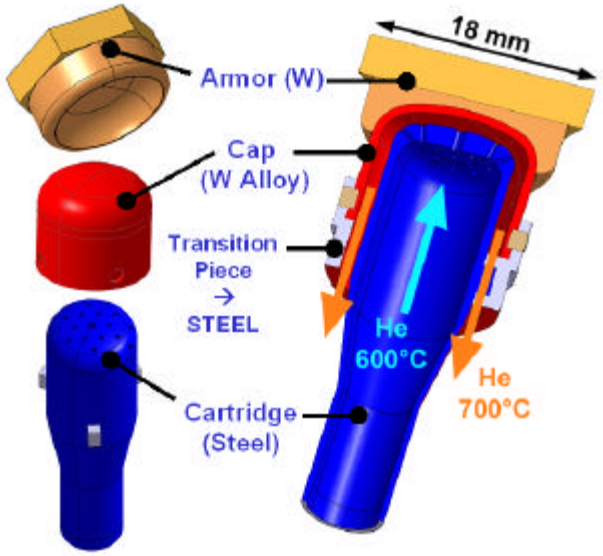

Figure 1.1**5:** Diagram of the HEMJ concept (Ihli, 2005).

The plasma-facing target is a tungsten armor plate which is attached to a tungsten-alloy (WL10) cap. A cylindrical steel cartridge that has twenty-four 0.6 mm diameter holes which surround a single 1.0 mm diameter hole in the center is secured below the cap (Figure 1.15). The jets are spaced by ~2 mm on a staggered grid. Helium enters the cartridge and is accelerated through the twenty-five holes to create a jet impingement on the capped inner surface of the tungsten alloy. Downstream of the jet impingement location, the helium forms a turbulent wall jet along the surface of the cap (Figure 1.15). The helium then exits the divertor at approximately 700 ^{o}C by flowing through a 0.9 mm gap between the cartridge and the cap. Maximum local heat transfer coefficients in excess of 50, 000 W/(m^2-K) are predicted near the stagnation point for operation with helium at 10 MPa and an inlet temperature of 600 ^{o}C. The high heat transfer coefficient predicted for this design has been experimentally validated with an air coolant corresponding to the

non-dimensional parameters anticipated for its helium operating conditions (Crosatti, 2008)

CHAPTER II

EXPERIMENTAL APPARATUS AND PROCEDURES

This chapter describes the experimental test section used to simulate the helium cooled flat plate (HCFP) divertor to verify the numerical results mentioned in subsection 1.1.2.1, along with the Georgia Tech experimental test loop and the procedures used to conduct the experiments. Section 2.1 details the experimental test section and test loop, while Section 2.2 presents the experimental procedures and test parameters.

2.1 Experimental Test Section

This section describes the experimental test section and test loop. Specifically, subsections 2.1.1, 2.1.2, 2.1.3, 2.1.4 and 2.1.5 detail the inner cartridges, the outer shell, the copper heater block, the assembly of the HCFP divertor test section, and the flow loop, respectively.

2.1.1 Inner Cartridge

The inner cartridge of the test section represents the inlet and outlet manifolds of the HCFP divertor module. Two aluminum inner cartridges, one for each jet impingement geometry, modeling the ODS steel inlet/outlet manifolds of the HCFP design, were constructed for this study. Aluminum was selected as the material for the inner cartridge based on its low cost, ease of machining, and widespread availability.

The two inner cartridges have identical dimensions (within machining tolerances) excluding the jet geometry on the top surface. The overall dimensions of the inner cartridge are 40.92 mm (height) x 19 mm (width) x 88.15 mm (length). A base flange exists at the bottom of the inner cartridge for the purpose of attaching it to the outer shell (6.48 mm (height) x 37.00 mm (width) x 104.2 mm (length), making the total height of the inner cartridge component 47.40 mm (Figure 2.1). A ½" (12.7 mm) diameter hole, with a UNF (Unified National Fine) thread profile of 20, is machined on the inlet and outlet side for the connection of the brass,1/2" (12.7 mm) OD, 3/8" (9.525 mm) ID, inlet and outlet tubes (Figure 2.1).

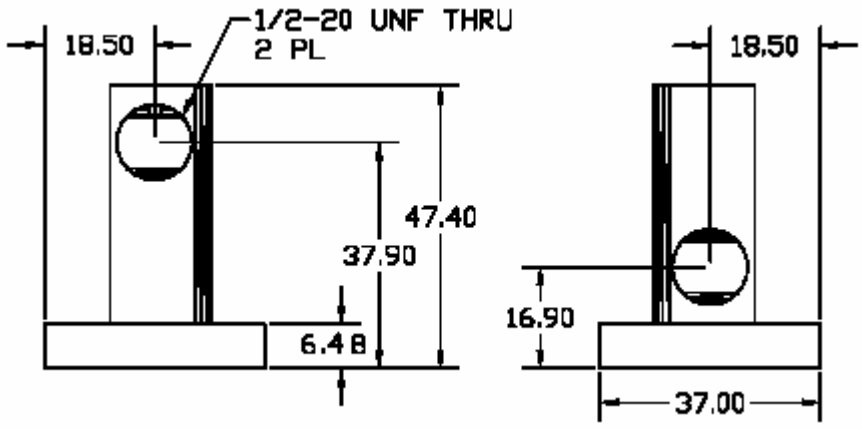

Figure 2.1: Inlet-side view (left) and outlet-side view (right) of the inner cartridge (AutoCAD 2006)

The shaded region along the right side of the inner cartridge (Figure 2.1, left) indicates a curved corner; it does not appear on the opposite side because it was necessary to remove one of the sides to machine the rectangular inlet and outlet manifolds (Figure 2.2 left). After machining the manifolds within the cartridge, the side surface of the cartridge was covered by a plate secured in place by 3 screws attached to

the aluminum rib separating the two manifolds (Figure 2.2). The inlet and outlet manifolds both have dimensions of 76.2 mm (length) x 19 mm (width) x 15 mm (height). A 2 mm wide slot, extending the entire length of the inlet manifold (76.2 mm) is machined into the top of one of the inner cartridges (Figure 2.2). Seven holes, 4.90 mm in diameter, along each side of the test section provide passage for the hot coolant to enter the exit manifold and exit the system (Figure 2.2, right).

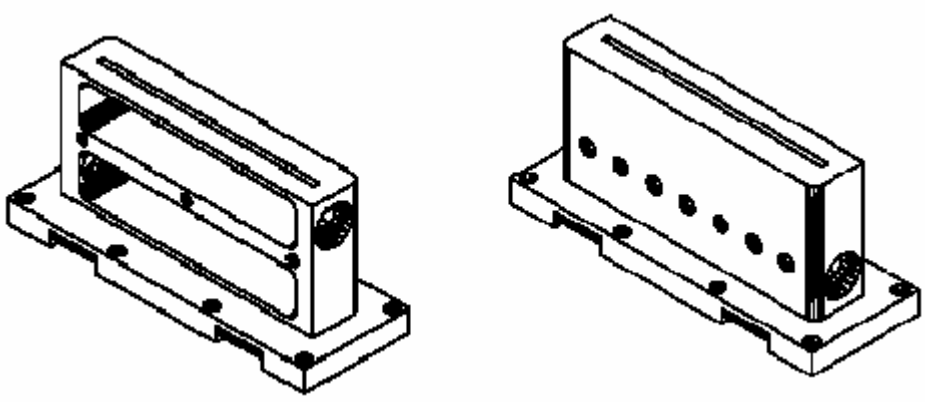

Figure 2.2: Missing plate view (left) and intact outer surface view (right) of the slotted inner cartridge from AutoCAD 2006.

The inner cartridge machined with the array of holes is shown in Figure 2.3. There is a total of 33 holes on a staggered 3-2-3 array with a row spacing of 5.86 mm and column spacing of 5 mm. The diameter of the holes is 1/32", or ~ 0.8 mm. The diagonal distance between holes is 6.37 mm; taking this value as the "pitch" gives a pitch-to-diameter ratio of 8.0. This value corresponds to the "optimum pitch to diameter ratio" for multiple-jet impact cooling as reported by San and Lai (2001) since it yields the maximum stagnation Nusselt number, Nu_{sg}, for all Reynolds numbers.

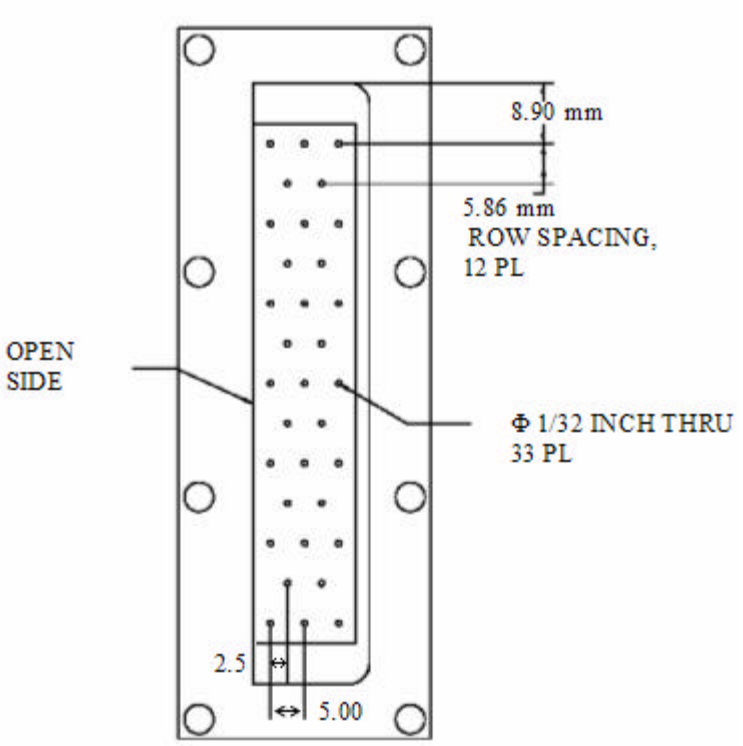

Figure 2.3: Top view of inner cartridge with jet array from AutoCAD 2006.

Figure 2.4: Photograph of the manufactured inner cartridges. The outlet port is visible near the bottom of the side of both cartridges.

The height of the gap, or the distance between the outer surface of the inner cartridge and inner surface of the outer shell (i.e. the cooled surface), is 1 mm for the cases without foam and ~2 mm when foam is present. When jet impingement is the primary cooling method, a small wall gap-to-diameter ratio is desired to prevent mixing with the recirculation flow which has been shown to reduce the stagnation Nusselt number (San and Shiao, 2006). In the cases with the foam insert, however, jet impingement is ineffective since the jets must flow through the foam to get to the cooled surface. Therefore, an increased gap, in the case of the foam, increases the cooling surface area and enhances turbulent mixing. A tradeoff exists, of course, since an increase in porous medium (PM) results in an increased pressure drop, and in the limiting case, no flow reaching the cooled surface. The thickness of 2 mm, provided by Sharafat (2007b), may therefore not be the optimal thickness for this design.

The original design proposed by Sharafat (2007b) featured a 2 mm slot in the foam, coinciding with the 2 mm slot machined in the inner cartridge. For this reason a 2 mm slot was machined into the inlet manifold for these studies (vs. the 0.5 mm slot proposed for the original HCFP design). The slotted foam design would likely provide the highest heat transfer coefficient, since it would allow coupling of all of the enhancement methods, i.e. jet impingement, increased turbulent mixing, and increased surface area. Additionally, the pressure drop would be reduced, compared to the case of foam with no slot, since PM is removed from the region of highest velocities and selectively located on the sides, where HTC due to jet impingement drops significantly. However, placement of a slot within the foam was abandoned for the present study due to concerns expressed by Ultramet (Sharafat, 2008) about the fragility of the foam. Still, this configuration may warrant revisiting in the future due to the favorable attributes listed above. Additionally, plans exist for creating an inner cartridge with a 0.5 mm slot to more closely duplicate the jet impingement geometry of the original HCFP design. Cross-sectional views of the test module configurations evaluated in this work are shown in Figure 2.5. The brass outer shell and aluminum inner cartridges are shown in red and green, respectively.

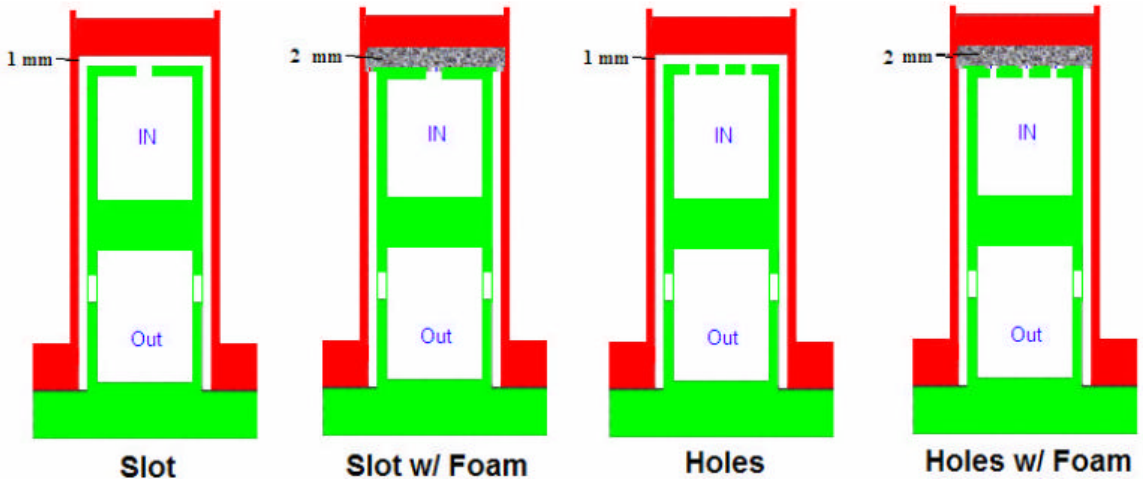

Figure 2.5: Cross-sectional views of the test module configurations studied.

2.1.1.1 Molybdenum foam insert

The foam used in this study was manufactured by Ultramet. The foam is created by pyrolyzing a polymer foam to create a reticulated vitreous carbon foam. Refractory metals are then infiltrated into the foam to tailor the material properties for specific applications (Ultramet, 2008). The manufacturer listed advantages of the metallic refractory open-cell foams are: (1) high specific thickness; (2) high surface area; (3) low pressure drop; (4) tailorable pore size and foam density; (5) ability to apply metal face sheets to create actively cooled structures; and (6) fabrication from various metals (Ultramet, 2008). Tungsten and molybdenum are among the refractory metals that can be used to create the foam. Tungsten is the most likely candidate for MFE applications.

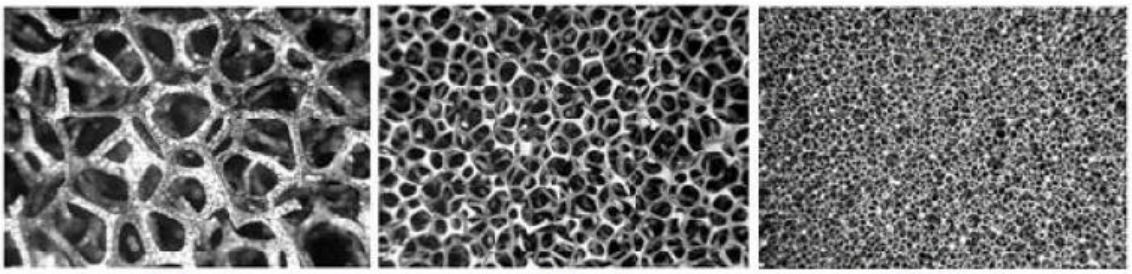

Figure 2.6: Three samples of RVC foam showing pore structure at different pore sizes (all ~10x magnification, Ultramet, 2008).

The foam used in this study is made of molybdenum. The pore sizes examined were 45 ppi (0.45 mm D), 65 ppi (0.27 mm D), and 100 ppi (0.17 mm D) (Williams, 2008). As shown in Figure 2.6, an increase in ppi corresponds to an increase in the number of pores per unit volume and smaller pore sizes. Note that an increase in pore size does not necessarily equate to an increase in porosity, where porosity is defined as the volume of pores divided by the total volume of the section. (For a given container size, it is possible to have one giant ball with the same total volume, and therefore porosity, as 100 smaller balls.) However, an increase in the number of pores (for a given porosity) will result in an increase in surface area, increase in turbulent mixing, and an increase in pressure drop. Therefore, an optimum pore size exists that will maximize the HTC while requiring a moderate pressure drop. Performing experiments, holding all variable constant except pore size, will provide a starting point for this optimization. Although it is unlikely that any of the three cases studied will correspond to this optimal point, the data obtained will be useful in developing correlations and validating models that can be used to find this balance.

The overall dimensions of the foam sections varied slightly for each piece. Most of the pieces were slightly too long or too wide to fit inside the brass outer shell and were

gently filed to the necessary dimensions using sandpaper. The dimensions of the foams inserted into the test section were 88 mm (length) x 21 mm (width) x 2.0 (or 2.1) mm (thickness). The 100 ppi and 45 ppi foam pieces as manufactured by Ultramet had a thickness of 2.0 mm, while the 65 ppi piece had a thickness of 2.1 mm. No efforts were made to remove any of the thickness of the foam piece based on engineering judgment that this would likely damage the piece. Once in location, sandwiched between the outer surface of the inner cartridge and the inner surface of the outer shell (Figure 2.4), the foam was compressed 0.1 mm to ensure good thermal contact. Therefore, the final gap thickness in the 45 ppi and 100 ppi cases was 1.9 mm, while the final gap thickness in the 65 ppi case was 2.0 mm. The porosities of the 45 ppi, 65 ppi, and 100 ppi foams were 70%, 88%, and 86%, respectively.

2.1.2 Outer Shell

The outer shell of the test section is made of C3600 free machining brass, which closely duplicates the W-alloy structure and the tungsten pressure-boundary flat plate. Brass was chosen for this piece, since the thermal conductivity of C3600 brass (115 W/(m-K) at 20^{o}C, www.MatWeb.com) is similar to that of the W-alloy at prototypical conditions (95-107 W/(m-K) from 500-1300 ^{o}C, ITER Material Properties Handbook, 2001). The outer shell has a total height of 47.4 mm, including a 1 mm raised edge along the periphery used to center the copper heater block on the top surface of the brass shell. The brass shell is 5 mm thick on top and 2 mm thick on the sides. The flange on the lower periphery of the outer shell is used to connect it to the inner cartridge. The connection is made with eight 6-32 UNC screws (four on each side) as shown in Figure

2.7. A silicone rubber gasket is placed between the mating flanges of the outer shell and inner cartridge (see Fig. 2.8)

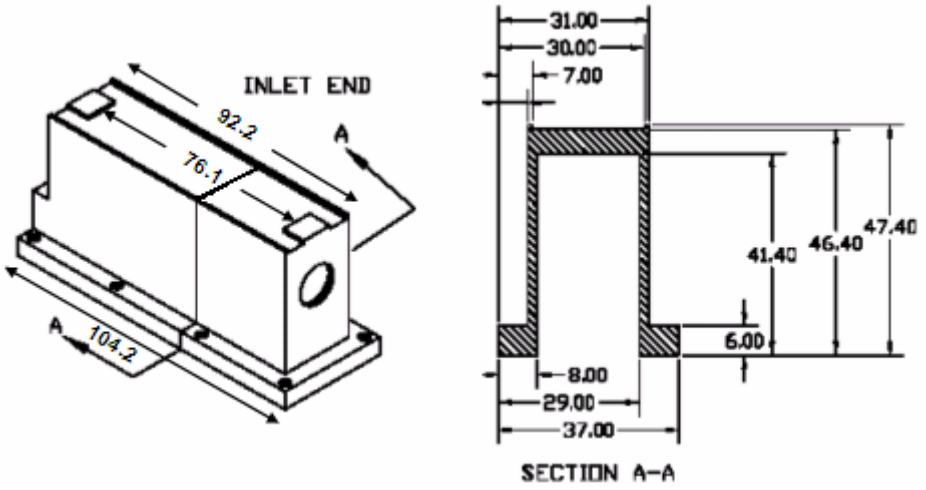

Figure 2.7: Schematic (left) and cross-sectional view (right) of outer shell (AutoCad 2006).

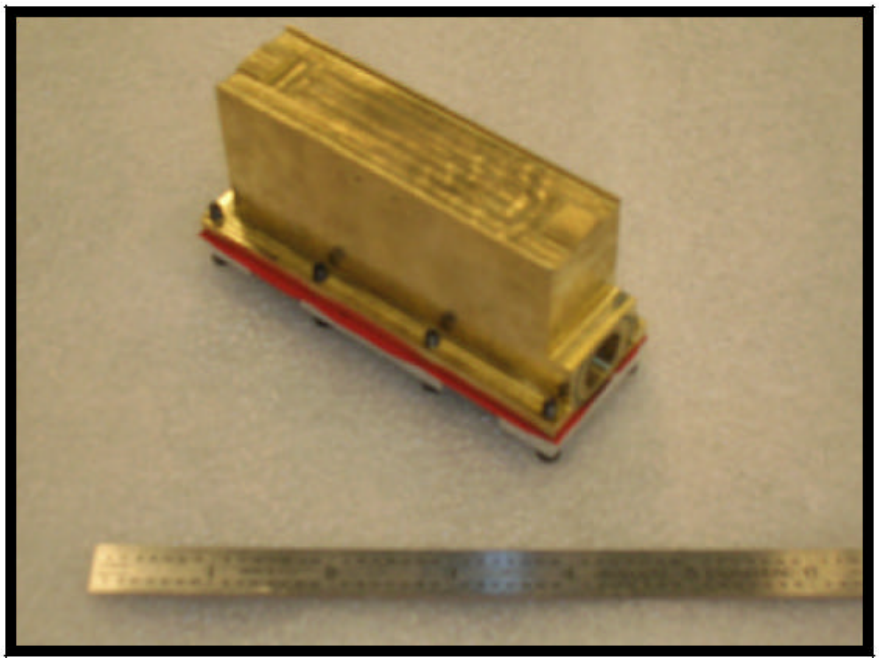

Figure 2.8: Photograph of brass outer shell connected to the inner cartridge (Outlet View). (The red in the photograph is the silicone rubber pressure gasket.)

The outer shell is instrumented with five E-type thermocouples (TCs) (OMEGA EMQSS-020G-6) to measure the temperature profile of the cooled surface. The center of the TC beads are all at the same elevation (*z* location), namely 1 mm above the cooled surface of the brass shell. The locations of the TCs were chosen such that the symmetry of the cooled surface temperature distribution could be evaluated while measuring the temperature variations on the surface (i.e., distance from inlet or distance from jet). The origin corresponds to the center of the cooled surface in the normal (x-direction) and axial (y-direction), as well as the location of TC "2" (Figure 2.9). TCs "3" and "4" are each located 8.5 mm from the centerline of the slot, however "3" is 10 mm downstream of the origin, while "4" is 5 mm upstream of the origin. Similarly, TCs "1" and "5" are each located 4.5 mm from the centerline, with TC "1" 10 mm upstream of the origin and TC "5" 5 mm downstream of the origin. Table 2.1 lists the location of these thermocouples. A schematic of the TC locations in the brass shell (Figure 2.9) and a bird's eye-view of the TCs position with respect to the jet geometry (Figure 2.10) is also presented.

Table 2.1: Cooled surface thermocouple positions and reference numbers

Thermocouple Reference #	***x*** [mm]	***y*** [mm]
1	-4.5	-10
2	0	0
3	-8.5	10
4	8.5	-5
5	4.5	5

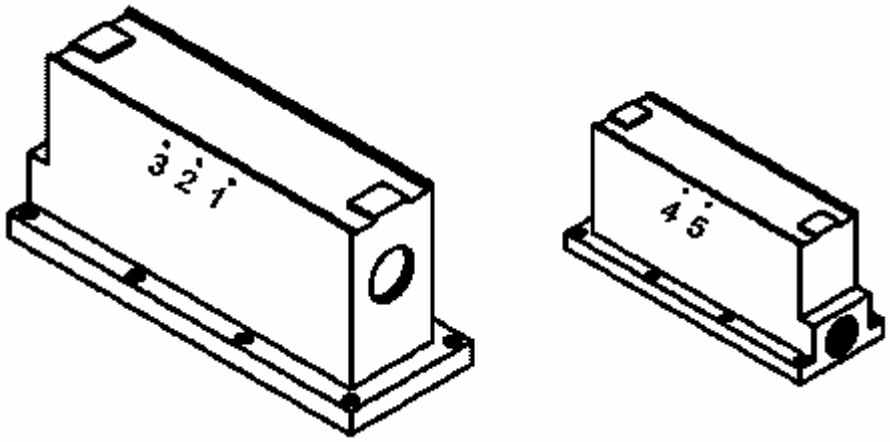

Figure 2.9: Sketch of brass outer shell showing the location of the 5 TCs: inlet view (left) and outlet view (right).

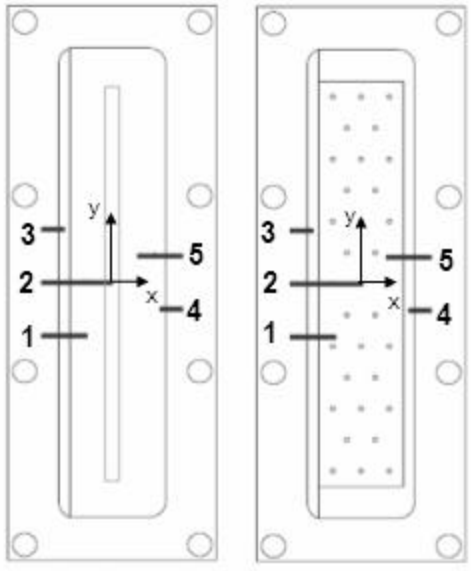

Figure 2.10: Sketch showing the position of the 5 TCs with respect to the slot (left) and the array of holes (right).

After inserting each thermocouple into the appropriate hole, it was bent to the side to prevent movement. The thermocouple probes were then further secured by the insulation which surrounded the test section and was tightly wrapped with a high-strength nickel wire.

2.1.3 Copper Heater Block

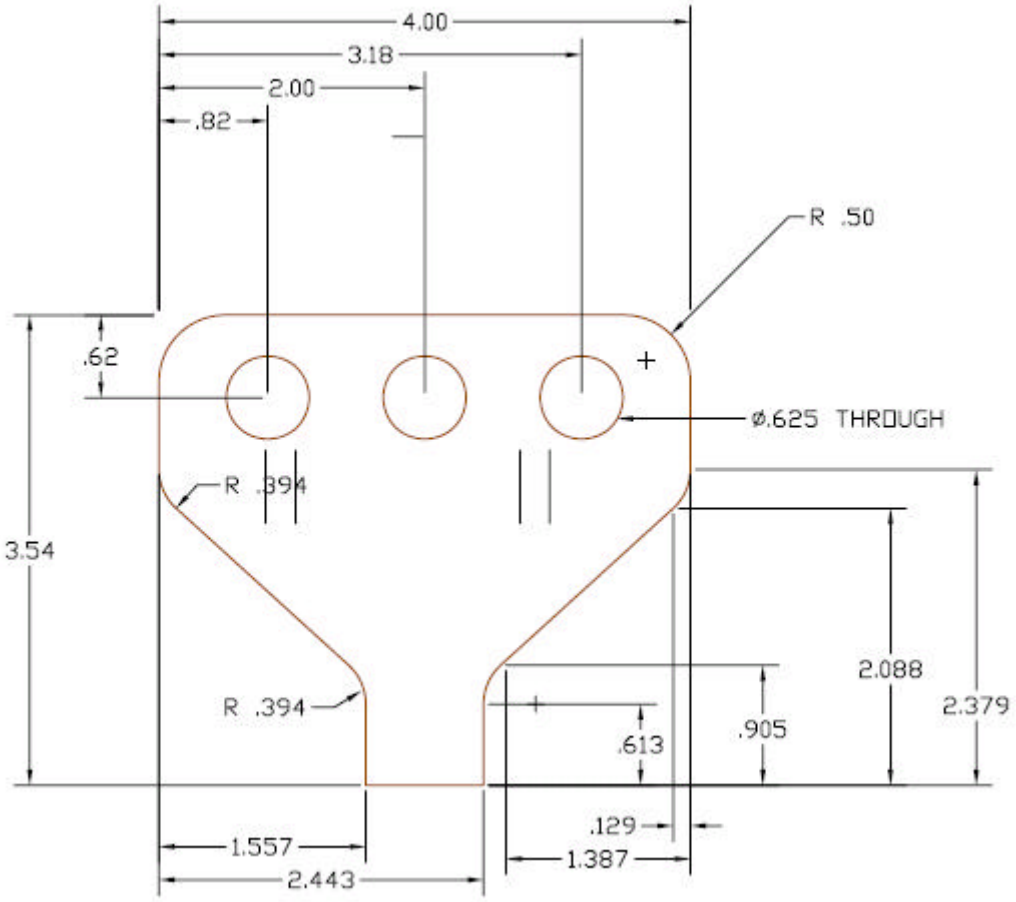

Figure 2.11: Drawing of the copper heater block from AutoCAD 2006.

A C14500 copper-alloy heater block, or concentrator, containing three 750 W cartridge heaters (FAST- HEAT® CH47474 120 V 750 W) is used to produce a uniform axial heat flux on the top of the brass outer shell, thereby simulating the incident heat flux on the divertor plate surface (Figure 2.11). The block is 4" (101.6 mm) wide at the top and is tapered down to a width of 0.865" (22 mm) at the neck to focus and increase the heat flux incident upon the test section. The heaters, which provide the power input (*i.e.*,

the heat flux incident on the outer brass shell), are connected in parallel. The input voltage is adjusted by a variable autotransformer (General Electric Volt-Pac). The input power and current are measured by a digital multimeter (Hewlett Packard 34401 A) and an AC ammeter (Shurile Model 8508), respectively. Each heater has a maximum output of 750 W, yielding a maximum possible heat flux of 1.35 MW/m^2.

Six E-type TCs (OMEGA® EMQSS-020G-6) are embedded in the "neck" of the concentrator to measure the incident heat flux. The TCs are located on two *x*-*z* planes corresponding to 1/3 and 2/3 of the copper block length (*y*) and extend to the midpoint of the copper neck width (*x*). The (z) positions correspond to 3.0, 7.0 and 12.0 mm above the contact surface with the brass outer shell (Figure 2.10). Additionally, two 1.59 mm diameter OMEGA Type-E thermocouples are embedded in the top of the copper heater block to a depth of 0.62 mm (corresponding to the centerline of the heater cartridges) and are located halfway between the middle heater and the side heaters. This provides a monitor of the peak temperature of the copper heater block, which is limited to 500°C (half of the melting temperature for this copper alloy). Table 2.2 provides the thermocouple labeling convention and positions for the copper heater block. A schematic of the copper block and TC locations is shown in Figure 2.12.

Table 2.2: Copper heater block thermocouple positions and reference numbers

Thermocouple Reference #	*y* [mm]	*z* [mm]
6	25.4	3
7	25.4	7
8	25.4	12
9	50.8	3
10	50.8	7
11	50.8	12

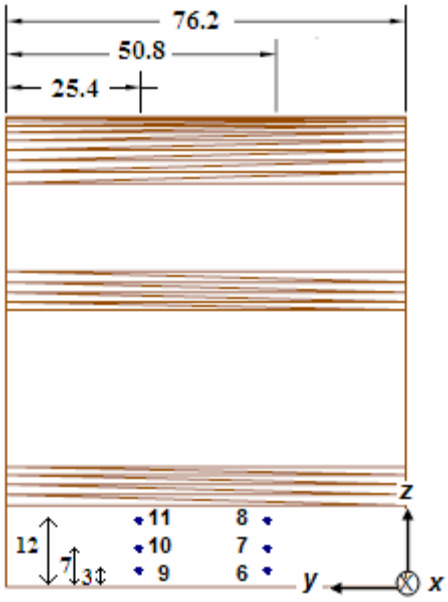

Figure 2.12: Side-view of copper heater block showing the locations of the 6 TCs that measure heat flux in the "neck" region.

2.1.4 Assembled HCFP Test Section

To simulate the thermal-hydraulic behavior of the HCFP divertor, a test section consisting of an aluminum inner cartridge, a brass shell, and a copper heater block was constructed. The concentrator is clamped to the top side of the brass outer shell by two

plates on the top and bottom of the test section and four long bolts (Figure 2.13, left). An exploded view of the test section is shown in Figure 2.13 (right). A thin, 0.13 mm, graphite sheet is placed between the concentrator heater and the brass shell to ensure good thermal contact between these two components. The completed test module is then insulated with 5 cm thick panels of mineral wool and wrapped with wire to secure the insulation. The insulated HCFP divertor test section is shown in Figure 2.14.

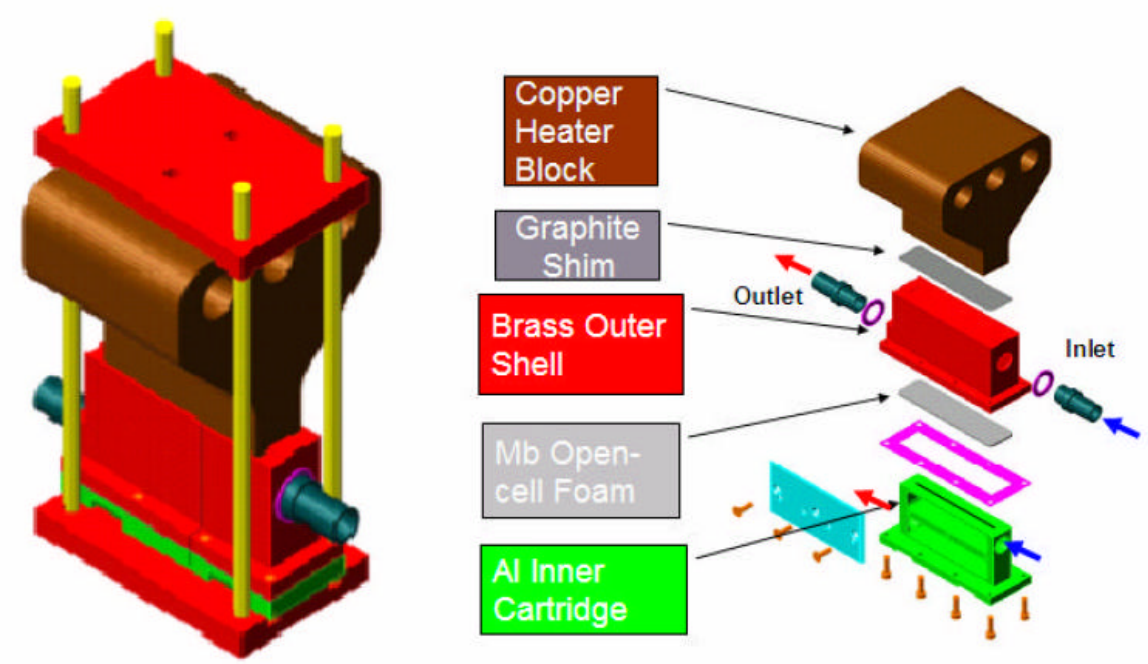

Figure 2.13: Schematic of the assembled HCFP test section (left) and exploded view (right).

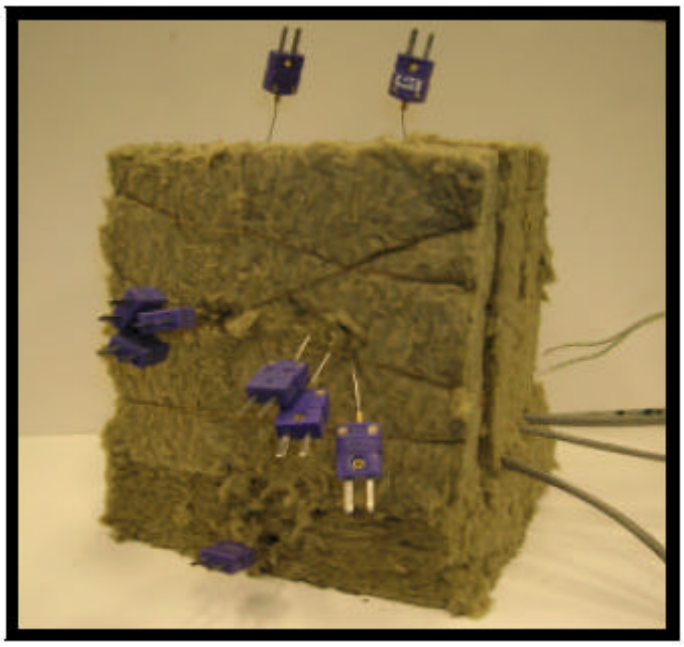

Figure 2.14: Photograph of the insulated HCFP divertor test section. (The test section is placed upside down since the copper heater block is extremely top heavy.)

2.1.5 Experimental Flow Loop

Experimental studies were performed by placing the test section in an open flow loop using air as the coolant. Air from a compressed-air line at gauge pressures of 116 – 524 kPa flows through a large rotameter (Brooks R12M-25-4), and is discharged to a fume hood after flowing through the test module. The mass flow rate is calculated from measurements of the volume flow rate (by the rotameter) and the air density determined from the inlet temperature and pressure. A pressure gauge (Marsh 100 psi) at the exit of the rotameter measures the test section inlet pressure; it has a resolution of 1 psig or 6.8 kPa. A 5.5 foot (1.7 m) long piece of ½" (12.7 mm) ID reinforced Tygon tubing (Kuriyama K3150 200 psi/1.4 MPa) connects the rotameter to a 1" NPT brass cross which is connected to the brass inlet tube on the opposite side via a 0.5" (12.7 mm) ID Swagelok. The remaining two ports on the inlet cross are used to connect a TC and one

side of a differential pressure transducer. The inlet temperature T_{in} is measured using an OMEGA Type-E thermocouple (OMEGA® EMQSS-125G-6). A 30 psi (207 kPa) differential pressure transducer (OMEGA® PX180-060DV) is used to monitor the pressure drop across the test section.

Similarly, a 1" NPT brass cross is connected to the brass outlet tube via a 0.5" (12.7 mm) ID Swagelok. This cross houses an OMEGA Type-E thermocouple (OMEGA® EMQSS-125G-6) to measure the outlet temperature T_{out}, a butterfly valve to control the mass flow rate, $\dot{m}$, and a small SS cross. The smaller cross is used to connect the outlet side of the differential pressure transducer as well as a pressure gauge (OMEGA® 100 psi – with a resolution of 0.5 psi) to measure the outlet pressure P_{out}; one side of the cross is unnecessary and is plugged. A 5/8" (15.9 mm) ID butterfly valve (Milwaukee Valve Co. BB2) is placed after the 1" (25.4 mm) cross to control the mass flow rate through the test section. Controlling the mass flow rate at the outlet allows a higher system pressure to be maintained in the test section, which prevents choking. However, in some cases, the flow control valve was placed at the inlet, and the outlet pressure was atmospheric, to test the effects of system pressure on HTC. Finally, the ambient pressure is measured using an absolute pressure transducer (OMEGA PX302-015AV). A schematic and photograph of the flow loop are provided in Figure 2.15 and 2.16, respectively.

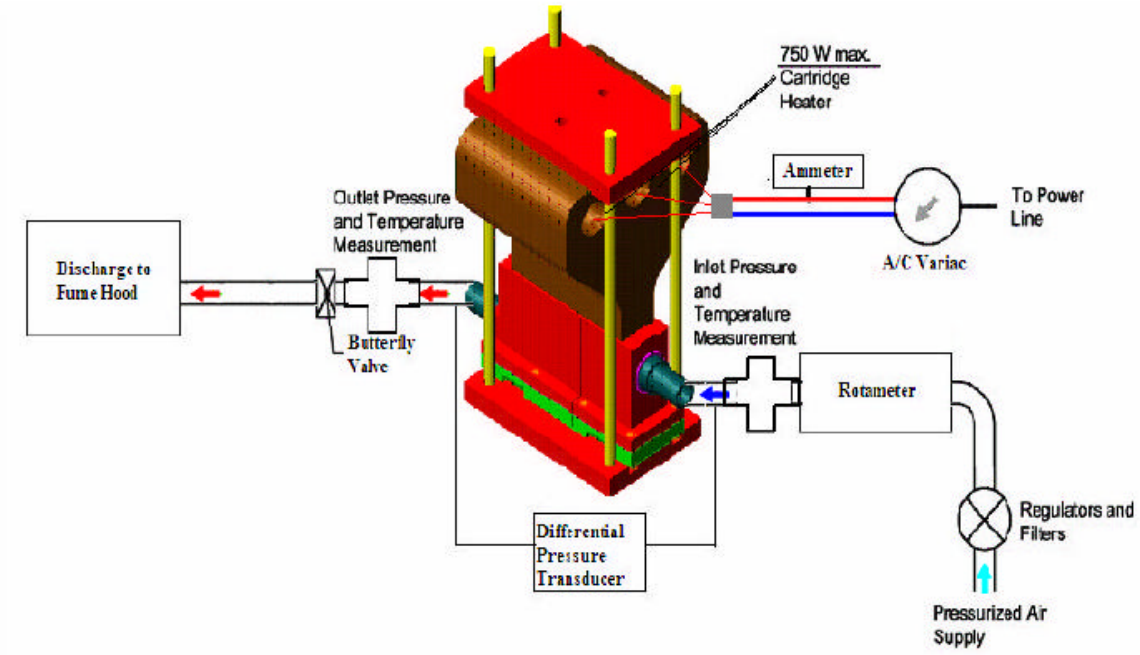

Figure 2.15: Diagram of the air flow loop.

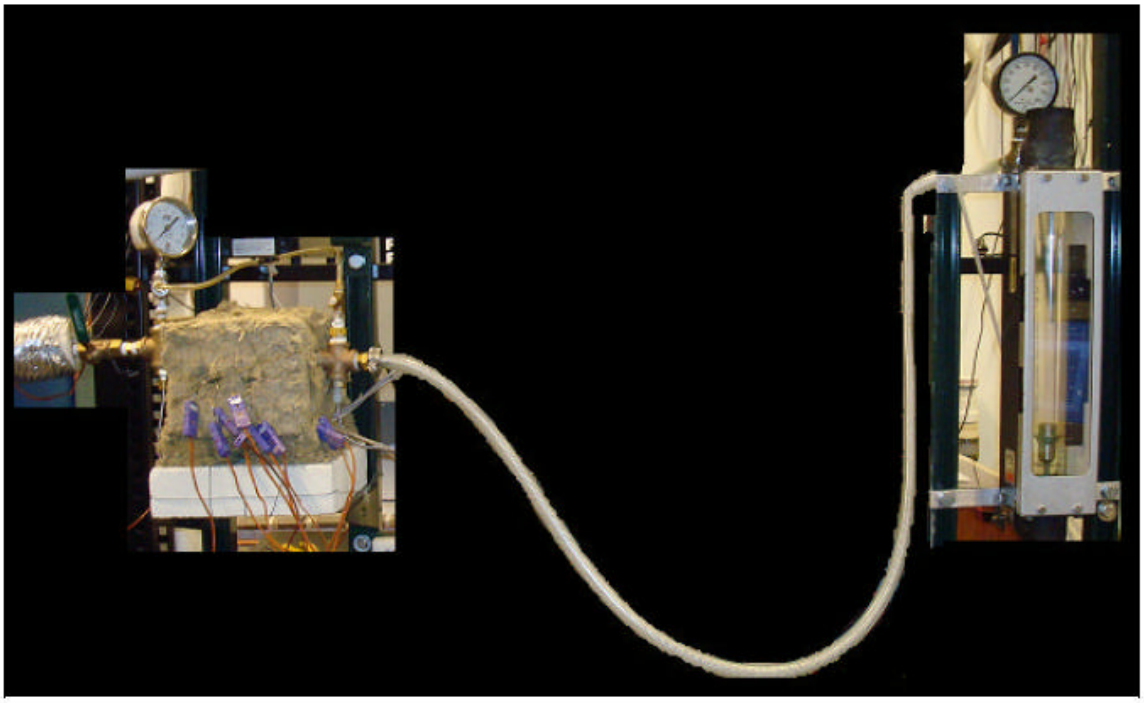

Figure 2.16: Photograph of the test section with instrumentation attached.

Details of the coolant flow path through the various test modules are shown in Figure 2.17. Air at room temperature (~22°C) enters the inlet manifold and is accelerated through the jet (slot or holes) toward the cooled surface. In the cases without foam, the stagnation point flow generated by the jet impingement directly cools the inner surface of the outer shell, which corresponds to the divertor heat removal surface. Downstream of the stagnation location, the air forms a turbulent wall jet and is pushed to the outer walls, flows down the gaps between the inner cartridge and outer shell and through the holes on the side of the inner cartridge into the outlet manifold, from which it exits on the opposite side of the test module. In the cases with foam insert, the high speed coolant coming out of the jets must pass through the foam before reaching the cooled surface. Some of the coolant may be diverted to the outer walls without ever reaching the cooled surface. The remainder of the flow path is the same as in the cases with no foam.

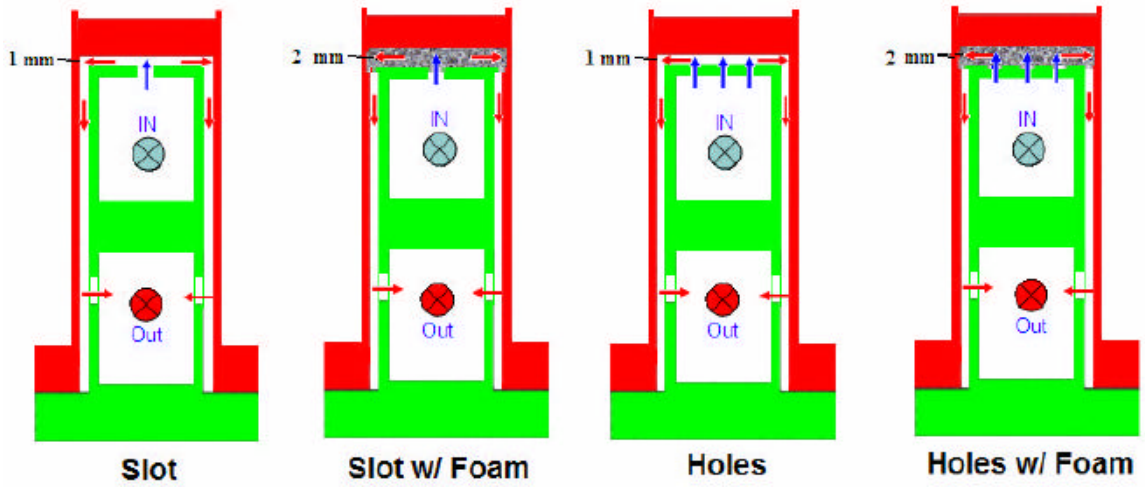

Figure 2.17: Coolant flow through test modules (cross-sectional view).

The data acquisition system consists of a 60-channel data acquisition unit (Agilent 34970, with three A/D cards #34901A, each having 20-channels). It is connected to a PC through a RS-232 serial cable. The Agilent Bench Link Data Logger 3 software is used to configure the unit and monitor the data on the PC. Only steady state data is stored for each experiment.

2.2 Experimental Parameters and Procedures

The operating conditions of the air flow loop have been selected to span the most important dimensionless group of the actual HCFP divertor module, namely, the Reynolds number *Re* based on either the hydraulic diameter of the slot in the inlet manifold $D_h = 2W = 4\,mm$ (where W is the slot width) or the jet hole diameter $D = 0.8\,\mathrm{mm}$, the average speed ($\overline{V} \circ \dot{m} / \rho A$) where A denotes either the area of the slot or the total area of the holes), and the viscosity at the test section inlet μ_{in}.

$$\mathrm{Re}_{sl} = \frac{\dot{m} D_h}{A_{sl} \mu_{in}} \qquad \text{or} \qquad \mathrm{Re}_h = \frac{\dot{m} D}{A_h \mu_{in}} \tag{2.1}$$

For the same $\dot{m}$ and μ_{in}, the Reynolds number for the geometry with the array of holes is approximately twice that for the geometry with the slot, since A_{sl} = 1.5 cm^2, about an order of magnitude larger than A_h = 0.16 cm^2. For the slot experiments, the Reynolds number varies from 1.3×10^4 to 5.6×10^4, corresponding to a mass flow rate ranging from 9.0 g/s to 40.2 g/s. The holes experiments cover a Reynolds number range of 1.1×10^4 to 6.8×10^4, corresponding to a mass flow rate range of 4.6 g/s to 26.2 g/s. The

Reynolds number, based on the 0.5 mm slot, expected for the baseline HCFP divertor design is 33,000 (Wang, 2008b).

Experiments were performed at nominal heat fluxes ranging from 0.22 MW/m^2 to 0.9 MW/m^2. The nominal incident heat flux q''_{nom} is the ratio of the total power input to the cartridge heaters and the area of the concentrator "neck" of 1.67×10^{-3} m^2. The power input was selected such that the peak temperature in the copper block never exceeded 500°C (half the melting point of C14500 copper alloy). Table 2.3 details the nominal operating conditions of the ARIES HCFP divertor and the GT baseline test module (slot) in an air flow loop. The difference between the Prandtl numbers of air (0.73) and helium (0.66) is deemed to have a small effect on the measured Nusselt number (and thus the convective heat transfer coefficient) since for turbulent flows **Nu** depends on **Pr** to the 0.4 power (Gardon and Akfirat, 1966).

Table 2.3: Comparison of thermal-hydraulic parameters for the HCFP and the GT experimental study (slot-design) using air.

Coolant	**T_{in}** [°C]	**P_{sys}** [MPa]	**q''_{nom}** [MW/m^2]	**$\dot{m}$** [g/s-m]	**Re** [x 10^3]	**Pr** [-]
He (ARIES)	600	10	10.0	702	33	0.66
Air (GT)	21.6-23.5	0.116-0.524	0.22-0.9	61-527	11-68	0.73

Each experiment is performed as follows:

1. The Agilent acquisition unit, voltage multi-meter, and power supply are switched on. The BenchLink Data Logger 3 software is opened and data scanning is initiated.

2. The power supply is adjusted to the desired value by turning the dial on the variable autotransformer while monitoring the voltage and current: $P=I*V$. The temperatures are monitored with the Data Logger software. The lowest heat flux (0.22 MW/m^2) required a voltage/current combination of 51 Volts and 7.25 Amps, while the highest heat flux (0.9 MW/m^2) required 100 Volts and 14.9 Amps.

3. Once the test section temperatures have risen to near the expected steady state values, the air supply is turned on. The mass flow rate is adjusted to the desired value via the butterfly valve at the test section outlet and the pressure regulator, which controls the pressure of the air supplied to the system. The "uncorrected" volumetric flow rate, **scfm,** is read from the rotameter (with a resolution of 0.25 scfm) and the pressure at the exit of the rotameter is recorded. This volumetric flow rate must be corrected for pressure and multiplied by density to obtain the mass flow rate (Equation 2.2).

$$\dot{m}\left(\text{kg}/\text{s}\right) = \text{scfm}* \sqrt{\frac{14.7\text{psia}}{p_{rot}(\text{psia})}} * \rho_{rot}\left(\text{kg}/\text{m}^3\right) * \frac{1\ \text{m}^3}{35.3\ \text{ft}^3} * \frac{1\ \text{min}}{60\ \text{sec}} \qquad (2.2)$$

   a. Several iterations are usually necessary to obtain the desired mass flow rate using this method.

4. Once the temperatures in the test section reach steady state, the data is recorded. The flow is considered to have reached "steady-state" when the temperatures

measured by the TCs in the cooled surface vary by no more than 1 °C over 2 minutes. Each experiment took about 45 min to reach steady-state.

The tests span a large range of *Re* and q''_{nom} to evaluate the dependence of HTC on operating conditions, i.e. the robustness of the design. In general, each configuration is tested at a Low Flow/Low Power, Medium Flow/Medium Power and High Flow/High Power combination. Supplementary experiments were sometimes performed to test various effects (e.g. effect of pressure on the predicted temperature distribution for the same *Re* and q''_{nom}) . Additionally, in some cases, test loop limitations (e.g. inability to reach the highest desired mass flow rate) limited the number of experiments performed for some configurations. However, a sufficient number of experiments has been performed for each configuration to allow at least two sets of comparisons to be performed between configurations. Comparisons between configurations are made by: (1) holding $\dot{m}$ and q''_{nom} constant and (2) holding *Re* and q''_{nom} constant.

The net heat flux q''_{net} is shown alongside q''_{nom} since heat losses will cause the actual heat flux incident on the brass surface to be slightly lower than the nominal value. To provide an estimate of the actual heat flux q''_{net}, the TCs located in the neck of the copper heater are used, along with the conductivity of C14500 copper, k_c =354.8 W/m-K, and the distance between TC beads L_i. A heat flux is calculated between each pair of TCs in an *x*-*z* plane, (i.e. 9-10, 10-11, 9-11, 6-7, 7-8, and 6-8). The net heat flux is calculated with the following formula:

$$q''_{net} = average\left(\frac{k_c}{L_i}\Delta T_i\right), \text{ where: } i = \text{9-10, 10-11, 9-11, 6-7, 7-8, and 6-8.} \qquad (2.3)$$

Since the inlet pressures vary between the experiments, it is necessary to normalize the pressure drops ΔP to a common system pressure P_{sys}, where P_{sys} is defined as the average of the inlet and outlet pressures. It is known that ΔP scales with the dynamic pressure $\rho \bar{V}^2/2$, which in turn is proportional to $\dot{m}^2/\rho$. Therefore, for a given $\dot{m}$, $\Delta P \propto 1/\rho \propto 1/P_{sys}$. All the measured pressure drops were therefore rescaled to a common pressure P_{nom} = 414 kPa (60 psia), by multiplying the pressure drops by P_{sys} and dividing by P_{nom}. The normalized pressure drop $\Delta P'$ is defined as follows: $\Delta P' \equiv \Delta P \, (P_{sys} / P_{nom})$. This normalization allows the pressure drop obtained for different test conditions and configurations to be directly compared.

2.2.1 Circular Jets Experiments

This section describes the experiments conducted using the inner cartridge with an array of circular holes (hereafter referred to as the "*Holes*" experiments). Details of the *Holes* experiments performed with no foam are presented in Table 2.4. *Holes* tests 1, 4, and 8 were performed to evaluate the effect of a lower system pressure on the HTC while maintaining the same Reynolds number. They are also used to check the adequacy of the pressure normalization method for pressure drop comparison. Tests 6 & 7 were performed to verify the repeatability and sensitivity of the experiment.

Table 2.4: List of the experiments performed with the array of holes configuration.

Exp. #	$\dot{m}$ [g/s]	Re [-]	q''_{nom} [MW/m^2]	q''_{net} [MW/m^2]	P_{in} [kPa]	DP' [kPa]
Holes-1	4.6	12,000	0.22	0.21	123.5	4.3
Holes-2	4.6	12,000	0.22	0.21	269.7	4.1
Holes-3	9.2	24,000	0.22	0.20	502.7	18.2
Holes-4	13.2	34,000	0.49	0.45	223.5	32.1
Holes-5	13.3	35,000	0.49	0.45	505.4	33.6
Holes-6	25.6	66,000	0.49	0.43	538.3	98.4
Holes-7	26.2	68,000	0.49	0.42	534.6	101.1
Holes-8	21.3	56,000	0.62	0.56	325.0	71.7
Holes-9	21.3	55,000	0.62	0.56	466.9	75.5

2.2.2 Circular Jets Experiments with 65 ppi Foam

Table 2.5 details the experiments conducted using the inner cartridge containing an array of circular holes with a 65 ppi Molybdenum foam insert placed in the gap between the cartridge and the cooled surface (hereafter referred to as the "*Holes-65*" experiments). The *Holes-65* tests span the same range of *Re* as the cases without foam. Comparisons between the results of the "*Holes*" and the "*Holes-65*" have been made on the basis of average change in HTC and △P' (see Chapter 5). One notable feature of Table 2.5 is that q''_{net} is sometimes greater than q''_{nom}. The reason for this is not fully understood. The leading hypothesis is that the conductivity of copper is not constant with respect to temperature as assumed in the calculation. Negative heat loss values ($q''_{nom} > q''_{net}$) occur only in the cases with foam insert and where the average temperature of the TCs located in the copper is less than 200°C, suggesting the actual conductivity of copper is lower than that used in the calculation. However, *Holes-3* and *Slot-1* and *Slot-100-1* also have average copper TC temperatures below 200°C, without negative heat

losses. Therefore, this effect may simply be due to fluctuations/uncertainty in experimental measurements.

Table 2.5: List of the experiments performed with the array of holes with 65 ppi foam configuration.

Exp. #	$\dot{m}$ [g/s]	Re [-]	q''_{nom} [MW/m^2]	q''_{net} [MW/m^2]	P_{in} [kPa]	$\Delta P'$ [kPa]
Holes-65-1	4.6	12,000	0.22	0.24	268.8	10.0
Holes-65-2	8.8	22,000	0.22	0.24	504.4	32.4
Holes-65-3	13.3	35,000	0.49	0.48	509.2	57.7
Holes-65-4	13.7	36,000	0.49	0.48	506.7	62.3
Holes-65-5	24.9	65,000	0.49	0.49	470.0	201.7
Holes-65-6	26.2	68,000	0.49	0.50	495.6	223.6

2.2.3 Slot Experiments

Table 2.6 details the *Slot* experiments that were performed using the slotted inner cartridge without a foam insert. The tests correspond to either the same (*Re*, q''_{nom}) combination or the same ($\dot{m}$, q''_{nom}) combination as the cases performed with the array of holes (with and without foam) and the slot with foam cases. Comparisons between the experiments are made in Chapter 5. Since the slot configuration is most similar to the HCFP design, it is taken as the nominal or baseline design of these studies. All comparisons of HTC enhancements or increases in $\triangle$P' are made with respect to the comparable (i.e., same mass flow rate and heat flux) *Slot* experiment.

Table 2.6: List of the experiments performed with the slot configuration.

Exp. #	$\dot{m}$ [g/s]	Re [-]	q''_{nom} [MW/m^2]	q''_{net} [MW/m^2]	P_{in} [kPa]	DP' [kPa]
Slot-1	9.0	13,000	0.22	0.21	526.9	6.3
Slot-2	25.7	36,000	0.49	0.47	428.7	50.2
Slot-3	38.0	53,000	0.62	0.59	477.4	118.9
Slot-4	40.1	56,000	0.74	0.71	494.8	127.1

2.2.4 Slot Experiments with 45 ppi Foam

This section describes the experiments conducted using the slotted inner cartridge while placing a 45 ppi Molybdenum foam insert in the gap between the inner cartridge and outer shell (hereafter referred to as the "*Slot-45*" experiments). Table 2.7 details the *Slot-45* experiments performed in this investigation. The tests correspond to the same (*Re*, q''_{nom}) combination or the same ($\dot{m}$, q''_{nom}) combination as the *Holes*, *Holes-65*, *Slot*, *Slot-100*, and *Slot-65* cases. Comparisons of HTC and △P' among the various configurations are made in Chapter 5. Only a Low flow/Low Power experiment and Medium flow/Medium Power experiment were performed for this configuration, since the house line for compressed air was incapable of producing the high flow rate attained in earlier experiments because of higher demand from other building occupants.

Table 2.7: List of the experiments performed with the slot with 45 ppi foam configuration.

Exp. #	$\dot{m}$ [g/s]	Re [-]	q''_{nom} [MW/m^2]	q''_{net} [MW/m^2]	P_{in} [kPa]	$\Delta P'$ [kPa]
Slot_45-1	9.0	13,000	0.22	0.23	520.1	14.8
Slot_45-2	26.2	37,000	0.46	0.45	590.0	100.1
Slot_45-3	26.0	37,000	0.49	0.46	462.7	99.2

2.2.5 Slot Experiments with 65 ppi Foam

This section describes the experiments conducted using the slotted inner cartridge while placing a 65 ppi Molybdenum foam insert in the gap between the inner cartridge and outer shell (hereafter referred to as the "*Slot-65*" experiments). Table 2.8 details the *Slot-65* experiments performed in this investigation. The tests correspond to the same (Re, q''_{nom}) combination or the same ($\dot{m}$, q''_{nom}) combination as the *Holes*, *Holes-65*, *Slot*, *Slot-100*, and *Slot-45* cases. Comparisons of HTC and △P' among the various configurations are made in Chapter 5.

Table 2.8: List of the experiments performed with the slot with 65 ppi foam configuration.

Exp. #	$\dot{m}$ [g/s]	Re [-]	q''_{nom} [MW/m^2]	q''_{net} [MW/m^2]	P_{in} [kPa]	$\Delta P'$ [kPa]
Slot-65-1	9.0	13,000	0.22	0.23	524.4	11.7
Slot-65-2	26.0	36,000	0.49	0.50	456.1	73.1
Slot-65-3	40.1	56,000	0.62	0.61	528.0	180.4
Slot-65-4	40.2	56,000	0.90	0.85	533.5	184.4

2.2.6 Slot Experiments with 100 ppi Foam

This section describes the experiments conducted using the slotted inner cartridge while placing a 100 ppi Molybdenum foam insert in the gap between the inner cartridge and outer shell (hereafter referred to as the "*Slot-100*" experiments). Table 2.9 details the *Slot-100* experiments performed in this investigation. The tests correspond to the same (Re, q''_{nom}) combination or the same ($\dot{m}$, q''_{nom}) combination as the *Holes*, *Holes-65*, *Slot*, *Slot-45*, and *Slot-65* cases. Comparisons of HTC and $\triangle$P' among the various configurations are made in Chapter 5. As in the *Slot-45* experiments, only a Low Flow/Low Power experiment and Medium Flow/Medium Power experiment were performed for this configuration, since the house line for compressed air was incapable of producing the high flow rate attained in earlier experiments because of higher demand from other building occupants.

.

Table 2.9: List of the experiments performed with the slot with 100 ppi foam configuration.

Exp. #	$\dot{m}$ [g/s]	Re [-]	q''_{nom} [MW/m^2]	q''_{net} [MW/m^2]	P_{in} [kPa]	$\Delta P'$ [kPa]
Slot-100-1	9.0	13,000	0.22	0.21	520.1	14.8
Slot-100-2	26.2	37,000	0.49	0.47	463.6	106.2

CHAPTER III

NUMERICAL MODEL

This chapter describes the numerical model used to simulate the HCFP divertor test module. Because of the the level of effort involved in setting up the mesh for the complex test module geometries used in this investigation, only the test module geometry with the array of holes has been simulated. The chapter is organized as follows. First, the geometry of the HCFP numerical model is described, followed by the mesh generation methodology. Next, the boundary conditions applied to the model are described. The turbulence models examined in this study are discussed, followed by a short section on convergence criteria. Finally, general numerical results, such as contour plots of static temperature and heat transfer coefficient and velocity pathlines are presented.

3.1 HCFP Geometry

The HCFP divertor test section model used for the numerical studies detailed in this chapter was constructed in Gambit® 2.2.30. Because of geometric symmetry, a half model is used for all the simulations. The model includes the aluminum inner cartridge, silicone rubber gasket, brass outer shell, brass inlet and outlet tubes, and the copper heater block including the cartridge heaters (Figure 3.1). These components are modeled in three-dimensions and include all pertinent features present in the experimental test section as described in Chapter 2. The material properties used in the numerical model are provided in Table 3.1.

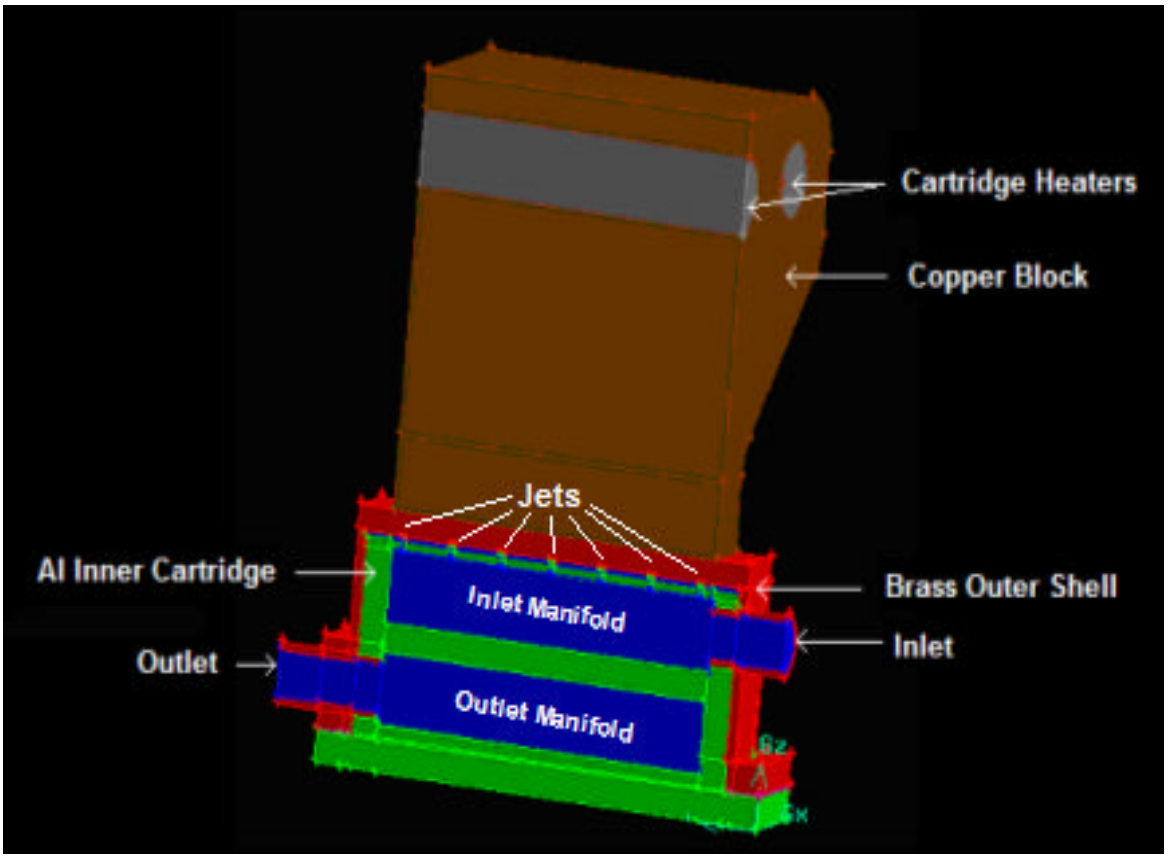

Figure 3.1: Diagram of the HCFP divertor test section numerical model.

Table 3.1 Table of the materials used in the numerical model.

Material	Component	Density [kg/m^3]	Thermal Conductivity [W/m-K]	Specific Heat [J/kg-K]
Air	Coolant	Ideal Gas	0.0242	1006.43
Aluminum	Inner Cartridge	2719	202.4	871
Brass C3600	Outer Shell	8500	116	380
Copper C14500	Heater Block	8940	354.8	376.8
Magnesium Oxide	Cartridge Heater	3580	T [K] / k: 273 / 42; 400 / 29; 600 / 20; 800 / 14; 1000 / 11	877
Silicon Rubber	Gasket	1200	0.2	1255

3.2 Mesh Generation

The mesh was constructed using Gambit® 2.2.30. The final grid used in the numerical simulations consists of 1.67 x10^6 cells with 766,000 nodes (Figure 3.2). A structured mesh was used whenever possible, by projecting face meshes along "mapped" side faces to create a volume mesh. A mapped face is similar to a checkerboard; it must have an equal number of nodes on parallel faces so that rows and columns may be formed. This method of meshing, known as Cooper meshing, only allows a face made of multiple faces to be projected onto a single face, not vice versa. For instance the face on the top of the inner cartridge with the array of holes is a face made of multiple faces. Nothing can be swept onto this face. The only option that will allow a structured mesh in this region is to first mesh the complex face, then mesh the side faces of the gap region

with a map and sweep the complex face mesh onto the single cooled surface. This is the very first thing done in the mesh generation process. The rest of the structured mesh builds off this initial choice, so it is imperative that the resolution in this region is chosen wisely.

The general guideline for generating the mesh is to conceptually picture the flow through the test module. Using physical intuition, identify the areas that are most likely to impact the solution and/or have complex flows. Then, generate a mesh that can resolve the major flow features expected. The FLUENT user guide (Section 6.2.2) states the following about the importance of mesh resolution in turbulent flows:

"Proper resolution of the mesh for turbulent flows is also very important. Due to the strong interaction of the mean flow and turbulence, the numerical results for turbulent flows tend to be more susceptible to grid dependency than those for laminar flows. In the near-wall region, different mesh resolutions are required depending on the near-wall model being used. In general, no flow passage should be represented by fewer than 5 cells. Most cases will require many more cells to adequately resolve the passage. In regions of large gradients, as in shear layers or mixing zones, the grid should be fine enough to minimize the change in the flow variables from cell to cell."

For this study, a node spacing of 0.25 mm was chosen for the perimeter of the jet to give a total of 20 nodes around the jet perimeter. The bottom of the jet was meshed with 72 triangles of approximately equal area. Triangles were chosen instead of quadrilateral elements, since unstructured tetragonal meshes generally perform better (have lower skewness values) when surrounded by triangular faces. A size function was applied to the face mesh of the inner cartridge to allow a fine mesh in the region of high

velocity gradients (near the jet/stagnation point) and a coarser mesh as the velocity gradients decrease (away from a jet). The size function imposed a cell growth rate of 10% with a maximum node spacing of 0.4, as it moves away from a jet (Figure 3.2). This face mesh is swept upwards, through the top air gap, onto the cooled surface. Therefore, the *x-y* spacing shown in Figure 3.2 is characteristic of the entire impingement region. The axial spacing of the impingement region is shown in Figure 3.3. A spacing of 0.1 mm was chosen for the flow direction in the jets, the top gap/impingement region (+*z*) and the side gap/exiting flow (-*z*).

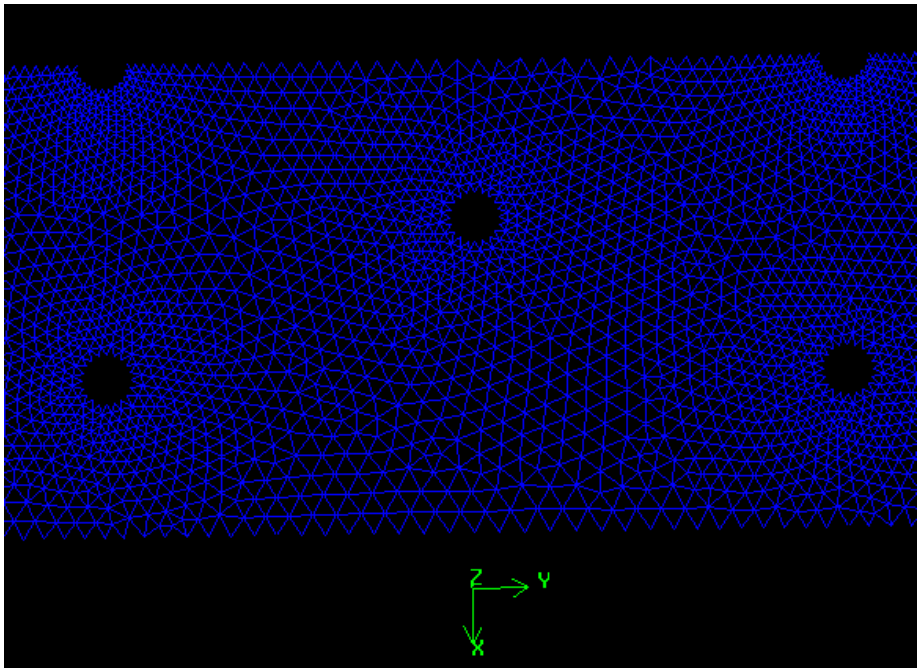

Figure 3.2: Face mesh surrounding the jets (x-y) plane

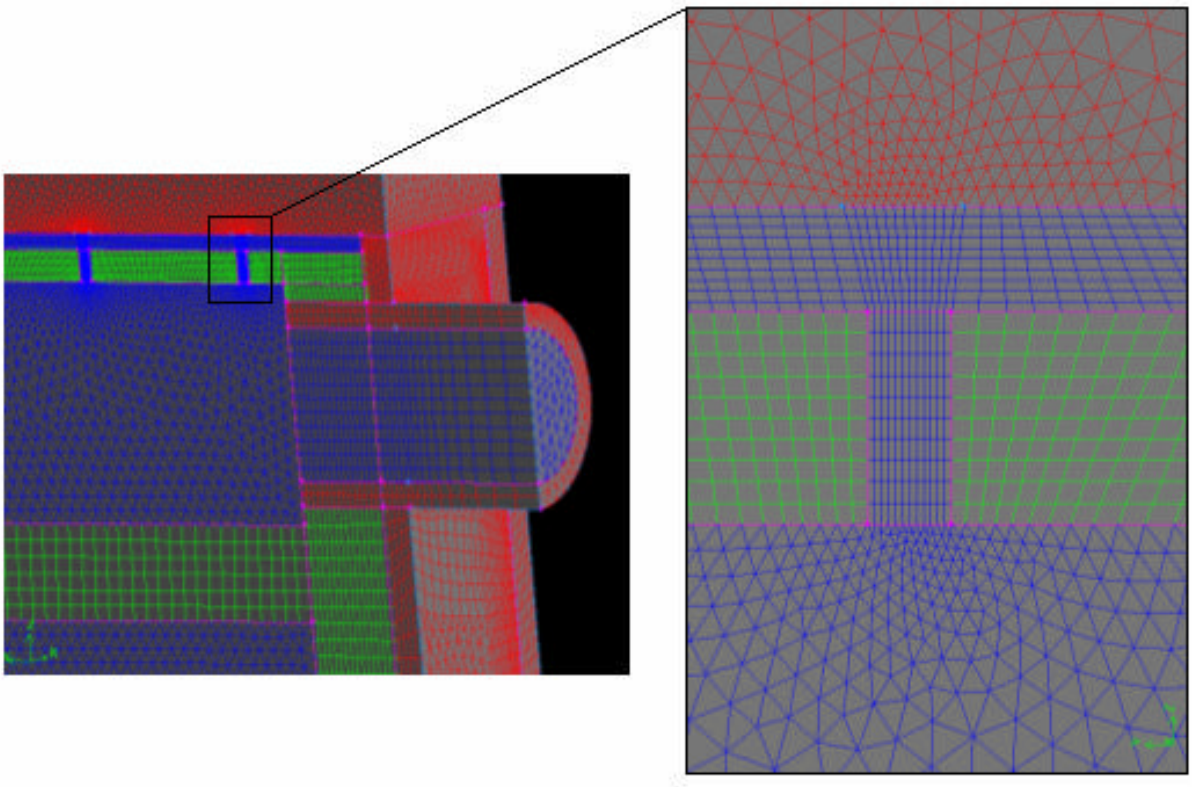

Figure 3.3: Close-up view of mesh in the jet and impingement region (*y*-*z* plane)

In some cases it is not possible to use a structured mesh; two such cases in this grid were the inlet manifold (Fig. 3.3, bottom right - blue) and the top of the brass shell (Fig 3.2, top right - red). The inlet manifold could not be meshed with a structured mesh because all of the sides could not be meshed with a map scheme, due to the connection with the curved inlet tube. The top of the brass shell could not be meshed with a cooper mesh, since the lower face (cooled surface) is already meshed (by projection of the top surface of the inner cartridge) and the top face consists of multiple faces, due to the connection with the copper heater. However, even if a structured mesh is possible, it is not always the best choice. Since the mesh is very fine in the impingement region (0.1 mm node spacing), and a structured mesh requires mapped faces, with equal number of

nodes on the top and bottom edges of the face, this tight node spacing would be carried throughout the rest of the test module (143 mm in height). Clearly, this is an undesirable outcome, and a waste of computer resources. With unstructured meshes, it is possible to grow the size of the cell through user defined size functions or by defining the node spacing on the other faces and letting FLUENT choose the growth rate. An example of tetragonal cell growth can be seen in Figure 3.3 (right).

Once all volumes are meshed, with a skewness value less than 0.97, the grid is imported into FLUENT. If it is desired to change the mesh size in the impingement region, it is necessary to delete the entire mesh and start over. The only exception to this is if an unstructured mesh surrounds (isolates) the initial structured mesh. Structured meshes built outside of unstructured meshes may be retained. The copper block and heater cartridges, for example, would not need to be remeshed if the same mesh spacing is left on the face joining the brass shell and the copper heater. However, a very fine mesh in the impingement region may necessitate smaller spacing throughout the top of the brass shell and the copper block. FLUENT does offer a grid adaption feature that allows refinement of the grid based on pressure, velocity, and temperature gradients, as well as volume size, without re-meshing in GAMBIT. Efforts were made to utilize this feature in this study; however, the amount of memory required exceeded the capabilities of the computer used. The completed mesh used for the array of holes numerical studies is shown in Figures 3.4.

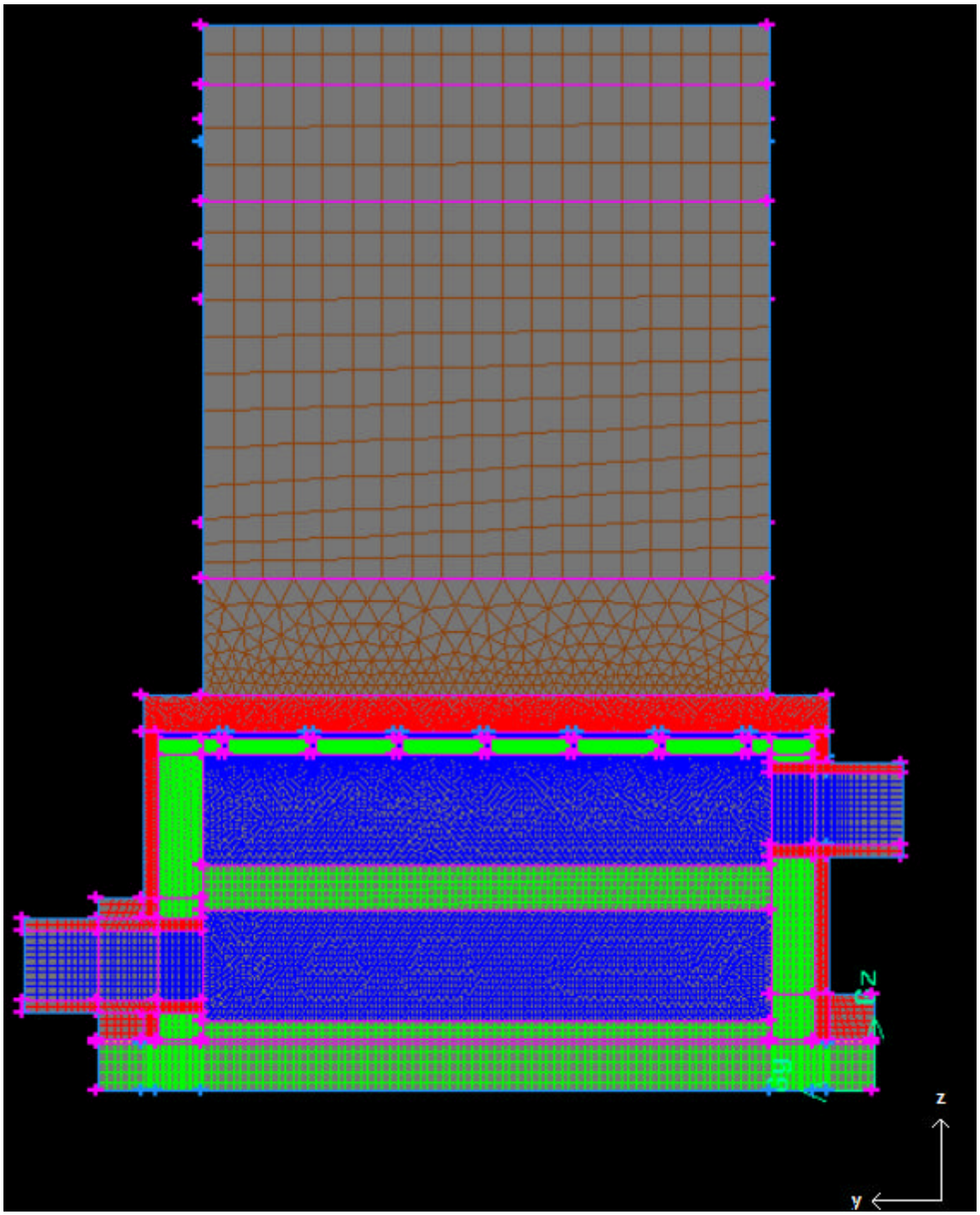

Figure 3.4: Full model final mesh.

3.3 Boundary Conditions

The boundary conditions applied to the test section model when used for comparison with experimental data are described in this section and detailed in Table 3.2. Quantities marked with an asterisk in Table 3.2 denote values that are experiment-specific. These values include: mass flow rate, power input, inlet and outlet temperatures and pressures, and turbulent intensity. The turbulence intensity at the inlet and exit is taken to be equal to the fully-developed value which can be estimated from the following formula (FLUENT 7.2.2).

$$I = 0.16(\mathrm{Re}_{Inlet})^{-1/8} \tag{3.1}$$

For compressible flows, if a mass flow rate at the inlet is known, FLUENT recommends the use of a mass flow inlet boundary condition, as is the case in this study (FLUENT 7.2.1). Pressure outlet boundary conditions are used to define the static pressure at flow outlets. Although, the inlet pressure and temperature are specified in the mass flow inlet boundary condition, FLUENT uses these more as initial conditions, than boundary conditions. FLUENT will adjust these values to the "correct" pressure and temperature conditions at the inlet that correspond to the given mass flow rate and outlet pressure. Therefore, if the final inlet temperature and pressure are far from the initial values, either the experimental data (mass flow rate, pressure drop, or inlet/exit temperature and pressure measurements) are in error, or FLUENT is doing a poor job predicting the pressure drop.

The power input to the heaters is specified as a volumetric heat generation rate. The combined volume of the three heaters is 4.52×10^{-5} m^3. The required power inputs for the three most commonly used heat fluxes is as follows: 370 W for q''_{nom} = 0.22 MW/m^2;

820 W for q''_{nom} = 0.49 MW/m^2; and 1,035 W for q''_{nom} = 0.62. The outer surfaces of the test module, i.e. the surfaces in contact with the insulation, were imposed with perfectly insulated boundary conditions (no heat loss). An alternative approach would have been to include the insulation surrounding the test section in the numerical model and apply the natural convection heat transfer coefficient to the outer surfaces of the insulation. However, this would have required significantly more cells and computer memory. Initial attempts were made to incorporate this functionality, but skewness values above 0.97 were obtained. To resolve this, it would have been necessary to change the outer faces of the model, which would essentially mean remeshing the entire model. Since experimental heat losses were measured to be <10% in most cases, the perfectly insulated condition was deemed suitable. Additionally, the temperatures of the outer surfaces of the insulation were measured with a non-contact infrared thermometer (Raytek ST^{TM} Pro) and a heat loss estimation based on natural convection was performed. These calculations also found low heat losses, typically on the order of ~5%. Therefore, one would expect the temperatures of the cooled surface TCs in the perfectly insulated numerical model to be slightly higher than the corresponding experimental values.

Table 3.2: Detailed list of the boundary conditions and their parameters

Name	Momentum BCs	Thermal BCs
Outer surfaces (in contact with insulation) -Al base -Brass shell -Copper Block	N/A	Heat Flux = 0 W/m^2 Heat Gen. Rate = 0 W/m^3
Cooled Surface	<u>Stationary Wall</u> No Slip Shear Condition Roughness Height = 0 m Roughness Constant = 0.5	Coupled Heat Gen. Rate = 0 W/m^3
Inlet	<u>Mass Flow Inlet</u> Mass Flow Rate = * Initial Gauge Pressure = * Turbulent Intensity = * Hyd. Diameter = 9.53 mm	Tot. Temperature = *
Cartridge Heaters	N/A	Source Terms = 1 Constant = * W/m^3
Midplane	Symmetry	Symmetry
Outlet	<u>Pressure Outlet</u> Gauge Pressure = * Turbulent Intensity = * Hyd. Diameter = 9.53 mm	Backflow Tot. Temperature = *

3.4 Turbulence Models

Although no single turbulence model is universally accepted as being superior for all types of problems, the standard k-ε model has been shown to provide an excellent match to experimental results in similar 3-D, turbulent jet impingement studies (Crosatti, 2008 and Weathers, 2007). The k-ε models are regarded as the simplest "complete model" of turbulence in which the solution of two separate transport equations allows the turbulent velocity and length to be independently determined (Fluent 12.4.1). It is perhaps the most popular turbulence model for industrial flows and heat transfer simulations due to its "robustness, economy, and reasonable accuracy for a wide range of turbulent flows" (Fluent 12.4.1). For high-Mach-number flows, such as those experienced in this investigation, compressibility affects turbulence through "dilatation dissipation." This effect is automatically taken into account when the ideal gas law for density is used (FLUENT 12.4.6).

Although the standard k-ε model is primarily valid for turbulent core flows (i.e., the flow in the regions far from walls), the use of semi-empirical formulas called "wall functions" makes the model suitable for wall-bounded flows (FLUENT 12.10.1). In most high Reynolds number flows, such as those studied here, the wall function approach is considered economical, robust, and reasonably accurate (FLUENT 12.10.1). FLUENT offers several choices of wall functions: (1) standard (default); (2) non-equilibrium; (3) enhanced wall treatment; and (4) user-defined functions. Standard wall functions are the most widely used by industry and are considered reliable provided that the near wall flows are not in strong non-equilibrium or subjected to severe pressure gradients (FLUENT 12.10.2). Standard wall-functions were used in the earlier helium-cooled

divertor modeling studies of Crosatti (2008) and Weathers (2007) with excellent results. As a result, the standard k-e closure equations with standard wall functions were used as the baseline turbulence model for all simulations.

However, FLUENT recommends the use of non-equilibrium wall functions for complex flows such as "*impingement"* where the mean flow and turbulence are subjected to severe pressure gradients and change rapidly. In such flows, improvements can be obtained, "particularly in the prediction of wall shear (skin-friction coefficient) and *heat transfer"* (FLUENT 12.10.3, emphasis mine). Therefore, three cases were run with the non-equilibrium wall functions in place of the standard wall functions. The impact of the wall function choice is discussed in Chapter 4.

The enhanced wall treatment wall functions are primarily useful for intermediate size meshes ($3 < y^+ < 10$) that are too fine for the near-wall centroid to lie in the fully turbulent region, but too coarse to properly resolve the laminar sublayer. Generally speaking, this is not the case in our studies. It should be remembered that y^+ is a solution-dependent quantity; for the cases examined here, the near jet y^+ values ranged from 20-58 for the low flow case, 55-111 for the medium flow case (Figure 3.5), and 99-238 in the high flow case. Although, y^+ values as low as 2 were obtained around the periphery of the cooled surface, this should not significantly impact the HTC predictions in the near jet regions.

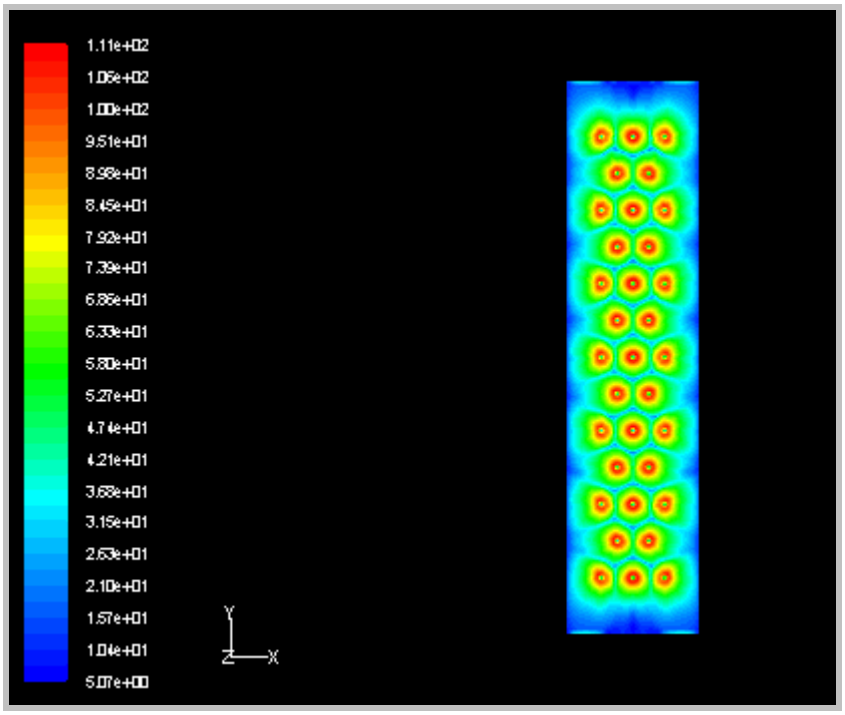

Figure 3.5: Contours of y^+ on the cooled surface for the medium flow case

An alternative to the wall function approach is to use a fine resolution mesh capable of resolving the flows in the laminar sublayer. This requires y^+ values near unity. Therefore the grid described above would need to be refined by nearly two orders of magnitude, which would certainly not be feasible for the full scale model shown here. A small slice of the test section with the appropriate boundary conditions would be required. A new mesh would be needed for each mass flow rate, since y^+ is dependent upon the flow. Additionally, the standard k-e model would not be applicable. The turbulence model used in these simulations should give accurate results throughout the near wall region. Examples of applicable turbulence models for this approach are the Spalart-Allmaras and k-? model.

3.5 Convergence

Convergence of the numerical simulation was determined by noting that the residuals had reached a nearly constant value. The standard order of magnitude for the residuals was at least 10^{-3} and decreased to 10^{-7} for the energy equation (Figure 3.6). Generally 300 iterations were sufficient to provide this level of convergence on a Pentium® IV 3.4 GHz workstation with 2 GB of RAM. However, trial cases were run up to 1,000 iterations, to see if the solution could be improved with further iterations. The result of these investigations was that the temperatures of the TCs in the cooled surface changed by ~0.1% between 100 and 1000 iterations. A surface monitor of the inlet pressure was also used as a measure of convergence (Figure 3.7).

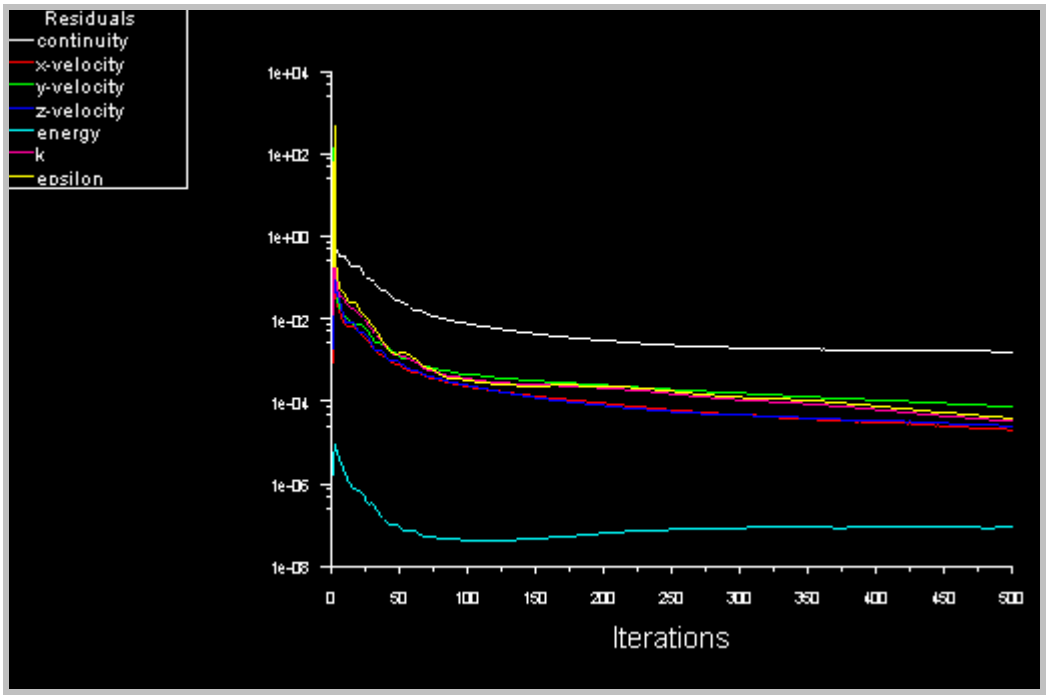

Figure 3.6: Plot of the residuals for a converged FLUENT® simulation.

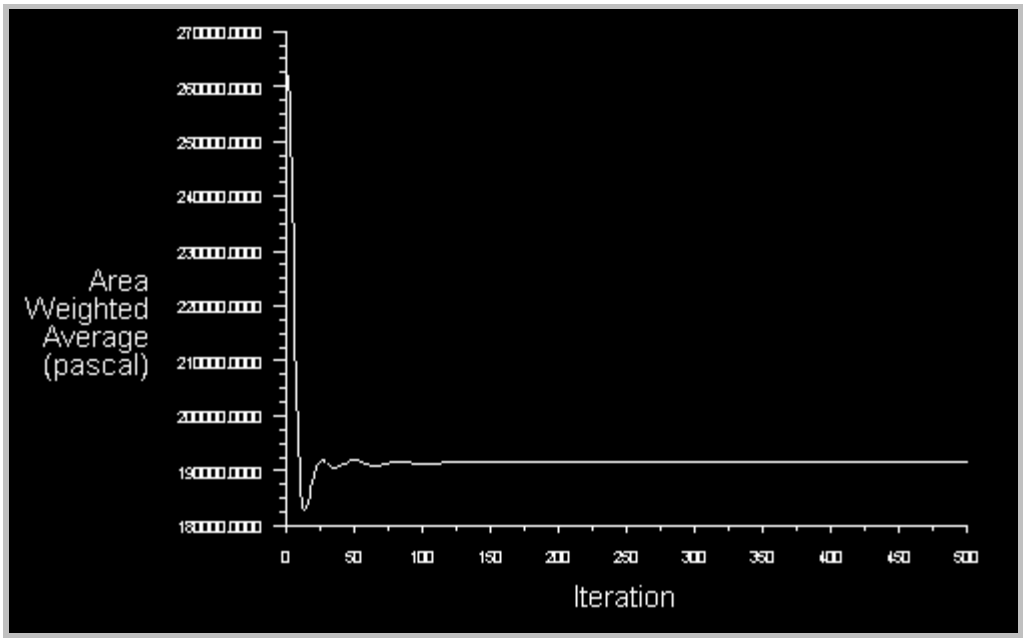

Figure 3.7: Plot of the surface integral monitor of inlet pressure for a converged FLUENT® simulation.

3.6 Nominal Case Results

This section provides an overview of the performance and predictions of the numerical model for a single case, namely the Medium flow/Medium power case for the array of holes test module with the Spalart-Allmaras turbulence model. The Reynolds number in this case is 35,000 which is similar to the reference value of the original 0.5 mm slot HCFP design of 33,000 (Wang 2008b). Figure 3.8 shows the temperature distribution of the HCFP divertor test section model. The fairly flat temperature distributions along the x-*y* planes in the neck region of the copper heater implies a nearly uniform incident heat flux in the axial, i.e., z dimension in the center of the heater (i.e., away from the edges of the copper block).

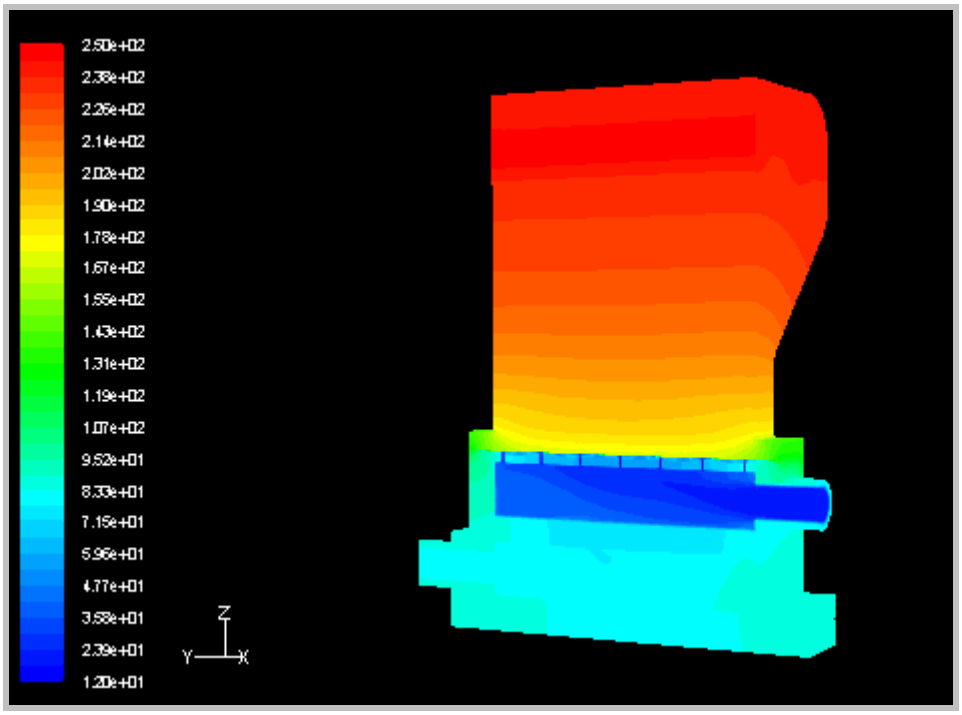

Figure 3.8: Contours of static temperature (°C) of the HCFP divertor test section displaying nearly uniform incident heat flux in the neck of the copper heater.

The temperatures and convective heat transfer coefficient (HTC) on the cooled surface above the impinging jets are of primary interest for this investigation. As expected, the HTC is highest at the stagnation point right above each jet. The peak HTC in this case was found to be 2.82 kW/m^2-K, which corresponds to a helium heat transfer coefficient, for the same Reynolds number and geometry, of 34.1 kW/m^2-K, which is consistent with the predicted peak HTC of ~39 kW/m^2-K, for the 0.5 mm prototypical HCFP (Wang, 2008). The average HTC, however, is only 1.25 kW/m^2-K for air, corresponding to an average helium HTC of 15.1 kW/m^2-K. These conversions are based on the fact that $\boldsymbol{Nu}_{\mathbf{air}} = \boldsymbol{Nu}_{\mathbf{He}}$ for the same Reynolds number and geometry. The conductivity of air and helium are calculated using Engineering Equation Solver (EES)

v8.185; $\boldsymbol{k_{air}}$ = 0.02753 W/m-k (P_{sys} = 414 kPa, T_{sys} = 51°C) and $\boldsymbol{k_{He}}$ = 0.3326 W/m-K (P_{sys} = 10 MPa, T_{sys} = 600°C). Since,

$$Nu = \frac{D_h * h}{k}, \tag{3.1}$$

and D_h is the same in both cases, then

$$h_{He} = \frac{k_{He}}{k_{air}} * h_{air} = 12.1 * h_{air}\ . \tag{3.2}$$

Although the HTC changes radically with distance from jets (Figure 3.9), the temperature is fairly uniform across the test section (Figure 3.10), i.e., it is independent of the position of the jets. This uniformity occurs primarily because of conduction in the relatively high thermal conductivity brass. The temperature is lower at the ends of the cooled surface since the incident heat flux is only applied to the center 76.2 mm (3") corresponding to the length of the inlet manifold. However, the cooled surface (inner surface of the brass outer shell) is 88.2 mm long.

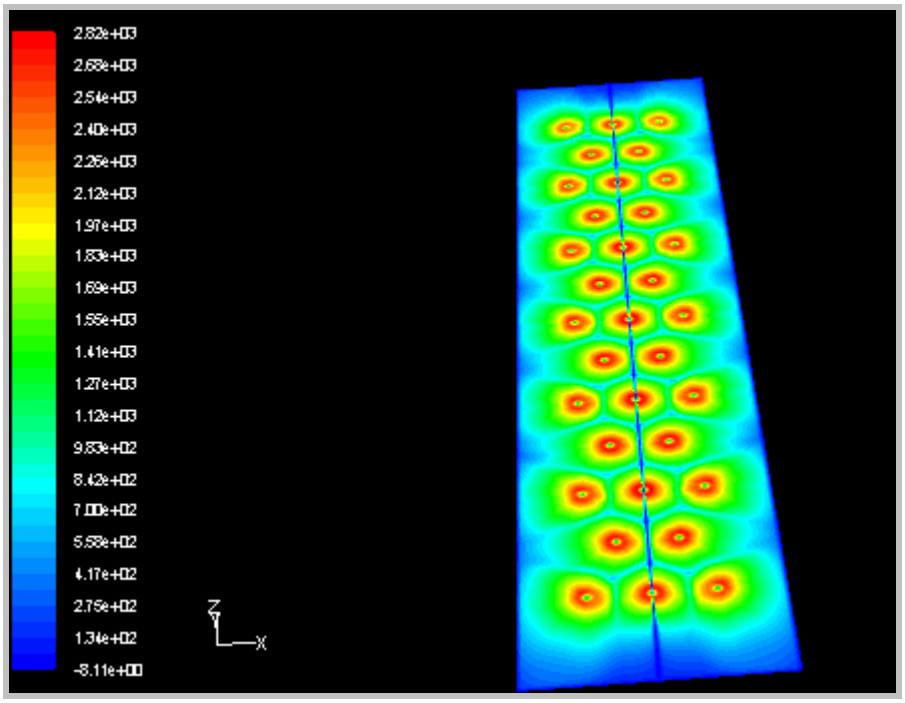

Figure 3.9: Convective heat transfer coefficient (W/m^2-K) contour plot of cooled surface for the array of holes test section - medium flow case.

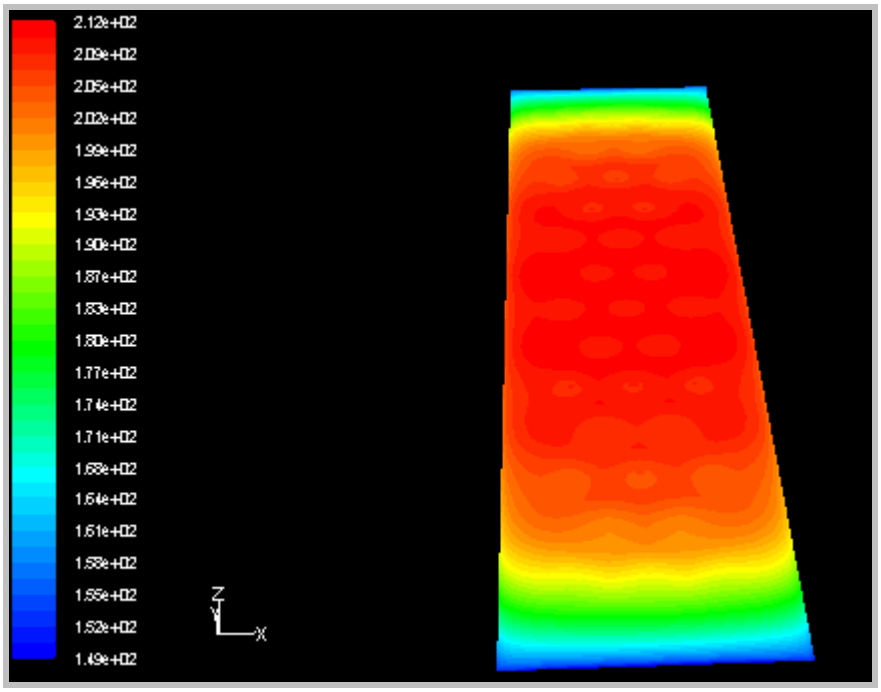

Figure 3.10: Static Temperature (°C) contour plot of cooled surface for the array of holes test section - medium flow case.

The pathlines of the coolant flow through the test module are shown in Figure 3.11. The pathlines are colored by velocity magnitude. As seen from the legend, the maximum speed reached in the jets is 177 m/s, which corresponds to a Mach number of ~0.5. Therefore it was considered important to include compressibility effects in the model. The surface shown (gray) is the aluminum inner cartridge. The image in the top left corner shows the pathlines impinging on the cooled surface and flowing down along the sides of the inner cartridge into the outlet manifold. Figure 3.12 gives a better idea of the velocity profile near the cooled surface by showing the velocity vectors, colored by magnitude. The velocity profile is very similar to the HTC profile shown in Figure 3.7, i.e. the regions of highest velocity are also the regions with the highest HTC.

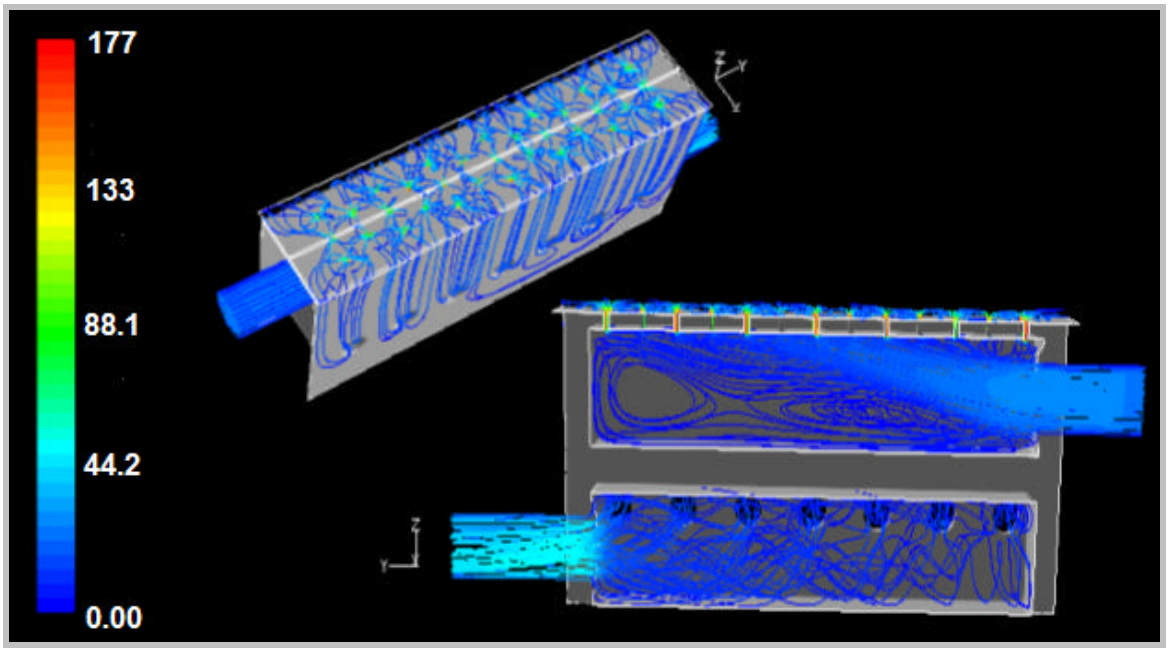

Figure 3.11: Coolant pathlines through the test module, colored by velocity magnitude (m/s).

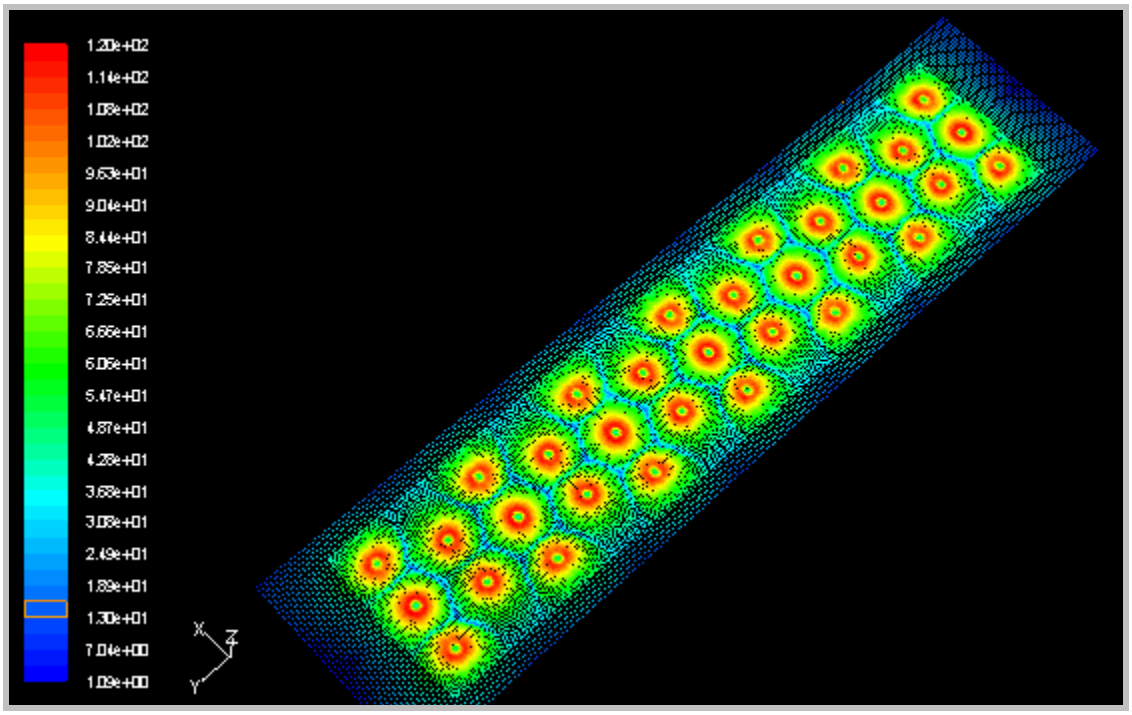

Figure 3.12: Velocity vector plot of cooled surface for the array of holes test section - medium flow case.

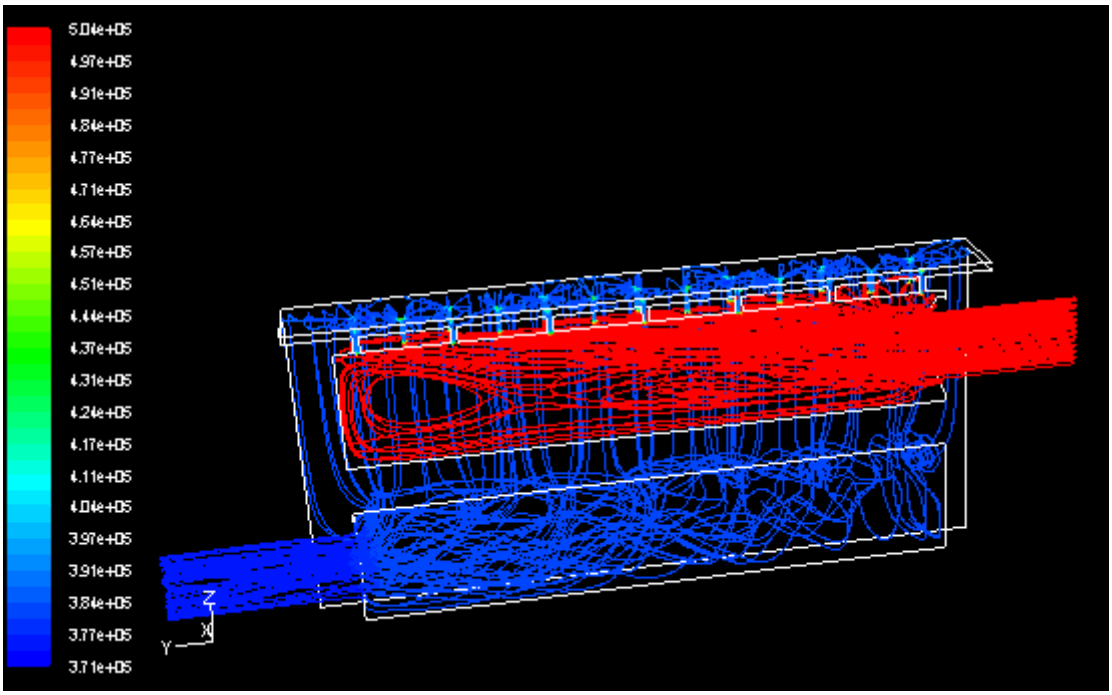

Figure 3.13: Coolant pathlines through the test module, colored by static pressure (Pa).

Figure 3.13 shows the coolant pathlines colored by static pressure. This figure is interesting because it indicates that ~all of the pressure drop occurs in the jets. There is also a region of adverse pressure (pressure increase in the flow direction) at the location where the impinging stream comes into contact with the wall. Figure 3.14 shows a close-up of one of the jets to emphasize this feature.

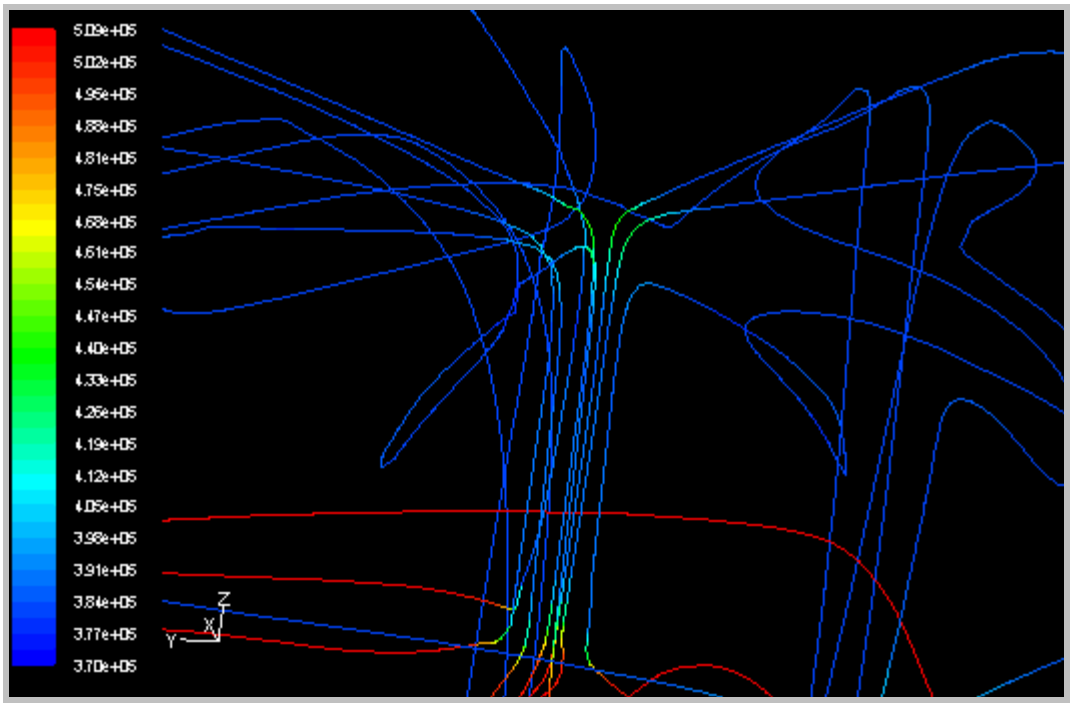

Figure 3.14: Close-up of coolant pathlines through a single jet, colored by static pressure (Pa)

CHAPTER IV

RESULTS AND DISCUSSION

In this chapter the experimental results obtained for the six test section configurations examined in this investigation are presented. In addition, the FLUENT numerical results obtained for the "*Holes*" test configuration are presented and compared to the corresponding experimental data. This chapter is organized as follows. Section 4.1 examines the effect of system pressure on the heat transfer coefficients for the same geometry and Reynolds numbers. Section 4.2 compares the experimental temperature profiles obtained for the "*Slot"* and "*Holes"* test section geometries. Sections 4.3 and 4.4 compare the data obtained for the test cases with and without a metal foam insert between the top of the inlet manifold and the cooled surface. Specifically, section 4.3 compares the experimental temperature profiles of the "*Holes"* and "*Holes-65" test configurations, while s*ection 4.4 compares the temperature profiles of the *"Slot", "Slot-45", "Slot-65"*, and *"Slot-100" test configurations.* Section 4.5 compares the temperature profiles and pressure drop values for all six configurations for a constant mass flow rate and incident heat flux. Finally, section 4.6 compares the experimental temperature profile, local heat transfer coefficients, and pressure drop for the *"Holes" test configuration against the corresponding numerical values obtained using FLUENT.*

4.1 Effect of System Pressure

In this section, experiments examining the effect of system pressure on the measured temperature distributions (i.e. the heat transfer coefficients) for the same test configuration, mass flow rate (i.e. Reynolds number), and incident heat flux are presented. Naturally, one would expect that for the same geometry and Reynolds number, the corresponding local Nusselt numbers (i.e. heat transfer coefficients) would be the same. However, concerns about the possibility of choking at high mass flow rates with low system pressure, coupled with the extent to which compressibility effects may impact the results and/or experimental procedures prompted this series of experiments. The **"***Holes"* test configuration was used in these experiments. Tests were performed at both high and low system pressures over the full range of Reynolds numbers and incident heat flux values. To facilitate comparison, the average HTC, h_{avg}, and the percentage change in HTC, $\% \Delta h_{avg}$, are calculated for each test using the following formulas:

$$h_{avg} = \left(\frac{q''_{nom}}{T_{avg} - T_{in}} \right) \tag{4.1}$$

$$\% \Delta h_{avg} = \frac{(h_{avg})_2 - (h_{avg})_1}{(h_{avg})_1} . \tag{4.2}$$

The results of these tests are shown in Table 4.1 and Figure 4.1. As expected, for the same mass flow rate (i.e. Reynolds number) and incident heat flux, system pressure did not significantly impact the average and local heat transfer coefficients; differences of only ~1% were observed over the examined range of pressures. This result indicates that, over the range of test conditions examined in this investigation, compressibility effects

are insignificant because of the relatively modest Mach number values. Choking, high Mach numbers, and compressibility effects limit the maximum possible flow rates and make CFD simulations more complicated.

Table 4.1: Holes experiments comparing the impact of P_{sys} on HTC

Case #	$\dot{m}$ (g/s)	q''_{nom} (MW/m^2)	P_{sys} (kPa)	ΔP (kPa)	T_{out} (°C)	h_{avg} (W/m^2-K)	% Δh_{avg} (-)
Holes-1	4.6	0.22	115.9	4.3	191.9	1304	--
Holes-2	4.6	0.22	266.5	4.1	194.0	1302	1%
Holes-4	13.2	0.49	188.3	32.1	214.0	2548	--
Holes-5	13.3	0.49	491.3	33.6	214.7	2549	0%
Holes-8	21.3	0.62	270.0	71.7	202.8	3422	--
Holes-9	21.3	0.62	430.7	75.5	204.8	3400	1%

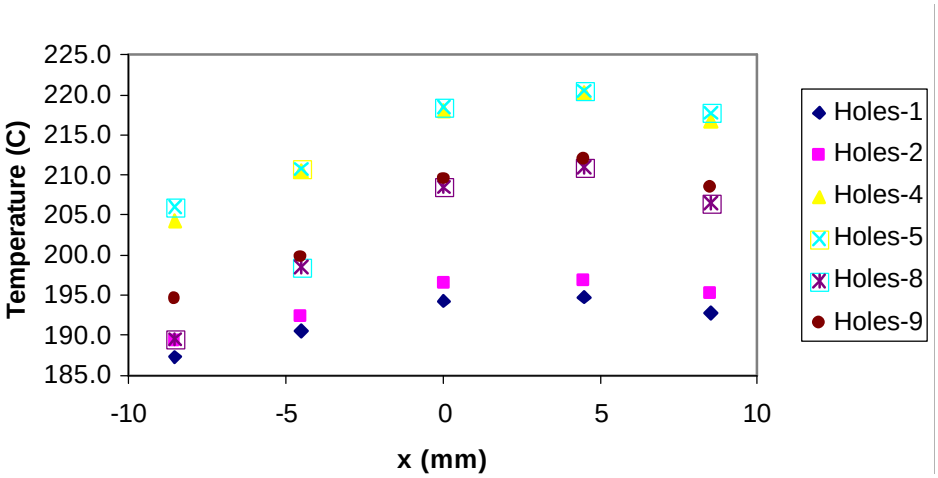

Figure 4.1: *Holes* experiments showing the effect of system pressure on HTC

4.2 Comparison between the *"Slot"* and *"Holes"* Test Configurations

It is of interest to compare the heat transfer performance of two of the leading jet-impingement geometries for helium-cooled divertors, namely, planar jets (i.e. slots) and

circular jets (i.e. holes). It is arguable as to whether such comparison should be made at the same Reynolds number or the mass flow rate; both comparisons have been made. The results are displayed in Table 4.2 and Figures 4.2 and 4.3. If the mass flow rate $\dot{m}$ is kept constant for both test section configurations, the holes configuration gives lower cooled surface temperatures, and hence, a higher average HTC. This is to be expected since the Reynolds number is much higher for the *Holes* experiments than the *Slot* for a given $\dot{m}$. This is due to the fact that the total flow area of the holes is considerably smaller than the slot flow area, so that the *Holes* experiments have much higher impingement velocities and increased turbulent mixing compared to the *Slot* cases. However, this enhancement comes at a cost, namely a significant increase in pressure drop as can be seen in Table 4.2, where the normalized pressure drop **?P'** values for the *"Holes"* test configuration are significantly higher than the corresponding values for the *"Slot"* test configuration. for the constant $\dot{m}$ experiments. If, on the other hand, the Reynolds number is kept constant, the trend is reversed.

One can argue that using $\dot{m}$ as the comparison basis is the most appropriate, inasmuch as the inlet and exit temperatures of the divertor coolant are generally maintained within a specified range, so that for a given divertor heat load, the total required coolant flow rate, and hence the flow rate per unit area, would be fixed. As long as the peak temperatures and stresses can be maintained within the allowable limits, the main metric for comparison between designs would be the required pumping power, i.e. the pressure drop. It should be noted that the value of the Reynolds number depends on how the characteristic dimension is defined. This is particularly the case for divertor configurations with metallic foam inserts, where the hydraulic diameter could be defined

in any number of ways. This means that if different configurations were to be compared at the same Reynolds numbers, the mass flow rates, and hence the coolant exit temperatures, would be significantly different, if the incident heat load is to remain unchanged. Nevertheless, regardless of how the comparison between the test configurations is to be made, the data shown in Table 4.2 and figures 4.2 and 4.3 show a clear trade-off between enhanced heat transfer and increased pressure drop. Hereafter, comparison will only be made on the basis of constant $\dot{m}$. However, all experimental results will be reported in the appendix.

Table 4.2: Experiments comparing the array of holes to the slot impingement geometry.

Case #	$\dot{m}$ (g/s)	Re (-)	q''_{nom} (MW/m^2)	ΔP (kPa)	% ΔP (-)	h_{avg} (W/m^2-K)	% Δh_{avg} (-)	T_{out} (°C)
Constant $\dot{m}$								
Slot-1	9.0	1.3E+04	0.22	6.3	-	1682	-	59.9
Holes-3	9.2	2.4E+04	0.22	18.2	190%	2080	24%	60.9
Slot-2	25.7	3.6E+04	0.49	50.2	-	2970	-	50.1
Holes-6	25.6	6.6E+04	0.49	98.4	96%	3964	33%	51.4
Constant Re								
Slot-1	9.0	1.3E+04	0.22	6.3	-	1682	-	59.9
Holes-2	4.6	1.2E+04	0.22	4.1	-36%	1302	-23%	94.1
Slot-2	25.7	3.6E+04	0.49	50.2	-	2970	-	50.1
Holes-5	13.3	3.5E+04	0.49	33.6	-33%	2549	-14%	79.2
Slot-3	38.0	5.3E+04	0.62	118.9	-	3825	-	43.3
Holes-9	21.3	5.5E+04	0.62	75.5	-37%	3400	-11%	66.2

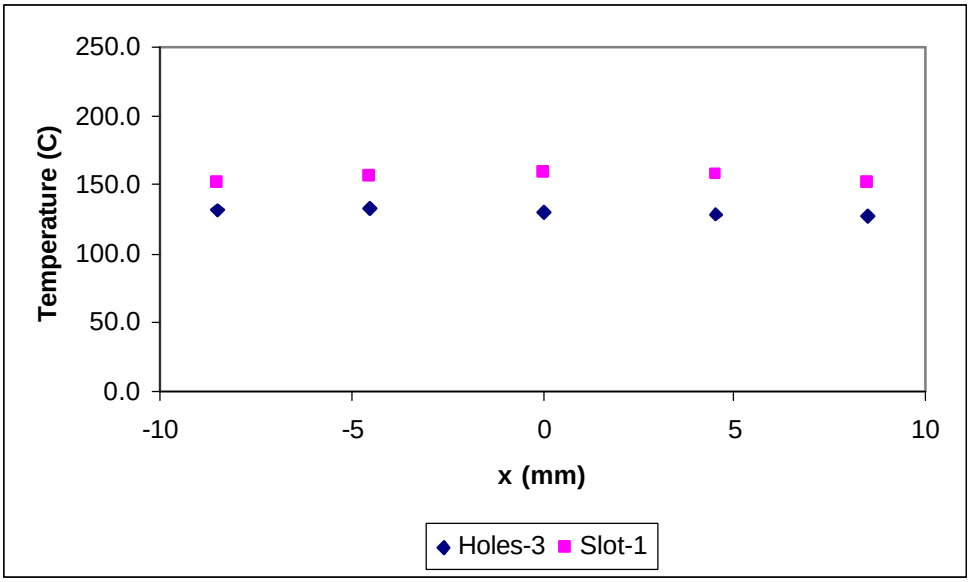

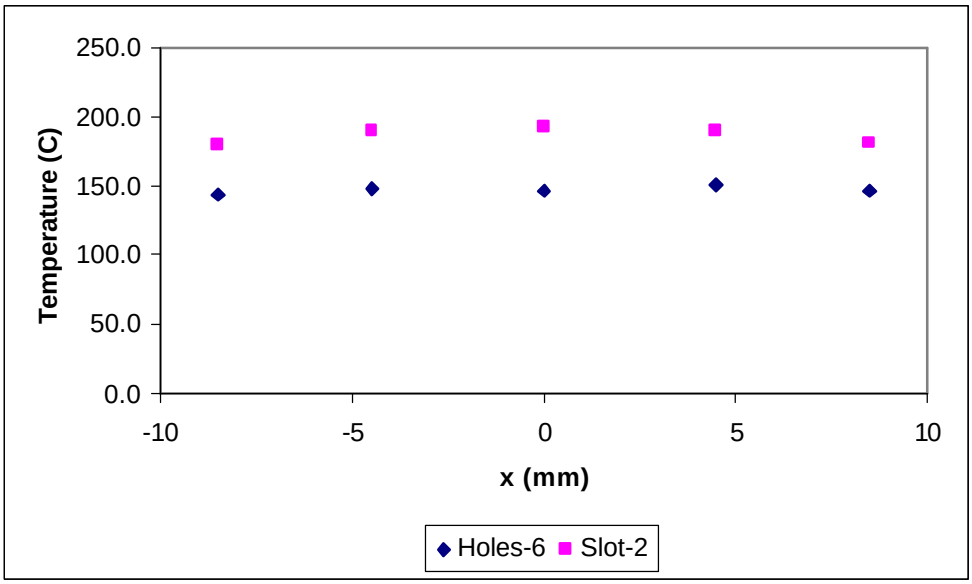

Figure 4.2: Holes vs. Slot temperature profiles for $\dot{m}$ = constant. Low Flow/Low Power (left), Med. Flow/Med. Power (right).

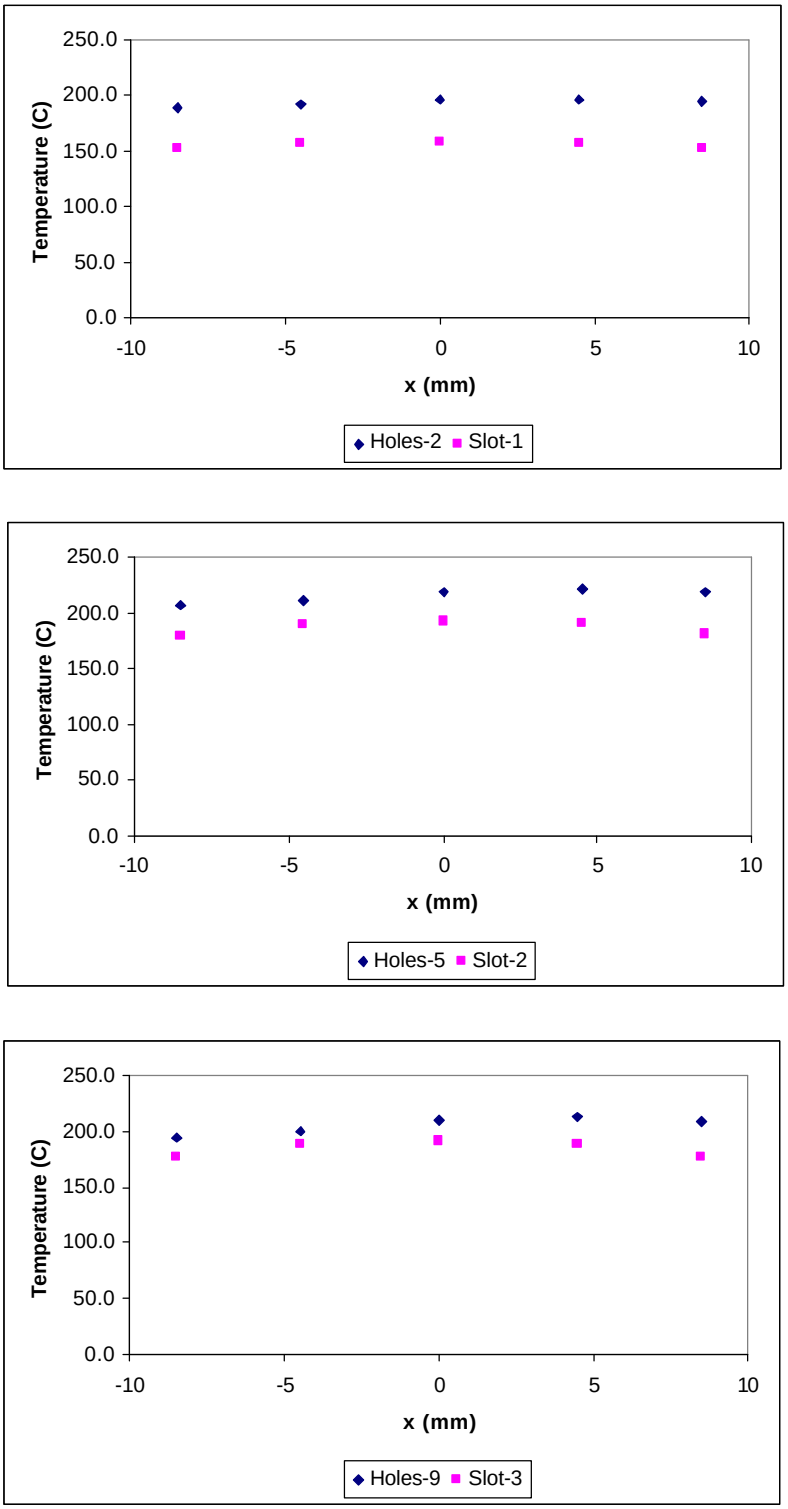

Figure 4.3: Holes vs. Slot temperature profiles for Re = constant. Low Flow/Low Power (top); Med. Flow/Med. Power (middle); High Flow/ High Power (bottom).

4.3 Effect of Metal Foam Insert for the *"Holes"* Test Configuration

The Holes jet geometry was tested with and without a 65 ppi Mo foam insert for a wide range of mass flow rates with two different heat flux values. This allows a direct comparison of the HTC enhancement and pressure drop increase that accompanies the use of metallic foam. The results of the experiments for these two configurations are presented in Table 4.3 and Figure 4.4. Since two different mass flow rates are tested at each power level, these experiments will also provide information on how the HTC changes with $\dot{m}$.

Table 4.3: Experiments comparing the array of holes with and without foam insert.

Case #	$\dot{m}$ (g/s)	q''_{nom} (MW/m^2)	ΔP (kPa)	$\%\Delta P$ (-)	T_{avg} (°C)	h_{avg} (W/m^2-K)	$\%\Delta h_{avg}$ (-)
Holes-2	4.6	0.22	4.1	-	194.0	1302	-
Holes-65-1	4.6	0.22	10.0	146%	154.7	1696	30%
Holes-3	9.2	0.22	18.2	-	129.9	2080	-
Holes-65-2	8.8	0.22	32.4	78%	117.3	2363	14%
Holes-5	13.3	0.49	33.6	-	214.7	2549	-
Holes-65-3	13.3	0.49	57.7	72%	185.9	3031	19%
Holes-7	26.2	0.49	101.1	-	143.6	4081	-
Holes-65-6	26.2	0.49	223.6	121%	135.9	4353	7%

The foam insert indeed increases the heat transfer performance of the divertor (by as much as 30% for the low flow case). However, the HTC enhancement provided by the foam appears to diminish as the mass flow rate (i.e. the jet Reynolds number) is increased; for the highest mass flow rate tested, the enhancement in the average heat transfer coefficient is only 7%. For the intermediate flow rate case (*Holes-3* and *Holes-65-2* experiments), an increase in the average HTC of 14% is observed with the foam despite a 4% reduction in the mass flow rate. This trend supports the predictions of

Sharafat (2007b) that increased turbulent mixing is the primary mode of HTC enhancement in the foam, rather than conduction or increased cooling area. Further evidence of this phenomenon is seen in the comparisons between how the HTC changes with mass flow rate between the two cases. A ~100% increase in flow (4.6 g/s vs. 9.2 (8.8) g/s and 13.3 g/s vs. 26.2 g/s) yields an average HTC increase of 60% for the no foam cases and 42% for the cases with foam.

It is observed from Table 5.2 that, as expected, the percent increase in pressure drop does not vary linearly with the mass flow rate. Therefore, there may be an optimal flow rate that minimizes the pressure increase associated with the foam. Still, the holes without foam appears to be a better choice, since it has a lower pressure drop, lower cost, and less uncertainty due to manufacturing tolerances, with only a slight reduction in HTC. It should be noted, however, that neither of the test configurations used in this investigation has been optimized. The data obtained here are only aimed at validating the CFD codes to be used to model the actual divertor modules. Once the CFD codes are validated, it will be possible to optimize the geometry and operating conditions for the different designs; comparison between the heat transfer performance and pressure drop values of such optimized designs at the actual operating conditions will ultimately be required to make the selection.

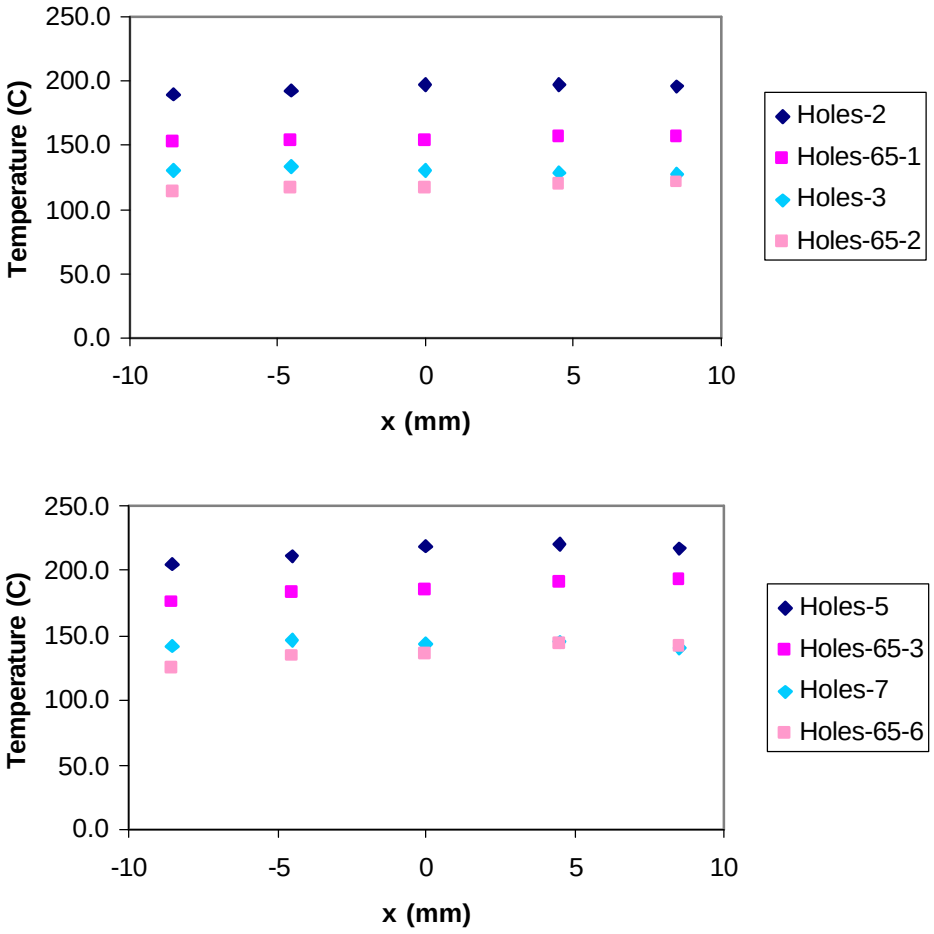

Figure 4.4: *Holes* vs. *Holes-65* temperature profiles for $\dot{m}$ = constant. Low Flow/Low Power (top), Med. Flow/Med. Power (bottom).

4.4 Effect of Metal Foam Insert for the *"Slot"* Test Configuration

In this section, the baseline design (*Slot*) is compared against three cases where Mo foam inserts characterized by various pore sizes and porosities were placed between the top of the inlet manifold and the cooled surface of the pressure boundary. This comparison will provide insight into the optimal foam design based on the HTC enhancement and pressure drop associated with each type of foam. The results are presented in Table 4.4 and Figures 4.5 and 4.6.

Table 4.4: Experiments comparing the slot to the various foam inserts.

Case #	$\dot{m}$ (g/s)	q''_{nom} (MW/m^2)	ΔP (kPa)	$\% \Delta P$ (-)	T_{avg} (°C)	h_{avg} (W/m^2-K)	$\% \Delta h_{avg}$ (-)
Slot-1	9.0	0.22	6.3	-	155.5	1682	-
Slot-45-1	9.0	0.22	13.0	107%	136.0	1945	16%
Slot-65-1	9.0	0.22	11.7	87%	109.7	2554	52%
Slot-100-1	9.0	0.22	14.8	136%	100.2	2875	71%
Slot-2	25.7	0.49	50.2	-	186.4	2970	-
Slot-45-3	26.0	0.49	99.2	98%	160.3	3573	20%
Slot-65-2	26.0	0.49	73.1	46%	139.0	4207	42%
Slot-100-2	26.2	0.49	106.2	112%	132.5	4476	51%
Slot-3	38.0	0.62	118.9	-	184.0	3825	-
Slot-65-3	40.1	0.62	180.4	52%	137.8	5378	41%

Although an increase in HTC is seen with all foam inserts compared to the baseline *"Slot"* geometry with the same flow rate and incident heat flux, there is a clear distinction in their performance that may make one more suitable than another. In general, one would expect an increase in heat transfer as the pore density is increased, since this will provide an increase in cooling surface area and turbulent mixing. This is validated by the data in Table 4.4. The 45 ppi foam performed the worst in terms of HTC enhancement. The percentage increase in the average heat transfer coefficient monotonically increases as the number of pores per inch increases. However, the change in pressure drop is not as straightforward. The poor pressure drop performance for the 45 ppi case would be contrary to the expected trend if the porosity was the same as the other two foam inserts. However, the porosity of the 45 ppi foam (70%) is much lower than that of the 65 ppi (88%) and 100 ppi (86%) foams. Consequently, it is difficult to directly compare the three foam test cases to determine whether the poor heat transfer performance for the 45 ppi case is due to the decreased pore density or the decreased

porosity, or even whether porosity improves or impairs heat transfer. Since the *Slot-65* and *Slot-100* cases are nearly equal in porosity, some evaluations can be made based on these two test geometries. Here again, it appears that the HTC enhancement compared to the baseline "*Slot*" case is most pronounced in the low flow experiments, where the velocities are lower, and hence, turbulent mixing is much lower without the foam. The 100 ppi foam performed the best in terms of heat transfer and the worst in terms of pressure drop. This reemphasizes the trade-off that exists between pressure drop and heat transfer. It would be of use to test foams with the same pore density and different porosities in the future to optimize this variable as well.

As noted earlier, none of the test configurations examined in this investigation has been optimized. The data obtained here are only aimed at validating the CFD codes to be used to model the actual divertor modules. Final selection of design parameters can only be made after the designs are optimized using the validated CFD code(s).

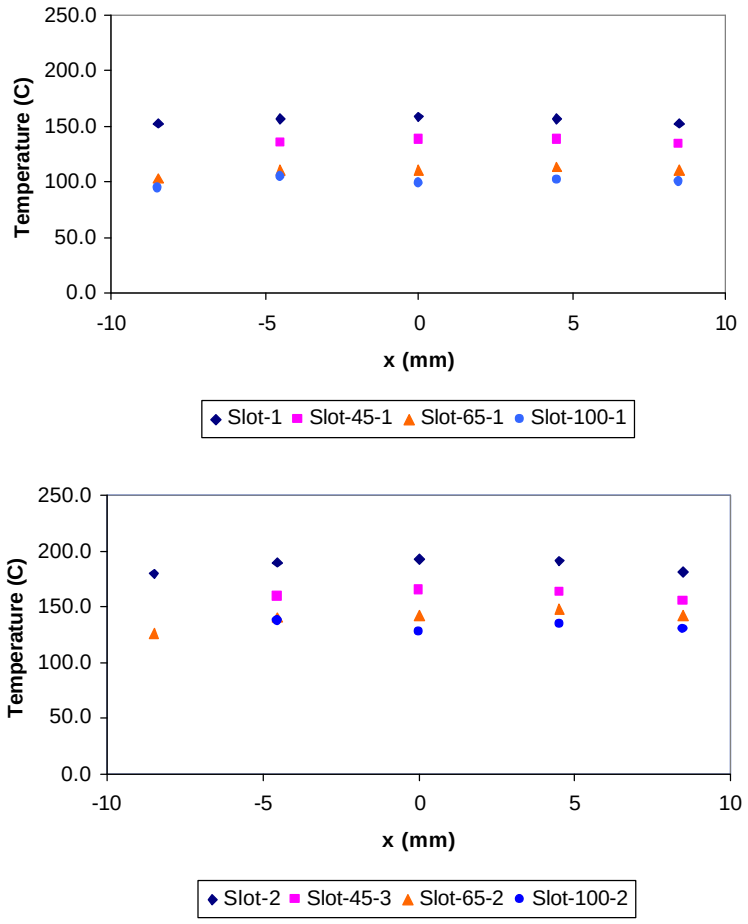

Figure 4.5: *Slot* vs. *Slot-45*, *Slot-65*, and *Slot-100* temperature profiles for $\dot{m}$ = constant. Low Flow/Low Power (top), Med. Flow/Med. Power (bottom).

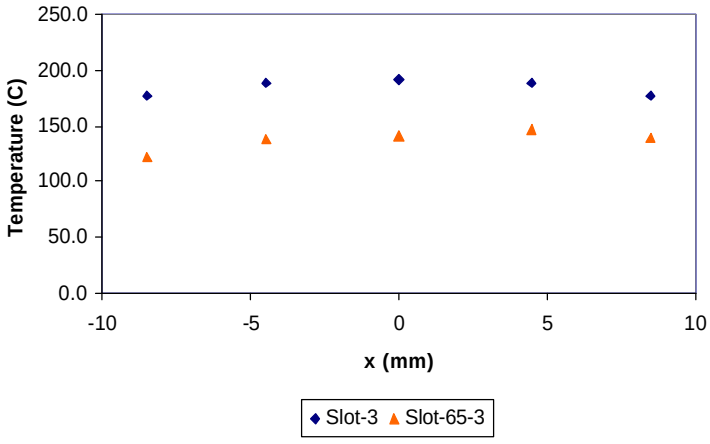

Figure 4.6: *Slot* vs. *Slot-65* temperature profiles for $\dot{m}$ = constant. High Flow/High Power.

It should be noted that in the *Slot-45-1*, *Slot-45-2*, and *Slot-100-2* experiments, TC#3 corresponding to x = -8.5 mm was broken, therefore no temperature information is known at this position for these three cases. Figure 4.6 compares only the *Slot-65* case to the *Slot*, since increased demand on the house air compressor would not allow these high flows to be reached when the *Slot-45* and *Slot-100* experiments were performed.

4.5 Comparison among All Test Configurations

Now that an in-depth look at the various experiments and parameters has been presented, this section provides a comparison among all six test section configurations at two mass flow rates and heat fluxes (Table 4.5). The pressure drop and average HTC are compared relative to the nominal design (*Slot*). Figure 4.7 shows the HTC plotted against mass flow rate for all experiments. Both Table 4.5 and the legend in Figure 4.7 are arranged according to the heat transfer performance, i.e the first entry, namely *Slot-100*, has the best heat transfer performance, while the last entry performs the worst.

Table 4.5: Summary of experiments comparing all six test modules.

Rank	Case #	ΔP (kPa)	% ΔP (-)	T_{avg} (°C)	h_{avg} (W/m^2-K)	% Δh_{avg} (-)
$\dot{m}$ =9 g/s, q''_{nom} =0.22 MW/m^2						
L 1	*Slot-100-1*	14.8	136%	100.2	2875	71%
L2	*Slot-65-1*	11.7	87%	109.7	2554	52%
L3	*Holes-65-2*	32.4	415%	117.3	2363	40%
L4	*Holes-3*	18.2	190%	129.9	2080	24%
L5	*Slot-45-1*	13.0	107%	136.0	1945	16%
L6	*Slot-1*	6.3	-	155.5	1682	-
$\dot{m}$ =26 g/s, q''_{nom} =0.49 MW/m^2						
H1	*Slot-100-2*	106.2	112%	132.5	4476	51%
H2	*Holes-65-6*	223.6	346%	135.9	4353	47%
H3	*Slot-65-2*	73.1	46%	139.0	4207	42%
H4	*Holes-7*	101.1	102%	143.6	4081	37%
H5	*Slot-45-3*	99.2	98%	160.3	3573	20%
H6	*Slot-2*	50.2	-	186.4	2970	-

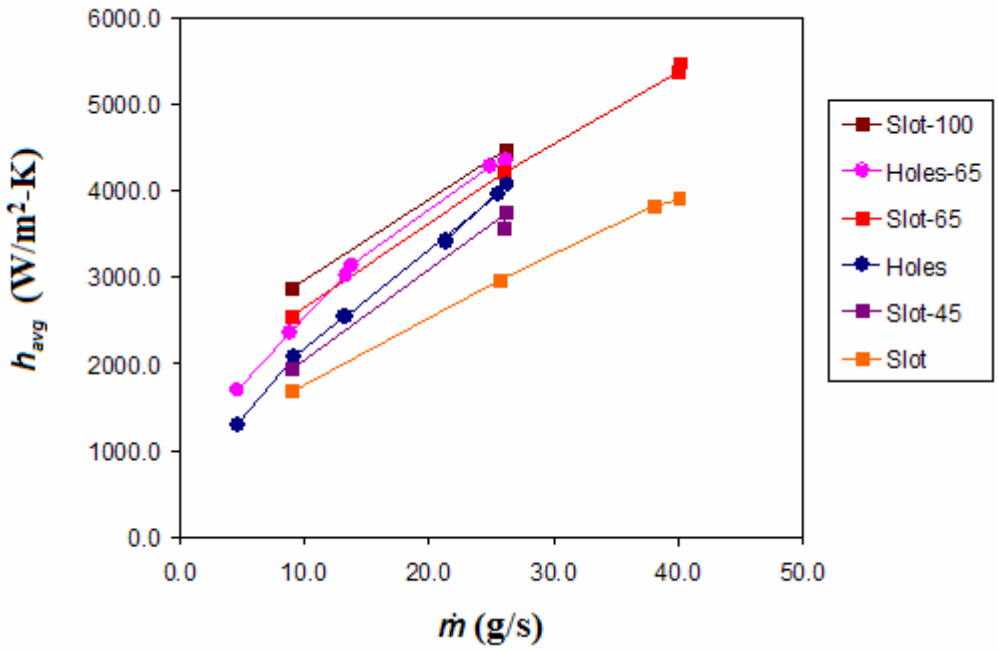

Figure 4.7: Comparison of average HTC versus mass flow rate for all test modules. The lines are linear interpolations between points.

The frontrunner in terms of highest average HTC for both flow rates is the *Slot-100*, characterized by a 2 mm wide slot and a 2 mm thick piece of 100 ppi Mb foam sandwiched between the top surface of the inner cartridge and outer shell. This result is not a "testament" to the cooling effectiveness of the slot design, but rather the 100 ppi foam, since a "*Holes-100*" test would almost certainly have produced an equally high HTC. However, the array of holes geometry was not tested with multiple foams based on the results of the *Holes-65* and *Slot-65* experiments. The *Slot-65* and *Holes-65* configurations produce the second-best performance in terms of heat transfer performance; however, the *Slot-65* has a pressure drop nearly 3 times lower than the *Holes-65* cases. Therefore, the Holes-with-foam design (in its present configuration) has been eliminated as a possible candidate unless design modifications, such as using larger holes, optimizing the hole pitch, or cutting matching holes in the foam are to be examined. The *Slot-65* configuration should be kept as a backup candidate in case the higher pressure drop associated with the 100 ppi foam is limiting. The 45 ppi foam (with 70% porosity) should also be eliminated from further consideration since it performs poorly in terms of both heat transfer and pressure drop.

The above experiments clearly show that HTC increases with pore density over the range studied (45-100 ppi). The foam significantly enhances heat transfer, particularly in the low flow cases. The *Slot-100* cases have a pressure drop comparable to *Holes* (no foam). The average HTC of the *Slot-100* Low Flow/Low Power case is nearly equal to that of the *Slot* High Flow/High Power case, with a pressure drop over 3 times lower. Therefore, the high pore density foam shows considerable potential for use in divertor design. However, the ultimate decision will be based on additional factors such as cost,

machining time and accuracy, durability, and robustness. In the event that foam is ruled out based on these considerations, the *Holes* design moves into first place with the highest HTC for a given $\dot{m}$. Still, the *Holes* design has a pressure drop considerably higher than the *Slot* design; recall that $A_{sl} \sim 10A_h$. In the end, it comes back to the trade-off between pressure drop and HTC and optimizing the design using a validated CFD model to best meet the needs of the application.

A graph showing the normalized pressure drops $\Delta P'$ plotted against mass flow rate $\dot{m}$ for all six test modules is shown in Figure 4.8. The parabolic curve-fits (lines) to the data for the rescaled pressure drops $\Delta P'$ (symbols) shown in Figure 4.8 all have R^2 values exceeding 0.999. Since $\Delta P' \propto \dot{m}^2$, this result provides added confidence in the accuracy of the measurements of $\dot{m}$ and ΔP for all experimental cases, as well as the normalization method used to calculate the $\Delta P'$ values. The pressure drops associated with all six test module configurations are shown in Figure 4.8. The legend lists the configurations in order of descending pressure drop, (i.e. *Holes-65* has the highest pressure drop and *Slot* has the lowest for a given $\dot{m}$). The *Holes*, *Slot-100*, and *Slot-45* have nearly equal pressure drops.

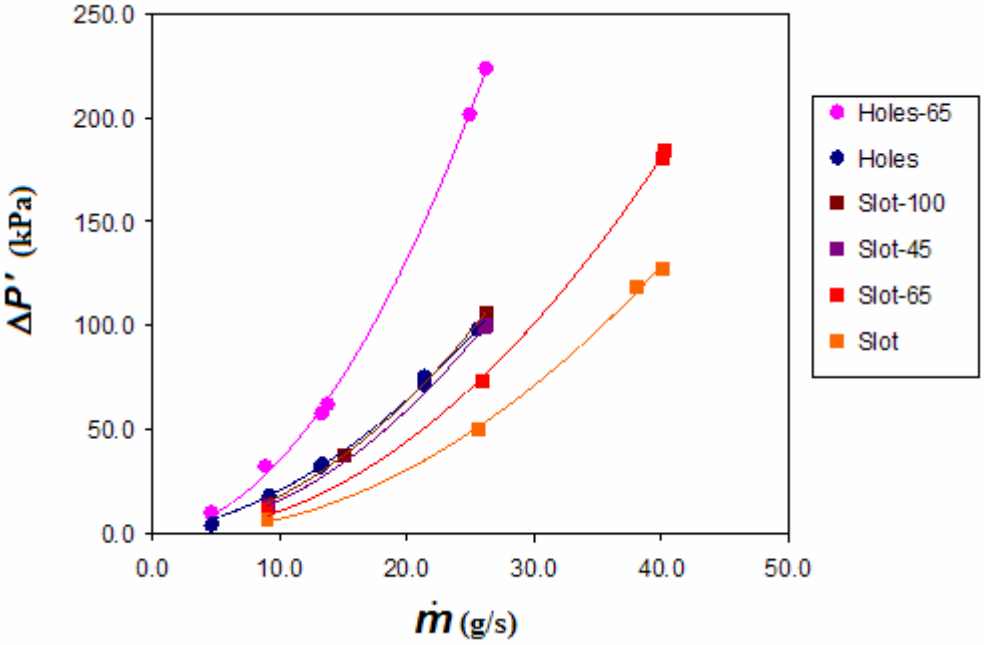

Figure 4.8: Comparison of pressure drop against mass flow rate for all test modules.

4.6 Numerical Results

This section presents the results obtained with the FLUENT numerical model described in Chapter 3. Because of the high level of effort required to generate an adequate mesh geometry, the numerical simulations have been limited to the *Holes* test module configuration. Three cases were run, namely, the Low Flow/ Low Power Medium Flow/ Medium Power and High Flow/ High Power experimental test cases, all of which correspond to high pressure conditions to eliminate the possibility of choking and reduce compressibility effects. The cases were run using various FLUENT modeling options to determine which would provide the best match to experimental data as well as test the variations between options. Unless otherwise specified, constant (default) air properties, ideal gas density, standard pressure discretization, and all other options described in Chapter 3 have been used. The experimental HTC is calculated using the

numerically predicted values of the local heat flux q''_{CFD}, since the local heat flux cannot be measured experimentally. Therefore the local HTC at a point on the cooled surface immediately below each TC, is defined as

$$h_{exp} = \frac{q''_{CFD}}{T_i - T_{in}} \tag{4.3}$$

where $\mathbf{T_i}$ is the temperature measured by the TC, i = 1,2,3,4,5, corrected to account for the conduction temperature drop between the thermocouple location and the surface. This temperature drop is taken to be equal to the FLUENT predicted temperature drop between the TC embedded location and the cooled surface, 1 mm below.

4.6.1 Low Flow/Low Power Test Condition

The Low Flow/Low Power case is representative of experimental case *Holes-2* and is characterized by $\dot{m}$ = 4.6 g/s and q''_{nom} = 0.22 MW/m^2. Additional experimental boundary conditions input into FLUENT are: $\mathbf{P_{in}}$ = 168.3 kPa (24.4 psig), $\mathbf{P_{out}}$ = 162.0 kPa (23.5 psig), $\mathbf{T_{in}}$ = 23.48 °C, $\mathbf{T_{out}}$= 94.07 °C, and Turbulence Intensity = 4.4%. The following options were investigated in FLUENT.

1. Standard k-e, standard wall functions, no viscous heating – SS0
2. Standard k-e, standard wall functions, w/ viscous heating – SSV
3. Standard k-e, non-equilibrium wall functions, w/ viscous heating – SNV
4. Standard k-e, non-equilibrium wall functions, w/ viscous heating,
   -Lowered outlet pressure to match FLUENT predicted pressured drop – SNVP
5. RNG k-e, non-equilibrium wall functions, w/ viscous heating – RNV

6. Spalart-Allmaras, vorticity-Based Production, w/viscous heating - SAVV
7. Low Pressure, standard k-e, standard wall functions, no viscous heating – SS0L (corresponds to *Holes-1*)

The results of the Low Flow/Low Power numerical cases are presented in Table 4.6, beneath their comparable experimental cases. The temperatures measured by the TCs (experimental), along with the predicted temperatures at the TC locations (numerical) are listed in Table 4.6; values of $\mathbf{T_i}$ where "i" denotes the TC number as defined in subsection 2.1.2 are tabulated. The FLUENT predicted average and peak HTCs on the cooled surface are also shown in Table 4.6, and referred to as $\mathbf{h_{CFD\_avg}}$ and $\mathbf{h_{CFD\_max}}$, respectively.

Table 4.6: Low Flow/ Low Power CFD results

	T_{in} (°C)	T_{out} (°C)	P_{in} (kPa)	P_{out} (kPa)	T_1 (°C)	T_2 (°C)	T_3 (°C)	T_4 (°C)	T_5 (°C)	h_{CFD_avg} (W/m^{2}K)	h_{CFD_max} (W/m^{2}K)
Holes-2	23.5	94.1	168.3	162.0	192.2	196.5	189.2	195.2	196.8	-	-
SS0	33.3	100.6	192.2	162.0	165.9	165.8	165.8	166.2	166.2	681	2621
SSV	33.4	100.6	191.6	162.0	166.0	166.0	166.0	166.4	166.4	680	2640
SNV	33.2	100.5	191.6	162.0	164.3	164.3	163.9	164.2	164.6	667	2482
SNVP	33.1	100.4	171.2	139.0	164.5	164.7	164.3	164.7	164.9	662	2460
RNV	33.4	100.5	189.8	162.0	167.2	167.6	166.5	166.8	167.4	629	1191
SAVV	34.2	101.4	190.3	162.0	184.8	185.2	184.1	184.4	185.1	528	1301
Holes-1	22.45	91.85	22.2	6.9	190.4	194.2	187.3	192.8	194.7	-	-
SS0L	31.7	96.7	74.2	6.9	164.4	164.3	164.3	164.7	164.7	672	2822

The options are tabulated in the order that they were tested. The original model "SS0" (and "SS0L" for the low pressure case) uses the same options utilized by Crosatti (2008) and Weathers (2007). This model uses the standard k-e turbulence model with standard wall function and no viscous heating - which is the default in FLUENT, since viscous heating is often negligible. This model did not adequately match the experimental conditions. The numerical temperature predictions in the TC locations were noticeably lower than the experimental values, resulting in a 16% over-prediction of the HTC. Additionally, the FLUENT predicted pressure drops are much higher than the experimental pressure drops.

Since the original model did not provide a good match to experimental data, as seen in Table 4.6, other options were investigated. The first variation (SSV) simply entailed enabling viscous heating, since, in compressible flows, viscous heating often becomes more important. However, the results of this model were nearly identical to the SSO case (16% over-estimation of the HTC), indicating that for the low flow case, viscous heating was indeed negligible. Next, the standard wall functions were replaced with non-equilibrium wall functions which are known to perform better in impinging flows (SNV). Once again, no improvements were seen; the results were nearly identical to the previous two cases (17% over-estimation of the HTC).

One particularly puzzling observation is that FLUENT changes the coolant inlet temperature $\mathbf{T_{in}}$, which is given as a boundary condition, by ~10°C. The reason FLUENT changes this boundary condition remains unresolved. One hypothesis was that since FLUENT was predicting an inlet pressure much higher than the experimental inlet pressure, FLUENT increased the temperature at the inlet such that the density at the inlet

remained the same as originally specified by the inlet temperature and pressure boundary conditions. This was the motivation behind case “SNVP”. In this case, the outlet pressure was artificially lowered to account for the increased pressure drop predicted by FLUENT so that the inlet pressure predicted by FLUENT would match the experimental inlet pressure. If the hypothesis were correct, FLUENT should also predict an inlet temperature similar to the experimental value. However, as seen from Table 4.6, this was not the case. Although the inlet pressure was considerably lower, the predicted inlet temperature remained the same. Once again, the HTC is over-predicted by nearly 16%.

Next it was decided to explore different turbulence models. The first variation on the standard turbulence was the RNG k-e model. The RNG model is similar to the standard k-e model, but is considered more accurate due to the following improvements: (1) an additional term in the e equation; (2) the inclusion of swirl effects on turbulence; (3) an analytical formula for turbulent Prandtl number; and (3) a differential formula for effective viscosity that accounts for low-Reynolds-number effects (FLUENT 12.4.2). Once again, however, the results are nearly identical to the previous cases, with nearly 15% over-estimation of HTC.

The next turbulence model selected was the Spalart-Allmaras model, which is a relatively simple one-equation closure. This model was designed specifically for wall-bounded flows with non-negligible compressibility and has been shown to give good results for boundary layers subjected to adverse pressure gradients, such as those seen in Figures 3.13 and 3.14. This model (SAVV) gave considerably different results than the k-e models. However, the predicted temperatures of the TCs are much closer to the experimental values, resulting in only a 5% over-estimation of the HTC. These results are

still questionable, however, since the issues with the inlet temperature and pressure boundary conditions modified by FLUENT have not been resolved. The Standard k-? (2-equation), Reynolds Stress (7-equation) and Large Eddy Simulation (LES) turbulence models were also attempted; however, the solution was divergent.

4.6.2 Medium Flow/Medium Power Test Condition

The Medium Flow/Medium Power case is representative of experimental case *Holes-5* and is characterized by $\dot{m}$ = 13.3 g/s and q''_{nom} = 0.49 MW/m^2. Additional experimental boundary conditions input into FLUENT are: $\mathbf{P_{in}}$ = 404.0 kPa (58.6 psig), $\mathbf{P_{out}}$ = 375.8 kPa (54.5 psig), $\mathbf{T_{in}}$ = 22.87 °C, $\mathbf{T_{out}}$= 79.18 °C, and Turbulence Intensity = 3.8%. The following options were explored in FLUENT.

1. Standard k-e, standard wall functions, no viscous heating – SSO
2. Standard k-e, non-equilibrium wall functions, w/ viscous heating – SNV
3. Spalart-Allmaras, Vorticity-Based Production, w/viscous heating – SAVV

The results of the Medium Flow/Medium Power numerical cases are presented in Table 4.7, below the corresponding experimental data for the *Holes-5* experiment. Fewer options are explored in this case, since some of the options were discarded if they did not produce a significant change in the Low Flow/ Low Power case or the High Flow/ High Power case. The low pressure case (*Holes-4*) would not converge in FLUENT due to choking and compressibility effects.

The numerical results for the Medium Flow/Medium Power cases follow the same trend as the Low Flow/Low Power cases. The standard k-e model with standard wall functions provides the worst match to experimental results, resulting in a 21% over-prediction of the HTC. The use of non-equilibrium wall functions gives some improvement, with a 18% over-prediction of the HTC. Spalart-Allmaras once again provides very different results from the k-e models, but matches the experimental results quite well. The difference between the experimental and numerical HTC, in this case, is only 1%. However, the predicted pressure drop is still much higher than the experimental value (Table 4.7).

Table 4.7: Medium Flow/ Medium Power CFD results

	T_{in} (°C)	T_{out} (°C)	P_{in} (kPa)	P_{out} (kPa)	T_1 (°C)	T_2 (°C)	T_3 (°C)	T_4 (°C)	T_5 (°C)	h_{CFD_avg} (W/m^{2}K)	h_{CFD_max} (W/m^{2}K)
Holes-5	22.9	79.2	404	375.8	210.8	218.6	206.0	217.8	220.5	-	-
SS0	29.8	80.9	503.3	375.8	173.2	172.2	174.3	175.3	173.9	1818	6885
SNV	29.9	81.1	502.1	375.8	179.3	178.5	179.5	180.4	179.7	1701	6263
SAVV	30.7	82.0	507.2	375.8	212.4	212.8	211.6	212.3	212.0	1249	2824

4.6.3 High Flow/High Power Test Condition

The High Flow/High Power case is representative of experimental case *Holes-9* and is characterized by $\dot{m}$ = 21.3 g/s and q''_{nom} = 0.62 MW/m^2. Additional experimental boundary conditions input into FLUENT are: P_{in} = 365.6 kPa (53.0 psig), P_{out} = 293.0

kPa **(**42.5 psig), $\mathbf{T_{in}}$ = 22.49 °C, $\mathbf{T_{out}}$= 66.25 °C, and Turbulence Intensity = 3.6%. The following options were explored in FLUENT.

1. Standard k-e, standard wall functions, no viscous heating – SSO
2. Standard k-e, standard wall functions, w/ viscous heating – SSV
3. Standard k-e, standard wall functions, w/ viscous heating, and 2^{nd} order Pressure dicretization – SSV2
4. Standard k-e, standard wall functions, w/ viscous heating, and Pressure Inlet - SSVP
5. Standard k-e, non-equilibrium wall functions, w/ viscous heating – SNV
6. Standard k-e, non-equilibrium wall functions, w/ viscous heating, and piece-wise linear air properties (EES – Table 4.8) – SNVL
7. Spalart-Allmaras, vorticity-Based Production, w/viscous heating – SAVV

The results of the High Flow/High Power numerical cases are presented in Table 4.7, below the corresponding experimental data for the *Holes-9* test. The low pressure case (*Holes-8*) would not converge in FLUENT due to choking and compressibility effects.

Table 4.8: High Flow/ High Power CFD results

	T_{in} (°C)	T_{out} (°C)	P_{in} (kPa)	P_{out} (kPa)	T_1 (°C)	T_2 (°C)	T_3 (°C)	T_4 (°C)	T_5 (°C)	h_{CFD_avg} (W/m^{2}K)	h_{CFD_max} (W/m^{2}K)
Holes-9	22.49	66.25	365.6	293	199.7	209.4	194.5	208.5	212.0	-	-
SS0	28.54	67.57	640.6	293	161.3	159.5	162.9	164.1	161.8	2726	10940
SSV	28.7	67.7	639.8	293	162.9	161.2	164.2	165.4	163.3	2683	11228
SSV2	28.5	67.6	641.5	293	161.5	159.6	163.0	164.2	162.0	2721	11232
SSVP	36.6	137.5	375.1	293	282.8	282.8	284.6	285.5	284.1	1166	5326
SNV	28.8	67.8	639.4	293	171.1	169.8	171.6	172.7	171.4	2458	9819
SNVL	28.7	67.8	639.8	293	168.0	166.8	168.5	169.6	168.4	2524	10003
SAVV	29.5	68.5	646.4	293	205.7	205.8	204.8	205.7	206.2	1784	4105

As shown in the Low Flow/ Low Power case, several modeling options have been examined in FLUENT in an attempt to match the experimental results. “SSO” is the baseline case with standard k-e model, standard wall functions and no viscous heating. This model over-predicts the HTC by nearly 24%. With viscous heating enabled (SSV), the temperatures on the cooled surface are slightly higher and the HTC is over-estimated by 23%. Next the pressure discretization is changed from “standard” to 2nd order (SSV2). The effects of this change were nearly negligible. The temperatures are nearly equal to the previous two cases and the HTC is over-predicted by 24%. Subsequently, the mass flow inlet was substituted with a pressure inlet boundary condition (SSVP). In this boundary condition, no mass flow rate is given to FLUENT, only the experimental inlet and exit pressures. FLUENT then calculates a mass flow rate based on these values. The resulting mass flow rate was 8.32 g/s compared to the experimental value of 21.3 g/s.

This resulted in temperature measurements much higher than experimental and an under-prediction of the HTC by 44%. Additionally, the inlet temperature is off by 14°C in this case, compared to 6°C in the previous cases. Clearly, this manner of setting the boundary conditions in FLUENT is inappropriate since errors in predicting the pressure drop are translated into errors in the mass flow rate, which lead to significant errors in the fluid temperatures and heat transfer coefficients.

Next, the non-equilibrium wall functions were used in place of the standard wall functions (SNV). As stated previously, FLUENT recommends their use for impinging flows. Indeed they do offer a noticeable improvement in matching the experimental temperatures. The HTC in this case is over-estimated by 19%. Subsequently, the default constant air properties were replaced with piecewise-linear functions using the data in Table 4.9 obtained from EES. While, this did have a small impact on the solution (~1%), it was not in the desired direction. Since the conductivity of air increases with temperature, the HTC increased as well, giving a HTC over-estimation of 20%.

Table 4.9: Air properties used for linear piece-wise function in SNVL case (EES).

T (°C)	**c_p** (J/kg-K)	**k** (W/m-K)	**μ** (kg/m-s)
293	1004	0.02514	1.83E-05
313	1005	0.02662	1.92E-05
333	1007	0.02808	2.01E-05
353	1008	0.02953	2.10E-05
373	1010	0.03095	2.18E-05
393	1012	0.03235	2.26E-05
413	1015	0.03374	2.35E-05
433	1018	0.03511	2.42E-05
473	1024	0.03779	2.58E-05
523	1034	0.04104	2.76E-05
573	1045	0.04418	2.93E-05
623	1056	0.04721	3.10E-05

Finally, the Spalart-Allmaras model is applied to the High Flow/ High Power case, after finding excellent comparisons in the Low Flow/Low Power and Medium Flow/ Medium Power cases. Again, the predicted temperatures and HTC are in excellent agreement with experimental results. The predicted HTC is only 1% different than the experimental HTC.

CHAPTER V

CONCLUSIONS AND RECOMMENDATIONS

5.1 Conclusions

The thermal performance of a prototypical flat plate divertor module was experimentally examined. The test module was designed and constructed to match the geometry, dimensions, material properties, and single-sided heating configuration of the actual flat plate divertor proposed by the ARIES team. Experiments were performed using air as the coolant with different values of the incident heat flux. The mass flow rate was selected to span the expected range of non-dimensional parameters for the actual helium-cooled flat plate divertor.

Six different variations of the flat-plate divertor concept were studied and evaluated in terms of their pressure drop and cooling performance. Wall temperature profiles, along with the local and average heat transfer coefficients, were measured for all test modules. Precise pressure drop measurements were made through the use of a differential pressure transducer connected in parallel across the test section. Additionally, approximate pressure drop values were determined from the two analog pressure gauges, at the exit of the rotameter and the exit of the test section.

The data obtained in this investigation follow the expected physical trends and provide a key dataset for validating commercially available CFD codes and models. These numerical codes can then be used to further optimize the dimensions of the impinging jet and the properties of the thermal interface material in the gap.

A 3-D numerical model duplicating the test module with the array of circular jets was created using the commercial CFD software package FLUENT. The numerical model was used in conjunction with the experimental boundary conditions to predict the wall temperature distributions, as well as the local heat transfer coefficients, and pressure drop. The heat transfer performance was shown to be slightly dependent on the choice of wall functions (standard vs. non-equilibrium) and highly dependent on the turbulence model (k-e vs. Spalart-Allmaras). In most cases, the difference between the experimental and numerical HTC was ~20%. The predicted pressure drop, on the other hand, was found to be virtually independent of the various viscous options (wall functions and turbulence models), but was a very poor match to experimental data (~700% difference).

5.1.1 Conclusions and Recommendations based on Experimental Results

This experimental investigation provides important results that extend and build upon previous studies of jet impingement cooling and porous medium heat exchangers. Heat transfer in jet impingement and porous media are complicated phenomena and general analytical solutions are not available. Typically, jet impingement studies are conducted experimentally and best-fit correlations are proposed (Beitelmal et al., 2006). The impingement of turbulent air jets on a flat surface with a small jet-to-wall spacing (H/D-holes or H/W-slot) was studied for the following jet geometries and porous media configurations:

- *Hexagonal Array of Circular Jets (Holes):* Circular jets of diameter D = 0.8 mm with a jet-to-wall spacing H/D = 1.25 on a staggered triangular array with a jet-to-jet

spacing s/D ~ 8 [corresponding to the "optimum pitch to diameter ratio" for multiple-jet impact cooling (San and Lai, 2001)] was tested with air for **Re** = 12,000 – 68,000.

- *Hexagonal Array of Circular Jets with 65 ppi Molybdenum Foam (Holes*-65): The same jet geometry as *(Holes)*, but with a 2.1 mm thick piece of 65 ppi molybdenum foam (88% porosity) compressed to 2.0 mm between the exit of the jets and the impingement surface, H/D = 2.5, was tested with air for **Re** = 11,000-68,000.
- *Rectangular Jet (Slot):* A rectangular jet with a width of 2 mm and a length of 76.2 mm with a jet-to-wall spacing H/W = 0.5 was tested with air over **Re** = 13,000 - 56,000.
- *Rectangular Jet with 45 ppi foam (Slot-45):* The same jet geometry as *(Holes)*, but with a 2.0 mm thick piece of 45 ppi molybdenum foam (70% porosity) compressed to 1.9 mm between the exit of the jets and the impingement surface, H/W = 0.95, was tested with air for **Re** = 13,000 and **Re** = 37,000.
- *Rectangular Jet with 65 ppi foam (Slot-65):* The same jet geometry as *(Holes)*, but with a 2.0 mm thick piece of 65 ppi molybdenum foam (88% porosity) compressed to 1.9 mm between the exit of the jets and the impingement surface, H/W = 0.95, was tested with air for **Re** = 13,000 - 56,000.
- *Rectangular Jet with 100 ppi foam (Slot-100):* The same jet geometry as *(Holes)*, but with a 2.0 mm thick piece of 100 ppi molybdenum foam (86% porosity) compressed to 1.9 mm between the exit of the jets and the impingement surface, H/W = 0.95, was tested with air for **Re** = 13,000 and **Re** = 37,000.

For test configurations with a porous metal foam insert, the Reynolds number, **Re,** is defined based on the impingement geometry, *Slot* or *Holes,* as indicated in Equation 2.1 and is *independent* of the characteristics of the foam. The characteristic dimensions used in the definition of the Reynolds number for the *Holes* and *Slot* geometries are the jet (i.e. hole) diameter and double the slot width, respectively.

The results of these studies show that for a given mass flow rate (or Reynolds number) the average heat transfer coefficient, $h_{avg,}$ *is highly dependent on the jet geometry*. For the specific geometries studied here, if $\dot{m}$ is held constant the *Holes* configuration has a higher average HTC. However, if **Re** is held constant the *Slot* configuration has a higher average HTC. This is primarily because the area of the slot is nearly an order of magnitude larger than the combined area of the holes. For a given **Re,** $\dot{m}$ is nearly 2 times higher in the *Slot* design.

An increase in heat transfer performance (compared to the baseline *Slot* design) was seen with all of the foam inserts. The data indicate that the HTC enhancement is dependent on the pore density or pores per inch (ppi). The *Slot-100* configuration (with the highest pore density) had the highest average HTC of all the designs, with a 71% improvement over the *Slot* design in the Low Flow/Low Power case and a 51% improvement in the Medium Flow/Medium Power case. The *Slot-65* and Holes-65 configurations were the runner-ups with a 52% and 40% improvement in the Low Flow/ Low Power case and a 47% and 42% improvement in the High Flow/High Power case over the *Slot* design. The reduction in relative improvement of HTC due to the metallic foam inserts with increasing mass flow rate (i.e. the jet Reynolds number) is a consistent trend throughout this study. This trend indicates that the HTC enhancement offered by

the foam is primarily due to increased turbulent mixing, rather than conduction or increased cooling area.

Comparing only the Holes and Holes-65 configurations at High Flow/High Power, reveals only a 7% average HTC increase with the 65 ppi foam insert, accompanied by a 121% increase in pressure drop. Therefore, if the *Holes* geometry as described above is used, it may not be advantageous to include a metallic foam as well. Clearly, it is not beneficial to accelerate the flows to extremely high speeds through the small area jets at the cost of significant pressure drop and then slow it down with the foam obstruction (increasing pressure drop further) before it ever hits the cooled surface.

This prompts the general *recommendation*: if metallic foam (or other porous media) is used, it should not be coupled with jet impingement, unless the foam is selectively located in the regions surrounding the jet impingement. By doing this, the pressure drop is reduced and the HTC profile becomes more uniform. Since in uninhibited jet impingement flows, the local HTC is greatly peaked near the jet stagnation point and falls off rapidly with lateral distance from the jet, porous media could greatly enhance the HTC in these regions. This can be accomplished through machining “jets” (slot or holes) in the foam matching the geometry of the jets machined into the inner cartridge. However, the high porosity/ high pore density foams are quite fragile and this would likely require advanced cutting techniques, such as lasers. The alternative approach would be to leave the foam intact, but greatly increase the area of the jets (slot or holes) to minimize the pressure drop and rely solely on the heat transfer enhancement of the foam, rather than jet impingement.

The latter approach is essentially the approach taken in the "slot with foam" studies presented here, although it is possible that an even wider slot width would be optimal. The slot width of 2 mm, gives an area ~10 times larger than the area of the Holes. As a result, the pressure drops in the *Slot-65* cases are ~3 times smaller than the comparable *Holes-65* cases, with a comparable heat transfer coefficient (only 3% reduction in the Medium Flow/ Medium Power case).

It is also noted that the pressure drop with the 100 ppi foam insert (*Slot-100*) is nearly double that of the case with no foam (*Slot*) for a given mass flow rate. However, the HTC enhancement through the foam is large enough, such that the *Slot-100* medium flow case has a 17% *higher average HTC* than the *Slot* high flow case with a 12% *lower pressure drop*. This is a significant benefit in favor of the metallic foam divertor concept – to improve heat transfer *and* reduce pressure drop. Therefore, it is recommended that the metallic foam divertor concept undergo further investigation and design optimization, i.e. higher pore density, higher porosity, slot in foam, and/or wider slot with no slot in the foam. It is also recommended to test the 0.5 mm slot geometry with no foam to more closely duplicate the jet impingement geometry of the original HCFP design.

5.1.2 Conclusions and Recommendations based on Numerical Results

The FLUENT model predictions for the array of holes geometry did not adequately match the experimental results. Several modeling options (turbulence model and wall functions) were investigated. Except for the Spalart-Allmaras turbulence model, the modeling options used had little impact on the overall result, suggesting that FLUENT predictions are generally insensitive to the options selected. Comparison

between the numerical predictions and the experimental data showed that FLUENT consistently *over-predicted* the HTC by ~20% for the range of Reynolds numbers tested. While a 20% uncertainty in the prediction of the heat transfer coefficient in complex geometries is "typical" for empirical Nusselt-type correlations, this result is somewhat disconcerting since it is consistently non-conservative and does not follow the trend of previous jet-impingement studies (Crosatti, 2008).

The Spalart-Allmaras turbulence model matched the experimental temperatures and local heat transfer coefficients remarkably well for all cases (< 6% difference in local HTC). However, this prompts the question: "Why the 20% difference between turbulence models and which one is correct?" Of course it is known which one is the better match to experimental data in these studies, but for future studies without experimental data, or for other divertor geometries, how will it be known? Additional work should be performed to further investigate the effect of modeling options on the numerical predictions, particularly for the other test configurations not modeled in this investigation. Furthermore, the pressure drop prediction did not agree with experimental data for all options and cases (400 - 1100 % error). Previous studies found the pressure drop to be off by ~25%, however the experimental pressure drop had a much larger error associated with it, since it came from the subtraction of an analog pressure gauge and a digital pressure transducer with ± 3 psi and ± 2.5 psi accuracy, respectively (Crosatti, 2008). Since the measured pressure drops in the HEMJ and T-tube test modules ranged from 1 to 20 psi, the experimental pressure drop measurement could have been off by as much as 450% in the low flow case, making the two studies approximately similar in accuracy. Regardless, this model as well as the validity of FLUENT for predicting complex, wall-

bounded, impingement flows with positive pressure gradients in the stagnation region requires further investigation. This should be the subject of future work.

It is also recommended that additional work should be performed to examine the effect of grid resolution on the predicted performance. The grid should be refined in the near-wall region to a value of $y^+ \sim 1$ to investigate its effect on HTC predictions. This was not possible for the current study, where grid resolution was limited by computer resources. However, enhancement of grid resolution, particularly in the near-wall region, can be accomplished (in the slot case) by using a 2-D model assuming the test section to be infinitely long in the axial direction. This method is far less computationally and time intensive. Various slot widths could be quickly compared; the effects of grid resolution, wall functions and turbulence models can also be examined. Since the actual divertor modules are expected to be fairly long (~2m), the results and conclusions to be derived from the two-dimensional numerical model should be applicable to the actual geometry. However, this is not possible for the case with hexagonal array of holes, since the jet geometry varies in the axial direction. It is also recommended that the FLUENT predictions and experimental data should be compared against predictions of other commercially available CFD codes, such as CFX and STAR-CD.

APPENDIX A

ERROR ANALYSIS

This appendix summarizes the uncertainties and sources of error associated with the experimental measurements of this investigation. The total uncertainty was calculated as the root-mean-square of the uncertainty due to statistical fluctuations, U_A, and the uncertainty of the instrumentation, U_B. An error propagation formula (A.3) was used to determine the uncertainty for derived quantities. The multiplier k_C of the sample standard deviation was determined by assuming a Gaussian distribution with 95% confidence intervals. The error propagation contribution to the total uncertainty did not include covariance terms.

$$U_A = k_c s_{Sample} \quad \textbf{A.1}$$

$$s_{Sample} = \sqrt{\frac{1}{N-1}\sum (x_i - \bar{x})^2} \quad \textbf{A.2}$$

$$U_X(i, j.., k) = \sqrt{U_i^2\left(\frac{\partial X}{\partial i}\right)^2 + U_j^2\left(\frac{\partial X}{\partial j}\right)^2 + ... + U_k^2\left(\frac{\partial X}{\partial k}\right)^2} \quad \textbf{A.3}$$

$$U_{Total} = \sqrt{U_A^2 + U_B^2} \qquad \textbf{A.4}$$

A.1 Uncertainty in Thermocouple Measurements

The total uncertainty in the thermocouple reading was derived from the manufacturer stated instrumental uncertainty, U_B = +/- 1.5 ^oC and the statistical fluctuations during an experiment. U_A was found by analyzing the temperature fluctuations during the experiment at steady state for 60 data points at nominal flow and power. This represents data collected for 5 minutes. A Gaussian distribution with k_C equal to 2.0 was used to encompass 95% of the measurements. The total uncertainty for each thermocouple is shown in Table A.2.

Table A.1: Thermocouple uncertainty data.

	Mean [^{o}C]	S_{Sample}	U_A	U_B	U_{total}
T1	210.8	0.383	0.765	1.50	1.68
T2	218.6	0.393	0.786	1.50	1.69
T3	206.0	0.374	0.748	1.50	1.68
T4	217.8	0.388	0.776	1.50	1.69
T5	220.5	0.395	0.790	1.50	1.70
T6	246.8	0.447	0.894	1.50	1.75
T7	253.3	0.460	0.920	1.50	1.76
T8	259.2	0.468	0.935	1.50	1.77
T9	247.8	0.449	0.897	1.50	1.75
T10	252.5	0.460	0.921	1.50	1.76
T11	258.3	0.467	0.934	1.50	1.77
T_{in}	22.9	0.016	0.031	1.50	1.50
T_{out}	79.2	0.136	0.272	1.50	1.52

A.2 Uncertainty in Mass Flow Rate

Only instrumental uncertainty U_B is considered in the mass flow rate measurement, since any statistical fluctuations were below the resolution of the instrumentation used and therefore undetectable. The mass flow rate calculation depended on three measured quantities: the "uncorrected" volume flow rate from the rotameter, the gauge pressure at the exit of the rotameter, and the temperature measured at the test section inlet. An analysis will be done based on the low flow case which will be subject to the largest error, since it is at lower pressure as well, (scfm = 5, Prot = 25 psig, Tin = 23.5°C). The rotameter has a minimum resolution of 0.25 standard cubic feet per minute (scfm). This corresponds to a relative mass flow rate uncertainty of 0.2 g/s. The pressure gauge had a minimum resolution of 1 psi with a typical accuracy of 3% full scale (FS) or 3 psi. This corresponds to a relative mass flow rate uncertainty of 0.2 g/s. The inlet temperature measurement has a total uncertainty of 1.5 as described in Section A.1, which corresponds to a relative mass flow rate uncertainty of 0.02 g/s and is therefore negligible. The maximum mass flow rate uncertainty is then approximately 6%.

A.3 Uncertainty in Pressure Drop

The uncertainty in the pressure drop was determined by considering statistical fluctuations in the differential pressure transducer reading as well as manufacturing uncertainties. The uncertainty for the statistical component U_A was found by analyzing the temperature fluctuations during the experiment at steady state for 60 data points at nominal flow and power for the *Slot* test module. This represents data collected for 5

minutes. A Gaussian distribution with k_C equal to 2.0 was used to encompass 95% of the measurements. This gave U_A = 0.078 psi. The Omega differential pressure transducer has a manufacturer stated tolerance of 0.1% FS or 0.3 psi. Therefore the total uncertainty is 0.3 psi for the nominal case, or 4%.

A.4 Uncertainty in Power Measurement

The uncertainty in the power input was determined by considering the statistical uncertainty due to fluctuations during the experiment and the manufacturer stated tolerances for the voltage and current measurement instruments. The statistical uncertainty was found, in the usual manner, to be U_A = 0.087 V or 0.94 W for the nominal power case (75.9 V, 10.8 A). The manufacturers' stated tolerance of the Agilent Data Acquisition unit is 0.01%, which is negligible. The resolution of the ammeter was 0.25 A, which corresponds to an uncertainty of 19 W. Therefore the total relative uncertainty in the power measurement is approximately 2.3%.

A.5 Uncertainty in Incident Heat Flux Measurement

The uncertainty in the measured incident heat flux is based on the uncertainty in the thermocouple temperatures (U_A ~ 1.75°C) and the uncertainty in the spacing between neighboring beads (0.1 mm). For a reasonable estimation, only the TC with the greatest spacing in the "neck" region of the copper concentrator is used, as shown in Equation A.5.

$$q''_{net} = k \frac{T_z - T_x}{D_{zx}} \tag{A.5}$$

The total uncertainty was calculated by determining the error propagation formula for the heat flux (Equation A.6), and the uncertainties of temperature measurements found in section A.1.

$$U_{q''_{net}} = \sqrt{\left(\frac{k}{\Delta x_{zx}}\right)^2 \left(U_{T_z}^2 + U_{T_x}^2\right) + U_{\Delta x_{zx}}^2 \left(\frac{q''}{\Delta x_{zx}}\right)^2} \qquad \text{(A.6)}$$

The uncertainty in the incident heat flux values vary greatly with the magnitude of the heat flux. For the slot design, with nominal flow and power, the relative uncertainty in the measured heat flux is 20% (46% at low power and 14% at high power). The rather high uncertainties at the low heat flux values are due to the high relative uncertainty (~3.5°C) in the measurement of the small temperature drop (~6°C) in the copper "neck".

A.6 Uncertainty in Heat Transfer Coefficient

The uncertainty in the heat transfer coefficient is mostly due to not knowing the local value of the heat flux except by FLUENT predictions. In general, FLUENT was ~20% different from experimental in the prediction of HTC, therefore it is reasonable to assume that the numerically predicted local heat flux is ~20% uncertain. The error propagation formula for the heat transfer coefficient is derived to be:

$$U_{HTC} = \sqrt{U_{q''}^2 \frac{1}{(T_w - T_{in})^2} + \left(U_{T_w}^2 + U_{T_{in}}^2\right) \frac{q''^2}{(T_w - T_{in})^4}}\,. \qquad \text{(A.7)}$$

The temperature standard uncertainties were computed in section A.1. The total uncertainty in the heat transfer coefficient is approximately 16%.

APPENDIX B

EXPERIMENTAL DATA AND CALCULATED QUANTITIES

Appendix B provides the measured and calculated data for each experiment performed in the investigation. The experiments are labeled consistently with the list of experiments provided in Section 2.2.

B.1 *Holes* Configuration

Table B.1: Experimental data for *Holes-1*

	Value	Units	Description
$\dot{m}$	4.6	[g/s]	Measured Mass Flow Rate
Re	1.2E+04	[-]	Jet Reynolds Number
$\mathbf{Q_{in}}$	369.5	[W]	Nominal Power Input
$\mathbf{Q_{out}}$	324.6	[W]	Power Out = $\dot{m}\ c_p(T_{out} - T_{in})$
% Losses	12%	[-]	Heat Loss
q''_{nom}	0.22	[MW/m^2]	Nominal Incident Heat Flux
q''_{net}	0.21	[MW/m^2]	Measured Incident Heat Flux
$\mathbf{P_{rot}}$	4.5	[psig]	Rotameter Pressure
$\mathbf{P_{out}}$	1	[psig]	Outlet Pressure
?P	2.2	[psi]	Measure Pressure Drop
$\mathbf{T_{in}}$	22.5	[^{o}C]	Inlet Temperature
$\mathbf{T_{out}}$	91.9	[^{o}C]	Outlet Temperature
$\mathbf{T_1}$	190.4	[^{o}C]	Embedded TC Ref. 1 in brass
$\mathbf{T_2}$	194.2	[^{o}C]	Embedded TC Ref. 2 in brass
$\mathbf{T_3}$	187.3	[^{o}C]	Embedded TC Ref. 3 in brass
$\mathbf{T_4}$	192.8	[^{o}C]	Embedded TC Ref. 4 in brass
$\mathbf{T_5}$	194.7	[^{o}C]	Embedded TC Ref. 5 in brass
$\mathbf{T_6}$	205.9	[^{o}C]	TC Ref. 6 in copper "neck"
$\mathbf{T_7}$	209.3	[^{o}C]	TC Ref. 7 in copper "neck"
$\mathbf{T_8}$	211.9	[^{o}C]	TC Ref. 8 in copper "neck"
$\mathbf{T_9}$	206.1	[^{o}C]	TC Ref. 9 in copper "neck"
$\mathbf{T_{10}}$	208.3	[^{o}C]	TC Ref. 10 in copper "neck"
$\mathbf{T_{11}}$	210.8	[^{o}C]	TC Ref. 11 in copper "neck"
$\mathbf{T_{peak\_1}}$	230.9	[^{o}C]	Peak Copper Temperature TC 1
$\mathbf{T_{peak\_2}}$	230.8	[^{o}C]	Peak Copper Temperature TC 2

Table B.2: Experimental data for *Holes-2*

	Value	Units	Description
$\dot{m}$	4.6	[g/s]	Measured Mass Flow Rate
Re	1.2E+04	[-]	Jet Reynolds Number
$\mathbf{Q_{in}}$	370.2	[W]	Nominal Power Input
$\mathbf{Q_{out}}$	328.5	[W]	Power Out = $\dot{m}\, c_p(T_{out} - T_{in})$
% Losses	11%	[-]	Heat Loss
q''_{nom}	0.22	[MW/m^2]	Nominal Incident Heat Flux
q''_{net}	0.21	[MW/m^2]	Measured Incident Heat Flux
$\mathbf{P_{rot}}$	25	[psig]	Rotameter Pressure
$\mathbf{P_{out}}$	23.5	[psig]	Outlet Pressure
?P	0.91	[psi]	Measure Pressure Drop
$\mathbf{T_{in}}$	23.5	[^{o}C]	Inlet Temperature
$\mathbf{T_{out}}$	94.1	[^{o}C]	Outlet Temperature
$\mathbf{T_1}$	192.2	[^{o}C]	Embedded TC Ref. 1 in brass
$\mathbf{T_2}$	196.5	[^{o}C]	Embedded TC Ref. 2 in brass
$\mathbf{T_3}$	189.2	[^{o}C]	Embedded TC Ref. 3 in brass
$\mathbf{T_4}$	195.6	[^{o}C]	Embedded TC Ref. 4 in brass
$\mathbf{T_5}$	196.8	[^{o}C]	Embedded TC Ref. 5 in brass
$\mathbf{T_6}$	208.0	[^{o}C]	TC Ref. 6 in copper "neck"
$\mathbf{T_7}$	211.4	[^{o}C]	TC Ref. 7 in copper "neck"
$\mathbf{T_8}$	214.0	[^{o}C]	TC Ref. 8 in copper "neck"
$\mathbf{T_9}$	208.5	[^{o}C]	TC Ref. 9 in copper "neck"
$\mathbf{T_{10}}$	210.6	[^{o}C]	TC Ref. 10 in copper "neck"
$\mathbf{T_{11}}$	213.2	[^{o}C]	TC Ref. 11 in copper "neck"
$\mathbf{T_{peak\_1}}$	233.3	[^{o}C]	Peak Copper Temperature TC 1
$\mathbf{T_{peak\_2}}$	233.0	[^{o}C]	Peak Copper Temperature TC 2

Table B.3: Experimental data for *Holes-3*

	Value	Units	Description
$\dot{m}$	9.2	[g/s]	Measured Mass Flow Rate
Re	2.4E+04	[-]	Jet Reynolds Number
$\mathbf{Q_{in}}$	370.2	[W]	Nominal Power Input
$\mathbf{Q_{out}}$	350.1	[W]	Power Out = $\dot{m}\, c_p(T_{out} - T_{in})$
% Losses	5%	[-]	Heat Loss
q''_{nom}	0.22	[MW/m^2]	Nominal Incident Heat Flux
q''_{net}	0.20	[MW/m^2]	Measured Incident Heat Flux
$\mathbf{P_{rot}}$	59.5	[psig]	Rotameter Pressure
$\mathbf{P_{out}}$	56	[psig]	Outlet Pressure
?P	2.21	[psi]	Measure Pressure Drop
$\mathbf{T_{in}}$	23.2	[^{o}C]	Inlet Temperature
$\mathbf{T_{out}}$	60.9	[^{o}C]	Outlet Temperature
$\mathbf{T_1}$	132.9	[^{o}C]	Embedded TC Ref. 1 in brass
$\mathbf{T_2}$	129.7	[^{o}C]	Embedded TC Ref. 2 in brass
$\mathbf{T_3}$	131.1	[^{o}C]	Embedded TC Ref. 3 in brass
$\mathbf{T_4}$	127.0	[^{o}C]	Embedded TC Ref. 4 in brass
$\mathbf{T_5}$	128.9	[^{o}C]	Embedded TC Ref. 5 in brass
$\mathbf{T_6}$	162.5	[^{o}C]	TC Ref. 6 in copper "neck"
$\mathbf{T_7}$	165.3	[^{o}C]	TC Ref. 7 in copper "neck"
$\mathbf{T_8}$	167.9	[^{o}C]	TC Ref. 8 in copper "neck"
$\mathbf{T_9}$	162.8	[^{o}C]	TC Ref. 9 in copper "neck"
$\mathbf{T_{10}}$	164.7	[^{o}C]	TC Ref. 10 in copper "neck"
$\mathbf{T_{11}}$	167.2	[^{o}C]	TC Ref. 11 in copper "neck"
$\mathbf{T_{peak\_1}}$	187.7	[^{o}C]	Peak Copper Temperature TC 1
$\mathbf{T_{peak\_2}}$	187.6	[^{o}C]	Peak Copper Temperature TC 2

Table B.4: Experimental data for *Holes-4*

	Value	Units	Description
$\dot{m}$	13.2	[g/s]	Measured Mass Flow Rate
Re	3.4E+04	[-]	Jet Reynolds Number
$\mathbf{Q_{in}}$	817.8	[W]	Nominal Power Input
$\mathbf{Q_{out}}$	686.7	[W]	Power Out = $\dot{m}\, c_p(T_{out} - T_{in})$
% Losses	16%	[-]	Heat Loss
q''_{nom}	0.49	[MW/m^2]	Nominal Incident Heat Flux
q''_{net}	0.45	[MW/m^2]	Measured Incident Heat Flux
$\mathbf{P_{rot}}$	21	[psig]	Rotameter Pressure
$\mathbf{P_{out}}$	7.5	[psig]	Outlet Pressure
?P	10.2	[psi]	Measured Pressure Drop
$\mathbf{T_{in}}$	21.6	[^{o}C]	Inlet Temperature
$\mathbf{T_{out}}$	73.3	[^{o}C]	Outlet Temperature
$\mathbf{T_1}$	210.5	[^{o}C]	Embedded TC Ref. 1 in brass
$\mathbf{T_2}$	218.1	[^{o}C]	Embedded TC Ref. 2 in brass
$\mathbf{T_3}$	204.2	[^{o}C]	Embedded TC Ref. 3 in brass
$\mathbf{T_4}$	216.9	[^{o}C]	Embedded TC Ref. 4 in brass
$\mathbf{T_5}$	220.2	[^{o}C]	Embedded TC Ref. 5 in brass
$\mathbf{T_6}$	246.0	[^{o}C]	TC Ref. 6 in copper "neck"
$\mathbf{T_7}$	252.4	[^{o}C]	TC Ref. 7 in copper "neck"
$\mathbf{T_8}$	258.2	[^{o}C]	TC Ref. 8 in copper "neck"
$\mathbf{T_9}$	246.3	[^{o}C]	TC Ref. 9 in copper "neck"
$\mathbf{T_{10}}$	251.0	[^{o}C]	TC Ref. 10 in copper "neck"
$\mathbf{T_{11}}$	256.8	[^{o}C]	TC Ref. 11 in copper "neck"
$\mathbf{T_{peak\_1}}$	299.9	[^{o}C]	Peak Copper Temperature TC 1
$\mathbf{T_{peak\_2}}$	299.5	[^{o}C]	Peak Copper Temperature TC 2

Table B.5: Experimental data for *Holes-5*

	Value	Units	Description
$\dot{m}$	13.3	[g/s]	Measured Mass Flow Rate
Re	3.5E+04	[-]	Jet Reynolds Number
$\mathbf{Q_{in}}$	816.0	[W]	Nominal Power Input
$\mathbf{Q_{out}}$	760.3	[W]	Power Out = $\dot{m}\, c_p(T_{out} - T_{in})$
% Losses	7%	[-]	Heat Loss
q''_{nom}	0.49	[MW/m^2]	Nominal Incident Heat Flux
q''_{net}	0.45	[MW/m^2]	Measured Incident Heat Flux
$\mathbf{P_{rot}}$	60	[psig]	Rotameter Pressure
$\mathbf{P_{out}}$	54.5	[psig]	Outlet Pressure
?P	4.1	[psi]	Measured Pressure Drop
$\mathbf{T_{in}}$	22.9	[^{o}C]	Inlet Temperature
$\mathbf{T_{out}}$	79.2	[^{o}C]	Outlet Temperature
$\mathbf{T_1}$	210.8	[^{o}C]	Embedded TC Ref. 1 in brass
$\mathbf{T_2}$	218.6	[^{o}C]	Embedded TC Ref. 2 in brass
$\mathbf{T_3}$	206.0	[^{o}C]	Embedded TC Ref. 3 in brass
$\mathbf{T_4}$	217.8	[^{o}C]	Embedded TC Ref. 4 in brass
$\mathbf{T_5}$	220.5	[^{o}C]	Embedded TC Ref. 5 in brass
$\mathbf{T_6}$	246.8	[^{o}C]	TC Ref. 6 in copper "neck"
$\mathbf{T_7}$	253.3	[^{o}C]	TC Ref. 7 in copper "neck"
$\mathbf{T_8}$	259.2	[^{o}C]	TC Ref. 8 in copper "neck"
$\mathbf{T_9}$	247.8	[^{o}C]	TC Ref. 9 in copper "neck"
$\mathbf{T_{10}}$	252.5	[^{o}C]	TC Ref. 10 in copper "neck"
$\mathbf{T_{11}}$	258.3	[^{o}C]	TC Ref. 11 in copper "neck"
$\mathbf{T_{peak\_1}}$	301.3	[^{o}C]	Peak Copper Temperature TC 1
$\mathbf{T_{peak\_2}}$	300.9	[^{o}C]	Peak Copper Temperature TC 2

Table B.6: Experimental data for *Holes-6*

	Value	Units	Description
$\dot{m}$	25.6	[g/s]	Measured Mass Flow Rate
Re	6.6E+04	[-]	Jet Reynolds Number
$\mathbf{Q_{in}}$	823.7	[W]	Nominal Power Input
$\mathbf{Q_{out}}$	741.8	[W]	Power Out = $\dot{m}\, c_p(T_{out} - T_{in})$
% Losses	10%	[-]	Heat Loss
q''_{nom}	0.49	[MW/m^2]	Nominal Incident Heat Flux
q''_{net}	0.42	[MW/m^2]	Measured Incident Heat Flux
$\mathbf{P_{rot}}$	67	[psig]	Rotameter Pressure
$\mathbf{P_{out}}$	51.5	[psig]	Outlet Pressure
?P	11.9	[psi]	Measured Pressure Drop
$\mathbf{T_{in}}$	22.8	[^{o}C]	Inlet Temperature
$\mathbf{T_{out}}$	51.4	[^{o}C]	Outlet Temperature
$\mathbf{T_1}$	148.6	[^{o}C]	Embedded TC Ref. 1 in brass
$\mathbf{T_2}$	146.1	[^{o}C]	Embedded TC Ref. 2 in brass
$\mathbf{T_3}$	144.0	[^{o}C]	Embedded TC Ref. 3 in brass
$\mathbf{T_4}$	146.4	[^{o}C]	Embedded TC Ref. 4 in brass
$\mathbf{T_5}$	150.6	[^{o}C]	Embedded TC Ref. 5 in brass
$\mathbf{T_6}$	207.4	[^{o}C]	TC Ref. 6 in copper "neck"
$\mathbf{T_7}$	213.4	[^{o}C]	TC Ref. 7 in copper "neck"
$\mathbf{T_8}$	219.2	[^{o}C]	TC Ref. 8 in copper "neck"
$\mathbf{T_9}$	209.2	[^{o}C]	TC Ref. 9 in copper "neck"
$\mathbf{T_{10}}$	213.3	[^{o}C]	TC Ref. 10 in copper "neck"
$\mathbf{T_{11}}$	218.8	[^{o}C]	TC Ref. 11 in copper "neck"
$\mathbf{T_{peak\_1}}$	260.9	[^{o}C]	Peak Copper Temperature TC 1
$\mathbf{T_{peak\_2}}$	260.8	[^{o}C]	Peak Copper Temperature TC 2

Table B.7: Experimental data for *Holes-7*

	Value	Units	Description
$\dot{m}$	26.2	[g/s]	Measured Mass Flow Rate
Re	6.8E+04	[-]	Jet Reynolds Number
$\mathbf{Q_{in}}$	823.5	[W]	Nominal Power Input
$\mathbf{Q_{out}}$	740.0	[W]	Power Out = $\dot{m}\, c_p(T_{out} - T_{in})$
% Losses	10%	[-]	Heat Loss
q''_{nom}	0.49	[MW/m^2]	Nominal Incident Heat Flux
q''_{net}	0.41	[MW/m^2]	Measured Incident Heat Flux
$\mathbf{P_{rot}}$	67	[psig]	Rotameter Pressure
$\mathbf{P_{out}}$	50.5	[psig]	Outlet Pressure
?P	12.3	[psi]	Measured Pressure Drop
$\mathbf{T_{in}}$	22.9	[^{o}C]	Inlet Temperature
$\mathbf{T_{out}}$	50.7	[^{o}C]	Outlet Temperature
$\mathbf{T_1}$	146.8	[^{o}C]	Embedded TC Ref. 1 in brass
$\mathbf{T_2}$	143.1	[^{o}C]	Embedded TC Ref. 2 in brass
$\mathbf{T_3}$	142.3	[^{o}C]	Embedded TC Ref. 3 in brass
$\mathbf{T_4}$	140.5	[^{o}C]	Embedded TC Ref. 4 in brass
$\mathbf{T_5}$	145.5	[^{o}C]	Embedded TC Ref. 5 in brass
$\mathbf{T_6}$	206.8	[^{o}C]	TC Ref. 6 in copper "neck"
$\mathbf{T_7}$	212.6	[^{o}C]	TC Ref. 7 in copper "neck"
$\mathbf{T_8}$	218.4	[^{o}C]	TC Ref. 8 in copper "neck"
$\mathbf{T_9}$	208.6	[^{o}C]	TC Ref. 9 in copper "neck"
$\mathbf{T_{10}}$	212.5	[^{o}C]	TC Ref. 10 in copper "neck"
$\mathbf{T_{11}}$	217.9	[^{o}C]	TC Ref. 11 in copper "neck"
$\mathbf{T_{peak\_1}}$	259.6	[^{o}C]	Peak Copper Temperature TC 1
$\mathbf{T_{peak\_2}}$	259.5	[^{o}C]	Peak Copper Temperature TC 2

Table B.8: Experimental data for *Holes-8*

	Value	Units	Description
$\dot{m}$	21.3	[g/s]	Measured Mass Flow Rate
Re	5.6E+04	[-]	Jet Reynolds Number
$\mathbf{Q_{in}}$	1034.4	[W]	Nominal Power Input
$\mathbf{Q_{out}}$	837.0	[W]	Power Out = $\dot{m}\, c_p(T_{out} - T_{in})$
% Losses	19%	[-]	Heat Loss
q''_{nom}	0.62	[MW/m^2]	Nominal Incident Heat Flux
q''_{net}	0.56	[MW/m^2]	Measured Incident Heat Flux
$\mathbf{P_{rot}}$	38	[psig]	Rotameter Pressure
$\mathbf{P_{out}}$	16.5	[psig]	Outlet Pressure
?P	15.9	[psi]	Measured Pressure Drop
$\mathbf{T_{in}}$	21.9	[^{o}C]	Inlet Temperature
$\mathbf{T_{out}}$	60.8	[^{o}C]	Outlet Temperature
$\mathbf{T_1}$	198.6	[^{o}C]	Embedded TC Ref. 1 in brass
$\mathbf{T_2}$	208.4	[^{o}C]	Embedded TC Ref. 2 in brass
$\mathbf{T_3}$	189.5	[^{o}C]	Embedded TC Ref. 3 in brass
$\mathbf{T_4}$	206.6	[^{o}C]	Embedded TC Ref. 4 in brass
$\mathbf{T_5}$	210.9	[^{o}C]	Embedded TC Ref. 5 in brass
$\mathbf{T_6}$	243.4	[^{o}C]	TC Ref. 6 in copper "neck"
$\mathbf{T_7}$	251.0	[^{o}C]	TC Ref. 7 in copper "neck"
$\mathbf{T_8}$	258.3	[^{o}C]	TC Ref. 8 in copper "neck"
$\mathbf{T_9}$	243.5	[^{o}C]	TC Ref. 9 in copper "neck"
$\mathbf{T_{10}}$	249.3	[^{o}C]	TC Ref. 10 in copper "neck"
$\mathbf{T_{11}}$	256.7	[^{o}C]	TC Ref. 11 in copper "neck"
$\mathbf{T_{peak\_1}}$	310.4	[^{o}C]	Peak Copper Temperature TC 1
$\mathbf{T_{peak\_2}}$	309.8	[^{o}C]	Peak Copper Temperature TC 2

Table B.9: Experimental data for *Holes-9*

	Value	Units	Description
$\dot{m}$	21.3	[g/s]	Measured Mass Flow Rate
Re	5.5E+04	[-]	Jet Reynolds Number
$\mathbf{Q_{in}}$	1034.7	[W]	Nominal Power Input
$\mathbf{Q_{out}}$	944.5	[W]	Power Out = $\dot{m}\, c_p(T_{out} - T_{in})$
% Losses	9%	[-]	Heat Loss
q''_{nom}	0.62	[MW/m^2]	Nominal Incident Heat Flux
q''_{net}	0.56	[MW/m^2]	Measured Incident Heat Flux
$\mathbf{P_{rot}}$	56	[psig]	Rotameter Pressure
$\mathbf{P_{out}}$	42.5	[psig]	Outlet Pressure
?P	10.5	[psi]	Measured Pressure Drop
$\mathbf{T_{in}}$	22.5	[^{o}C]	Inlet Temperature
$\mathbf{T_{out}}$	66.2	[^{o}C]	Outlet Temperature
$\mathbf{T_1}$	199.7	[^{o}C]	Embedded TC Ref. 1 in brass
$\mathbf{T_2}$	209.4	[^{o}C]	Embedded TC Ref. 2 in brass
$\mathbf{T_3}$	194.5	[^{o}C]	Embedded TC Ref. 3 in brass
$\mathbf{T_4}$	208.5	[^{o}C]	Embedded TC Ref. 4 in brass
$\mathbf{T_5}$	212.0	[^{o}C]	Embedded TC Ref. 5 in brass
$\mathbf{T_6}$	245.4	[^{o}C]	TC Ref. 6 in copper "neck"
$\mathbf{T_7}$	253.2	[^{o}C]	TC Ref. 7 in copper "neck"
$\mathbf{T_8}$	260.6	[^{o}C]	TC Ref. 8 in copper "neck"
$\mathbf{T_9}$	246.5	[^{o}C]	TC Ref. 9 in copper "neck"
$\mathbf{T_{10}}$	252.3	[^{o}C]	TC Ref. 10 in copper "neck"
$\mathbf{T_{11}}$	259.6	[^{o}C]	TC Ref. 11 in copper "neck"
$\mathbf{T_{peak\_1}}$	312.8	[^{o}C]	Peak Copper Temperature TC 1
$\mathbf{T_{peak\_2}}$	312.3	[^{o}C]	Peak Copper Temperature TC 2

B.2 *Holes-65* Configuration

Table B.10: Experimental data for *Holes-65-1*

	Value	Units	Description
$\dot{m}$	4.6	[g/s]	Measured Mass Flow Rate
Re	1.1E+04	[-]	Jet Reynolds Number
$\mathbf{Q_{in}}$	372.1	[W]	Nominal Power Input
$\mathbf{Q_{out}}$	332.1	[W]	Power Out = $\dot{m}\ c_p(T_{out} - T_{in})$
% Losses	11%	[-]	Heat Loss
q''_{nom}	0.22	[MW/m^2]	Nominal Incident Heat Flux
q''_{net}	0.24	[MW/m^2]	Measured Incident Heat Flux
$\mathbf{P_{rot}}$	25	[psig]	Rotameter Pressure
$\mathbf{P_{out}}$	22	[psig]	Outlet Pressure
?P	2.3	[psi]	Measured Pressure Drop
$\mathbf{T_{in}}$	23.2	[^{o}C]	Inlet Temperature
$\mathbf{T_{out}}$	94.7	[^{o}C]	Outlet Temperature
$\mathbf{T_1}$	154.1	[^{o}C]	Embedded TC Ref. 1 in brass
$\mathbf{T_2}$	154.3	[^{o}C]	Embedded TC Ref. 2 in brass
$\mathbf{T_3}$	151.5	[^{o}C]	Embedded TC Ref. 3 in brass
$\mathbf{T_4}$	157.4	[^{o}C]	Embedded TC Ref. 4 in brass
$\mathbf{T_5}$	156.1	[^{o}C]	Embedded TC Ref. 5 in brass
$\mathbf{T_6}$	171.4	[^{o}C]	TC Ref. 6 in copper "neck"
$\mathbf{T_7}$	175.0	[^{o}C]	TC Ref. 7 in copper "neck"
$\mathbf{T_8}$	178.1	[^{o}C]	TC Ref. 8 in copper "neck"
$\mathbf{T_9}$	173.3	[^{o}C]	TC Ref. 9 in copper "neck"
$\mathbf{T_{10}}$	175.6	[^{o}C]	TC Ref. 10 in copper "neck"
$\mathbf{T_{11}}$	178.4	[^{o}C]	TC Ref. 11 in copper "neck"
$\mathbf{T_{peak\_1}}$	198.7	[^{o}C]	Peak Copper Temperature TC 1
$\mathbf{T_{peak\_2}}$	198.7	[^{o}C]	Peak Copper Temperature TC 2

Table B.11: Experimental data for *Holes-65-2*

	Value	Units	Description
$\dot{m}$	8.8	[g/s]	Measured Mass Flow Rate
Re	2.2E+04	[-]	Jet Reynolds Number
$\mathbf{Q_{in}}$	373.1	[W]	Nominal Power Input
$\mathbf{Q_{out}}$	358.5	[W]	Power Out = $\dot{m}\, c_p(T_{out} - T_{in})$
% Losses	4%	[-]	Heat Loss
q''_{nom}	0.22	[MW/m^2]	Nominal Incident Heat Flux
q''_{net}	0.24	[MW/m^2]	Measured Incident Heat Flux
$\mathbf{P_{rot}}$	59.5	[psig]	Rotameter Pressure
$\mathbf{P_{out}}$	54.5	[psig]	Outlet Pressure
?P	4.0	[psi]	Measured Pressure Drop
$\mathbf{T_{in}}$	22.9	[^{o}C]	Inlet Temperature
$\mathbf{T_{out}}$	63.0	[^{o}C]	Outlet Temperature
$\mathbf{T_1}$	116.5	[^{o}C]	Embedded TC Ref. 1 in brass
$\mathbf{T_2}$	116.8	[^{o}C]	Embedded TC Ref. 2 in brass
$\mathbf{T_3}$	113.0	[^{o}C]	Embedded TC Ref. 3 in brass
$\mathbf{T_4}$	119.7	[^{o}C]	Embedded TC Ref. 4 in brass
$\mathbf{T_5}$	120.4	[^{o}C]	Embedded TC Ref. 5 in brass
$\mathbf{T_6}$	136.1	[^{o}C]	TC Ref. 6 in copper "neck"
$\mathbf{T_7}$	139.6	[^{o}C]	TC Ref. 7 in copper "neck"
$\mathbf{T_8}$	142.9	[^{o}C]	TC Ref. 8 in copper "neck"
$\mathbf{T_9}$	138.1	[^{o}C]	TC Ref. 9 in copper "neck"
$\mathbf{T_{10}}$	140.5	[^{o}C]	TC Ref. 10 in copper "neck"
$\mathbf{T_{11}}$	143.4	[^{o}C]	TC Ref. 11 in copper "neck"
$\mathbf{T_{peak\_1}}$	164.1	[^{o}C]	Peak Copper Temperature TC 1
$\mathbf{T_{peak\_2}}$	164.1	[^{o}C]	Peak Copper Temperature TC 2

Table B.12 Experimental data for *Holes-65-3*

	Value	Units	Description
$\dot{m}$	13.3	[g/s]	Measured Mass Flow Rate
Re	3.5E+04	[-]	Jet Reynolds Number
$\mathbf{Q_{in}}$	824.9	[W]	Nominal Power Input
$\mathbf{Q_{out}}$	785.0	[W]	Power Out = $\dot{m}\, c_p(T_{out} - T_{in})$
% Losses	5%	[-]	Heat Loss
q''_{nom}	0.49	[MW/m^2]	Nominal Incident Heat Flux
q''_{net}	0.48	[MW/m^2]	Measured Incident Heat Flux
$\mathbf{P_{rot}}$	61.0	[psig]	Rotameter Pressure
$\mathbf{P_{out}}$	52.0	[psig]	Outlet Pressure
?P	7.1	[psi]	Measured Pressure Drop
$\mathbf{T_{in}}$	22.9	[^{o}C]	Inlet Temperature
$\mathbf{T_{out}}$	81.3	[^{o}C]	Outlet Temperature
$\mathbf{T_1}$	183.7	[^{o}C]	Embedded TC Ref. 1 in brass
$\mathbf{T_2}$	184.8	[^{o}C]	Embedded TC Ref. 2 in brass
$\mathbf{T_3}$	176.1	[^{o}C]	Embedded TC Ref. 3 in brass
$\mathbf{T_4}$	193.0	[^{o}C]	Embedded TC Ref. 4 in brass
$\mathbf{T_5}$	191.7	[^{o}C]	Embedded TC Ref. 5 in brass
$\mathbf{T_6}$	223.2	[^{o}C]	TC Ref. 6 in copper "neck"
$\mathbf{T_7}$	229.9	[^{o}C]	TC Ref. 7 in copper "neck"
$\mathbf{T_8}$	236.7	[^{o}C]	TC Ref. 8 in copper "neck"
$\mathbf{T_9}$	227.2	[^{o}C]	TC Ref. 9 in copper "neck"
$\mathbf{T_{10}}$	232.3	[^{o}C]	TC Ref. 10 in copper "neck"
$\mathbf{T_{11}}$	238.1	[^{o}C]	TC Ref. 11 in copper "neck"
$\mathbf{T_{peak\_1}}$	280.1	[^{o}C]	Peak Copper Temperature TC 1
$\mathbf{T_{peak\_2}}$	280.1	[^{o}C]	Peak Copper Temperature TC 2

Table B.13 Experimental data for *Holes-65-4*

	Value	Units	Description
$\dot{m}$	13.7	[g/s]	Measured Mass Flow Rate
Re	3.6E+04	[-]	Jet Reynolds Number
$\mathbf{Q_{in}}$	816.2	[W]	Nominal Power Input
$\mathbf{Q_{out}}$	766.0	[W]	Power Out = $\dot{m}\, c_p(T_{out} - T_{in})$
% Losses	6%	[-]	Heat Loss
q''_{nom}	0.49	[MW/m^2]	Nominal Incident Heat Flux
q''_{net}	0.48	[MW/m^2]	Measured Incident Heat Flux
$\mathbf{P_{rot}}$	61.0	[psig]	Rotameter Pressure
$\mathbf{P_{out}}$	51.0	[psig]	Outlet Pressure
?P	7.8	[psi]	Measured Pressure Drop
$\mathbf{T_{in}}$	22.6	[^{o}C]	Inlet Temperature
$\mathbf{T_{out}}$	77.7	[^{o}C]	Outlet Temperature
$\mathbf{T_1}$	176.1	[^{o}C]	Embedded TC Ref. 1 in brass
$\mathbf{T_2}$	177.3	[^{o}C]	Embedded TC Ref. 2 in brass
$\mathbf{T_3}$	168.7	[^{o}C]	Embedded TC Ref. 3 in brass
$\mathbf{T_4}$	185.1	[^{o}C]	Embedded TC Ref. 4 in brass
$\mathbf{T_5}$	183.9	[^{o}C]	Embedded TC Ref. 5 in brass
$\mathbf{T_6}$	215.0	[^{o}C]	TC Ref. 6 in copper "neck"
$\mathbf{T_7}$	221.6	[^{o}C]	TC Ref. 7 in copper "neck"
$\mathbf{T_8}$	228.3	[^{o}C]	TC Ref. 8 in copper "neck"
$\mathbf{T_9}$	218.8	[^{o}C]	TC Ref. 9 in copper "neck"
$\mathbf{T_{10}}$	223.7	[^{o}C]	TC Ref. 10 in copper "neck"
$\mathbf{T_{11}}$	229.5	[^{o}C]	TC Ref. 11 in copper "neck"
$\mathbf{T_{peak\_1}}$	270.7	[^{o}C]	Peak Copper Temperature TC 1
$\mathbf{T_{peak\_2}}$	270.7	[^{o}C]	Peak Copper Temperature TC 2

Table B.14 Experimental data for *Holes-65-5*

	Value	Units	Description
$\dot{m}$	24.9	[g/s]	Measured Mass Flow Rate
Re	6.5E+04	[-]	Jet Reynolds Number
$\mathbf{Q_{in}}$	820.2	[W]	Nominal Power Input
$\mathbf{Q_{out}}$	686.2	[W]	Power Out = $\dot{m}\, c_p(T_{out} - T_{in})$
% Losses	16%	[-]	Heat Loss
q''_{nom}	0.49	[MW/m^2]	Nominal Incident Heat Flux
q''_{net}	0.49	[MW/m^2]	Measured Incident Heat Flux
$\mathbf{P_{rot}}$	61.0	[psig]	Rotameter Pressure
$\mathbf{P_{out}}$	19.0	[psig]	Outlet Pressure
?P	34.5	[psi]	Measured Pressure Drop
$\mathbf{T_{in}}$	23.0	[^{o}C]	Inlet Temperature
$\mathbf{T_{out}}$	50.3	[^{o}C]	Outlet Temperature
$\mathbf{T_1}$	135.5	[^{o}C]	Embedded TC Ref. 1 in brass
$\mathbf{T_2}$	137.7	[^{o}C]	Embedded TC Ref. 2 in brass
$\mathbf{T_3}$	126.4	[^{o}C]	Embedded TC Ref. 3 in brass
$\mathbf{T_4}$	144.0	[^{o}C]	Embedded TC Ref. 4 in brass
$\mathbf{T_5}$	144.9	[^{o}C]	Embedded TC Ref. 5 in brass
$\mathbf{T_6}$	178.9	[^{o}C]	TC Ref. 6 in copper "neck"
$\mathbf{T_7}$	185.5	[^{o}C]	TC Ref. 7 in copper "neck"
$\mathbf{T_8}$	192.5	[^{o}C]	TC Ref. 8 in copper "neck"
$\mathbf{T_9}$	182.4	[^{o}C]	TC Ref. 9 in copper "neck"
$\mathbf{T_{10}}$	187.5	[^{o}C]	TC Ref. 10 in copper "neck"
$\mathbf{T_{11}}$	193.6	[^{o}C]	TC Ref. 11 in copper "neck"
$\mathbf{T_{peak\_1}}$	235.8	[^{o}C]	Peak Copper Temperature TC 1
$\mathbf{T_{peak\_2}}$	235.7	[^{o}C]	Peak Copper Temperature TC 2

Table B.15 Experimental data for *Holes-65-6*

	Value	Units	Description
$\dot{m}$	26.2	[g/s]	Measured Mass Flow Rate
Re	6.8E+04	[-]	Jet Reynolds Number
$\mathbf{Q_{in}}$	819.8	[W]	Nominal Power Input
$\mathbf{Q_{out}}$	689.4	[W]	Power Out = $\dot{m}\, c_p(T_{out} - T_{in})$
% Losses	16%	[-]	Heat Loss
q''_{nom}	0.49	[MW/m^2]	Nominal Incident Heat Flux
q''_{net}	0.50	[MW/m^2]	Measured Incident Heat Flux
$\mathbf{P_{rot}}$	65.0	[psig]	Rotameter Pressure
$\mathbf{P_{out}}$	21.0	[psig]	Outlet Pressure
?P	36.2	[psi]	Measured Pressure Drop
$\mathbf{T_{in}}$	23.1	[^{o}C]	Inlet Temperature
$\mathbf{T_{out}}$	49.1	[^{o}C]	Outlet Temperature
$\mathbf{T_1}$	133.7	[^{o}C]	Embedded TC Ref. 1 in brass
$\mathbf{T_2}$	135.9	[^{o}C]	Embedded TC Ref. 2 in brass
$\mathbf{T_3}$	124.5	[^{o}C]	Embedded TC Ref. 3 in brass
$\mathbf{T_4}$	142.2	[^{o}C]	Embedded TC Ref. 4 in brass
$\mathbf{T_5}$	143.2	[^{o}C]	Embedded TC Ref. 5 in brass
$\mathbf{T_6}$	177.6	[^{o}C]	TC Ref. 6 in copper "neck"
$\mathbf{T_7}$	184.3	[^{o}C]	TC Ref. 7 in copper "neck"
$\mathbf{T_8}$	191.3	[^{o}C]	TC Ref. 8 in copper "neck"
$\mathbf{T_9}$	181.1	[^{o}C]	TC Ref. 9 in copper "neck"
$\mathbf{T_{10}}$	186.2	[^{o}C]	TC Ref. 10 in copper "neck"
$\mathbf{T_{11}}$	192.4	[^{o}C]	TC Ref. 11 in copper "neck"
$\mathbf{T_{peak\_1}}$	234.9	[^{o}C]	Peak Copper Temperature TC 1
$\mathbf{T_{peak\_2}}$	234.8	[^{o}C]	Peak Copper Temperature TC 2

B.3 *Slot* Configuration

Table B.16 Experimental data for Slot-*1*

	Value	Units	Description
$\dot{m}$	9.0	[g/s]	Measured Mass Flow Rate
Re	1.3E+04	[-]	Jet Reynolds Number
$\mathbf{Q_{in}}$	371.9	[W]	Nominal Power Input
$\mathbf{Q_{out}}$	337.0	[W]	Power Out = $\dot{m}\ c_p(T_{out} - T_{in})$
% Losses	9%	[-]	Heat Loss
q''_{nom}	0.22	[MW/m^2]	Nominal Incident Heat Flux
q''_{net}	0.21	[MW/m^2]	Measured Incident Heat Flux
$\mathbf{P_{rot}}$	62	[psig]	Rotameter Pressure
$\mathbf{P_{out}}$	61	[psig]	Outlet Pressure
?P	0.72	[psi]	Measured Pressure Drop
$\mathbf{T_{in}}$	22.9	[^{o}C]	Inlet Temperature
$\mathbf{T_{out}}$	59.9	[^{o}C]	Outlet Temperature
$\mathbf{T_1}$	156.6	[^{o}C]	Embedded TC Ref. 1 in brass
$\mathbf{T_2}$	159.0	[^{o}C]	Embedded TC Ref. 2 in brass
$\mathbf{T_3}$	152.4	[^{o}C]	Embedded TC Ref. 3 in brass
$\mathbf{T_4}$	152.1	[^{o}C]	Embedded TC Ref. 4 in brass
$\mathbf{T_5}$	157.5	[^{o}C]	Embedded TC Ref. 5 in brass
$\mathbf{T_6}$	169.6	[^{o}C]	TC Ref. 6 in copper "neck"
$\mathbf{T_7}$	172.7	[^{o}C]	TC Ref. 7 in copper "neck"
$\mathbf{T_8}$	175.6	[^{o}C]	TC Ref. 8 in copper "neck"
$\mathbf{T_9}$	170.2	[^{o}C]	TC Ref. 9 in copper "neck"
$\mathbf{T_{10}}$	172.3	[^{o}C]	TC Ref. 10 in copper "neck"
$\mathbf{T_{11}}$	174.9	[^{o}C]	TC Ref. 11 in copper "neck"
$\mathbf{T_{peak\_1}}$	194.8	[^{o}C]	Peak Copper Temperature TC 1
$\mathbf{T_{peak\_2}}$	194.8	[^{o}C]	Peak Copper Temperature TC 2

Table B.17 Experimental data for Slot-*2*

	Value	Units	Description
$\dot{m}$	25.7	[g/s]	Measured Mass Flow Rate
Re	3.6E+04	[-]	Jet Reynolds Number
$\mathbf{Q_{in}}$	814.4	[W]	Nominal Power Input
$\mathbf{Q_{out}}$	725.6	[W]	Power Out = $\dot{m}\ c_p(T_{out} - T_{in})$
% Losses	11%	[-]	Heat Loss
q''_{nom}	0.49	[MW/m^2]	Nominal Incident Heat Flux
q''_{net}	0.47	[MW/m^2]	Measured Incident Heat Flux
$\mathbf{P_{rot}}$	51	[psig]	Rotameter Pressure
$\mathbf{P_{out}}$	40	[psig]	Outlet Pressure
?P	7.5	[psi]	Measured Pressure Drop
$\mathbf{T_{in}}$	22.1	[^{o}C]	Inlet Temperature
$\mathbf{T_{out}}$	50.1	[^{o}C]	Outlet Temperature
$\mathbf{T_1}$	189.3	[^{o}C]	Embedded TC Ref. 1 in brass
$\mathbf{T_2}$	192.6	[^{o}C]	Embedded TC Ref. 2 in brass
$\mathbf{T_3}$	179.3	[^{o}C]	Embedded TC Ref. 3 in brass
$\mathbf{T_4}$	180.8	[^{o}C]	Embedded TC Ref. 4 in brass
$\mathbf{T_5}$	190.1	[^{o}C]	Embedded TC Ref. 5 in brass
$\mathbf{T_6}$	219.1	[^{o}C]	TC Ref. 6 in copper "neck"
$\mathbf{T_7}$	225.3	[^{o}C]	TC Ref. 7 in copper "neck"
$\mathbf{T_8}$	232.0	[^{o}C]	TC Ref. 8 in copper "neck"
$\mathbf{T_9}$	220.4	[^{o}C]	TC Ref. 9 in copper "neck"
$\mathbf{T_{10}}$	225.3	[^{o}C]	TC Ref. 10 in copper "neck"
$\mathbf{T_{11}}$	231.2	[^{o}C]	TC Ref. 11 in copper "neck"
$\mathbf{T_{peak\_1}}$	273.6	[^{o}C]	Peak Copper Temperature TC 1
$\mathbf{T_{peak\_2}}$	273.7	[^{o}C]	Peak Copper Temperature TC 2

Table B.18 Experimental data for Slot-*3*

	Value	Units	Description
$\dot{m}$	38.0	[g/s]	Measured Mass Flow Rate
Re	5.3E+04	[-]	Jet Reynolds Number
$\mathbf{Q_{in}}$	1034.2	[W]	Nominal Power Input
$\mathbf{Q_{out}}$	812.1	[W]	Power Out = $\dot{m}\, c_p(T_{out} - T_{in})$
% Losses	21%	[-]	Heat Loss
q''_{nom}	0.62	[MW/m^2]	Nominal Incident Heat Flux
q''_{net}	0.59	[MW/m^2]	Measured Incident Heat Flux
$\mathbf{P_{rot}}$	62	[psig]	Rotameter Pressure
$\mathbf{P_{out}}$	37.5	[psig]	Outlet Pressure
?P	17.0	[psi]	Measured Pressure Drop
$\mathbf{T_{in}}$	22.2	[^{o}C]	Inlet Temperature
$\mathbf{T_{out}}$	43.3	[^{o}C]	Outlet Temperature
$\mathbf{T_1}$	187.7	[^{o}C]	Embedded TC Ref. 1 in brass
$\mathbf{T_2}$	191.0	[^{o}C]	Embedded TC Ref. 2 in brass
$\mathbf{T_3}$	176.1	[^{o}C]	Embedded TC Ref. 3 in brass
$\mathbf{T_4}$	188.0	[^{o}C]	Embedded TC Ref. 4 in brass
$\mathbf{T_5}$	177.2	[^{o}C]	Embedded TC Ref. 5 in brass
$\mathbf{T_6}$	225.5	[^{o}C]	TC Ref. 6 in copper "neck"
$\mathbf{T_7}$	233.2	[^{o}C]	TC Ref. 7 in copper "neck"
$\mathbf{T_8}$	241.6	[^{o}C]	TC Ref. 8 in copper "neck"
$\mathbf{T_9}$	227.4	[^{o}C]	TC Ref. 9 in copper "neck"
$\mathbf{T_{10}}$	233.5	[^{o}C]	TC Ref. 10 in copper "neck"
$\mathbf{T_{11}}$	241.1	[^{o}C]	TC Ref. 11 in copper "neck"
$\mathbf{T_{peak\_1}}$	293.8	[^{o}C]	Peak Copper Temperature TC 1
$\mathbf{T_{peak\_2}}$	293.9	[^{o}C]	Peak Copper Temperature TC 2

Table B.19 Experimental data for Slot-*4*

	Value	Units	Description
$\dot{m}$	40.1	[g/s]	Measured Mass Flow Rate
Re	5.6E+04	[-]	Jet Reynolds Number
$\mathbf{Q_{in}}$	1242.0	[W]	Nominal Power Input
$\mathbf{Q_{out}}$	1014.7	[W]	Power Out = $\dot{m}\, c_p(T_{out} - T_{in})$
% Losses	18%	[-]	Heat Loss
q''_{nom}	0.74	[MW/m^2]	Nominal Incident Heat Flux
q''_{net}	0.71	[MW/m^2]	Measured Incident Heat Flux
$\mathbf{P_{rot}}$	65	[psig]	Rotameter Pressure
$\mathbf{P_{out}}$	39.5	[psig]	Outlet Pressure
?P	17.6	[psi]	Measured Pressure Drop
$\mathbf{T_{in}}$	22.1	[^{o}C]	Inlet Temperature
$\mathbf{T_{out}}$	47.1	[^{o}C]	Outlet Temperature
$\mathbf{T_1}$	217.3	[^{o}C]	Embedded TC Ref. 1 in brass
$\mathbf{T_2}$	221.1	[^{o}C]	Embedded TC Ref. 2 in brass
$\mathbf{T_3}$	203.5	[^{o}C]	Embedded TC Ref. 3 in brass
$\mathbf{T_4}$	205.1	[^{o}C]	Embedded TC Ref. 4 in brass
$\mathbf{T_5}$	217.5	[^{o}C]	Embedded TC Ref. 5 in brass
$\mathbf{T_6}$	262.8	[^{o}C]	TC Ref. 6 in copper "neck"
$\mathbf{T_7}$	272.0	[^{o}C]	TC Ref. 7 in copper "neck"
$\mathbf{T_8}$	282.1	[^{o}C]	TC Ref. 8 in copper "neck"
$\mathbf{T_9}$	265.1	[^{o}C]	TC Ref. 9 in copper "neck"
$\mathbf{T_{10}}$	272.6	[^{o}C]	TC Ref. 10 in copper "neck"
$\mathbf{T_{11}}$	281.7	[^{o}C]	TC Ref. 11 in copper "neck"
$\mathbf{T_{peak\_1}}$	345.0	[^{o}C]	Peak Copper Temperature TC 1
$\mathbf{T_{peak\_2}}$	345.1	[^{o}C]	Peak Copper Temperature TC 2

B.4 *Slot-45* Configuration

Table B.20 Experimental data for Slot-*45-1*

	Value	Units	Description
$\dot{m}$	9.0	[g/s]	Measured Mass Flow Rate
Re	1.3E+04	[-]	Jet Reynolds Number
$\mathbf{Q_{in}}$	369.7	[W]	Nominal Power Input
$\mathbf{Q_{out}}$	340.9	[W]	Power Out = $\dot{m}\ c_p(T_{out} - T_{in})$
% Losses	8%	[-]	Heat Loss
q''_{nom}	0.22	[MW/m^2]	Nominal Incident Heat Flux
q''_{net}	0.23	[MW/m^2]	Measured Incident Heat Flux
$\mathbf{P_{rot}}$	62	[psig]	Rotameter Pressure
$\mathbf{P_{out}}$	60	[psig]	Outlet Pressure
?P	1.5	[psi]	Measured Pressure Drop
$\mathbf{T_{in}}$	22.4	[^{o}C]	Inlet Temperature
$\mathbf{T_{out}}$	59.7	[^{o}C]	Outlet Temperature
$\mathbf{T_1}$	134.7	[^{o}C]	Embedded TC Ref. 1 in brass
$\mathbf{T_2}$	138.2	[^{o}C]	Embedded TC Ref. 2 in brass
$\mathbf{T_3}$	-	[^{o}C]	Embedded TC Ref. 3 in brass
$\mathbf{T_4}$	133.7	[^{o}C]	Embedded TC Ref. 4 in brass
$\mathbf{T_5}$	137.4	[^{o}C]	Embedded TC Ref. 5 in brass
$\mathbf{T_6}$	151.8	[^{o}C]	TC Ref. 6 in copper "neck"
$\mathbf{T_7}$	154.9	[^{o}C]	TC Ref. 7 in copper "neck"
$\mathbf{T_8}$	157.6	[^{o}C]	TC Ref. 8 in copper "neck"
$\mathbf{T_9}$	-	[^{o}C]	TC Ref. 9 in copper "neck"
$\mathbf{T_{10}}$	154.7	[^{o}C]	TC Ref. 10 in copper "neck"
$\mathbf{T_{11}}$	157.3	[^{o}C]	TC Ref. 11 in copper "neck"
$\mathbf{T_{peak\_1}}$	176.9	[^{o}C]	Peak Copper Temperature TC 1
$\mathbf{T_{peak\_2}}$	176.7	[^{o}C]	Peak Copper Temperature TC 2

Table B.21 Experimental data for Slot-*45-2*

	Value	Units	Description
$\dot{m}$	26.2	[g/s]	Measured Mass Flow Rate
Re	3.7E+04	[-]	Jet Reynolds Number
$\mathbf{Q_{in}}$	775.8	[W]	Nominal Power Input
$\mathbf{Q_{out}}$	665.2	[W]	Power Out = $\dot{m}\ c_p(T_{out} - T_{in})$
% Losses	14%	[-]	Heat Loss
q''_{nom}	0.46	[MW/m^2]	Nominal Incident Heat Flux
q''_{net}	0.45	[MW/m^2]	Measured Incident Heat Flux
$\mathbf{P_{rot}}$	73	[psig]	Rotameter Pressure
$\mathbf{P_{out}}$	60	[psig]	Outlet Pressure
?P	10.9	[psi]	Measured Pressure Drop
$\mathbf{T_{in}}$	22.3	[^{o}C]	Inlet Temperature
$\mathbf{T_{out}}$	47.4	[^{o}C]	Outlet Temperature
$\mathbf{T_1}$	145.2	[^{o}C]	Embedded TC Ref. 1 in brass
$\mathbf{T_2}$	150.9	[^{o}C]	Embedded TC Ref. 2 in brass
$\mathbf{T_3}$	-	[^{o}C]	Embedded TC Ref. 3 in brass
$\mathbf{T_4}$	141.8	[^{o}C]	Embedded TC Ref. 4 in brass
$\mathbf{T_5}$	148.7	[^{o}C]	Embedded TC Ref. 5 in brass
$\mathbf{T_6}$	178.6	[^{o}C]	TC Ref. 6 in copper "neck"
$\mathbf{T_7}$	184.4	[^{o}C]	TC Ref. 7 in copper "neck"
$\mathbf{T_8}$	189.8	[^{o}C]	TC Ref. 8 in copper "neck"
$\mathbf{T_9}$	-	[^{o}C]	TC Ref. 9 in copper "neck"
$\mathbf{T_{10}}$	184.2	[^{o}C]	TC Ref. 10 in copper "neck"
$\mathbf{T_{11}}$	189.5	[^{o}C]	TC Ref. 11 in copper "neck"
$\mathbf{T_{peak\_1}}$	227.9	[^{o}C]	Peak Copper Temperature TC 1
$\mathbf{T_{peak\_2}}$	227.5	[^{o}C]	Peak Copper Temperature TC 2

Table B.22 Experimental data for Slot-*45-3*

	Value	Units	Description
$\dot{m}$	26.0	[g/s]	Measured Mass Flow Rate
Re	3.7E+04	[-]	Jet Reynolds Number
$\mathbf{Q_{in}}$	824.9	[W]	Nominal Power Input
$\mathbf{Q_{out}}$	716.2	[W]	Power Out = $\dot{m}\ c_p(T_{out} - T_{in})$
% Losses	13%	[-]	Heat Loss
q''_{nom}	0.49	[MW/m^2]	Nominal Incident Heat Flux
q''_{net}	0.46	[MW/m^2]	Measured Incident Heat Flux
$\mathbf{P_{rot}}$	56	[psig]	Rotameter Pressure
$\mathbf{P_{out}}$	38	[psig]	Outlet Pressure
?P	14.4	[psi]	Measured Pressure Drop
$\mathbf{T_{in}}$	22.1	[^{o}C]	Inlet Temperature
$\mathbf{T_{out}}$	49.3	[^{o}C]	Outlet Temperature
$\mathbf{T_1}$	159.0	[^{o}C]	Embedded TC Ref. 1 in brass
$\mathbf{T_2}$	164.7	[^{o}C]	Embedded TC Ref. 2 in brass
$\mathbf{T_3}$	-	[^{o}C]	Embedded TC Ref. 3 in brass
$\mathbf{T_4}$	162.9	[^{o}C]	Embedded TC Ref. 4 in brass
$\mathbf{T_5}$	154.8	[^{o}C]	Embedded TC Ref. 5 in brass
$\mathbf{T_6}$	195.6	[^{o}C]	TC Ref. 6 in copper "neck"
$\mathbf{T_7}$	202.1	[^{o}C]	TC Ref. 7 in copper "neck"
$\mathbf{T_8}$	208.1	[^{o}C]	TC Ref. 8 in copper "neck"
$\mathbf{T_9}$	196.9	[^{o}C]	TC Ref. 9 in copper "neck"
$\mathbf{T_{10}}$	201.8	[^{o}C]	TC Ref. 10 in copper "neck"
$\mathbf{T_{11}}$	207.8	[^{o}C]	TC Ref. 11 in copper "neck"
$\mathbf{T_{peak\_1}}$	250.4	[^{o}C]	Peak Copper Temperature TC 1
$\mathbf{T_{peak\_2}}$	250.1	[^{o}C]	Peak Copper Temperature TC 2

B.5 *Slot-65* Configuration

Table B.23 Experimental data for Slot-*65-1*

	Value	Units	Description
$\dot{m}$	9.0	[g/s]	Measured Mass Flow Rate
Re	1.3E+04	[-]	Jet Reynolds Number
$\mathbf{Q_{in}}$	371.4	[W]	Nominal Power Input
$\mathbf{Q_{out}}$	323.3	[W]	Power Out = $\dot{m}\ c_p(T_{out} - T_{in})$
% Losses	13%	[-]	Heat Loss
q''_{nom}	0.22	[MW/m^2]	Nominal Incident Heat Flux
q''_{net}	0.23	[MW/m^2]	Measured Incident Heat Flux
$\mathbf{P_{rot}}$	62	[psig]	Rotameter Pressure
$\mathbf{P_{out}}$	60	[psig]	Outlet Pressure
?P	1.35	[psi]	Measured Pressure Drop
$\mathbf{T_{in}}$	22.8	[^{o}C]	Inlet Temperature
$\mathbf{T_{out}}$	58.2	[^{o}C]	Outlet Temperature
$\mathbf{T_1}$	110.0	[^{o}C]	Embedded TC Ref. 1 in brass
$\mathbf{T_2}$	110.3	[^{o}C]	Embedded TC Ref. 2 in brass
$\mathbf{T_3}$	103.6	[^{o}C]	Embedded TC Ref. 3 in brass
$\mathbf{T_4}$	110.8	[^{o}C]	Embedded TC Ref. 4 in brass
$\mathbf{T_5}$	113.7	[^{o}C]	Embedded TC Ref. 5 in brass
$\mathbf{T_6}$	132.2	[^{o}C]	TC Ref. 6 in copper "neck"
$\mathbf{T_7}$	135.7	[^{o}C]	TC Ref. 7 in copper "neck"
$\mathbf{T_8}$	139.0	[^{o}C]	TC Ref. 8 in copper "neck"
$\mathbf{T_9}$	134.7	[^{o}C]	TC Ref. 9 in copper "neck"
$\mathbf{T_{10}}$	136.8	[^{o}C]	TC Ref. 10 in copper "neck"
$\mathbf{T_{11}}$	139.6	[^{o}C]	TC Ref. 11 in copper "neck"
$\mathbf{T_{peak\_1}}$	159.6	[^{o}C]	Peak Copper Temperature TC 1
$\mathbf{T_{peak\_2}}$	159.7	[^{o}C]	Peak Copper Temperature TC 2

Table B.24 Experimental data for Slot-*65-2*

	Value	Units	Description
$\dot{m}$	26.0	[g/s]	Measured Mass Flow Rate
Re	3.7E+04	[-]	Jet Reynolds Number
$\mathbf{Q_{in}}$	820.3	[W]	Nominal Power Input
$\mathbf{Q_{out}}$	768.2	[W]	Power Out = $\dot{m}\ c_p(T_{out} - T_{in})$
% Losses	6%	[-]	Heat Loss
q''_{nom}	0.49	[MW/m^2]	Nominal Incident Heat Flux
q''_{net}	0.50	[MW/m^2]	Measured Incident Heat Flux
$\mathbf{P_{rot}}$	56	[psig]	Rotameter Pressure
$\mathbf{P_{out}}$	41	[psig]	Outlet Pressure
?P	10.4	[psi]	Measured Pressure Drop
$\mathbf{T_{in}}$	22.3	[^{o}C]	Inlet Temperature
$\mathbf{T_{out}}$	51.5	[^{o}C]	Outlet Temperature
$\mathbf{T_1}$	139.6	[^{o}C]	Embedded TC Ref. 1 in brass
$\mathbf{T_2}$	141.8	[^{o}C]	Embedded TC Ref. 2 in brass
$\mathbf{T_3}$	125.3	[^{o}C]	Embedded TC Ref. 3 in brass
$\mathbf{T_4}$	141.3	[^{o}C]	Embedded TC Ref. 4 in brass
$\mathbf{T_5}$	147.0	[^{o}C]	Embedded TC Ref. 5 in brass
$\mathbf{T_6}$	186.2	[^{o}C]	TC Ref. 6 in copper "neck"
$\mathbf{T_7}$	193.4	[^{o}C]	TC Ref. 7 in copper "neck"
$\mathbf{T_8}$	200.7	[^{o}C]	TC Ref. 8 in copper "neck"
$\mathbf{T_9}$	191.7	[^{o}C]	TC Ref. 9 in copper "neck"
$\mathbf{T_{10}}$	196.4	[^{o}C]	TC Ref. 10 in copper "neck"
$\mathbf{T_{11}}$	202.7	[^{o}C]	TC Ref. 11 in copper "neck"
$\mathbf{T_{peak\_1}}$	245.2	[^{o}C]	Peak Copper Temperature TC 1
$\mathbf{T_{peak\_2}}$	245.3	[^{o}C]	Peak Copper Temperature TC 2

Table B.25 Experimental data for Slot-*65-3*

	Value	Units	Description
$\dot{m}$	40.1	[g/s]	Measured Mass Flow Rate
Re	5.6E+04	[-]	Jet Reynolds Number
$\mathbf{Q_{in}}$	1034.7	[W]	Nominal Power Input
$\mathbf{Q_{out}}$	831.3	[W]	Power Out = $\dot{m}\, c_p(T_{out} - T_{in})$
% Losses	20%	[-]	Heat Loss
q''_{nom}	0.62	[MW/m^2]	Nominal Incident Heat Flux
q''_{net}	0.61	[MW/m^2]	Measured Incident Heat Flux
$\mathbf{P_{rot}}$	70.5	[psig]	Rotameter Pressure
$\mathbf{P_{out}}$	37.5	[psig]	Outlet Pressure
?P	24.4	[psi]	Measured Pressure Drop
$\mathbf{T_{in}}$	22.5	[^{o}C]	Inlet Temperature
$\mathbf{T_{out}}$	43.0	[^{o}C]	Outlet Temperature
$\mathbf{T_1}$	138.5	[^{o}C]	Embedded TC Ref. 1 in brass
$\mathbf{T_2}$	140.8	[^{o}C]	Embedded TC Ref. 2 in brass
$\mathbf{T_3}$	122.3	[^{o}C]	Embedded TC Ref. 3 in brass
$\mathbf{T_4}$	140.0	[^{o}C]	Embedded TC Ref. 4 in brass
$\mathbf{T_5}$	147.2	[^{o}C]	Embedded TC Ref. 5 in brass
$\mathbf{T_6}$	195.5	[^{o}C]	TC Ref. 6 in copper "neck"
$\mathbf{T_7}$	204.1	[^{o}C]	TC Ref. 7 in copper "neck"
$\mathbf{T_8}$	212.9	[^{o}C]	TC Ref. 8 in copper "neck"
$\mathbf{T_9}$	202.2	[^{o}C]	TC Ref. 9 in copper "neck"
$\mathbf{T_{10}}$	208.1	[^{o}C]	TC Ref. 10 in copper "neck"
$\mathbf{T_{11}}$	215.6	[^{o}C]	TC Ref. 11 in copper "neck"
$\mathbf{T_{peak\_1}}$	266.5	[^{o}C]	Peak Copper Temperature TC 1
$\mathbf{T_{peak\_2}}$	266.8	[^{o}C]	Peak Copper Temperature TC 2

Table B.26 Experimental data for Slot-*65-4*

	Value	Units	Description
$\dot{m}$	40.2	[g/s]	Measured Mass Flow Rate
Re	5.6E+04	[-]	Jet Reynolds Number
$\mathbf{Q_{in}}$	1498.9	[W]	Nominal Power Input
$\mathbf{Q_{out}}$	1189.7	[W]	Power Out = $\dot{m}\, c_p(T_{out} - T_{in})$
% Losses	21%	[-]	Heat Loss
q''_{nom}	0.90	[MW/m^2]	Nominal Incident Heat Flux
q''_{net}	0.85	[MW/m^2]	Measured Incident Heat Flux
$\mathbf{P_{rot}}$	71	[psig]	Rotameter Pressure
$\mathbf{P_{out}}$	38	[psig]	Outlet Pressure
?P	24.7	[psi]	Measured Pressure Drop
$\mathbf{T_{in}}$	22.4	[^{o}C]	Inlet Temperature
$\mathbf{T_{out}}$	51.6	[^{o}C]	Outlet Temperature
$\mathbf{T_1}$	193.7	[^{o}C]	Embedded TC Ref. 1 in brass
$\mathbf{T_2}$	192.9	[^{o}C]	Embedded TC Ref. 2 in brass
$\mathbf{T_3}$	161.1	[^{o}C]	Embedded TC Ref. 3 in brass
$\mathbf{T_4}$	184.7	[^{o}C]	Embedded TC Ref. 4 in brass
$\mathbf{T_5}$	199.9	[^{o}C]	Embedded TC Ref. 5 in brass
$\mathbf{T_6}$	267.9	[^{o}C]	TC Ref. 6 in copper "neck"
$\mathbf{T_7}$	280.6	[^{o}C]	TC Ref. 7 in copper "neck"
$\mathbf{T_8}$	293.3	[^{o}C]	TC Ref. 8 in copper "neck"
$\mathbf{T_9}$	283.1	[^{o}C]	TC Ref. 9 in copper "neck"
$\mathbf{T_{10}}$	290.9	[^{o}C]	TC Ref. 10 in copper "neck"
$\mathbf{T_{11}}$	300.9	[^{o}C]	TC Ref. 11 in copper "neck"
$\mathbf{T_{peak\_1}}$	370.7	[^{o}C]	Peak Copper Temperature TC 1
$\mathbf{T_{peak\_2}}$	370.9	[^{o}C]	Peak Copper Temperature TC 2

B.6 *Slot-100* Configuration

Table B.27 Experimental data for Slot-*100-1*

	Value	Units	Description
$\dot{m}$	9.0	[g/s]	Measured Mass Flow Rate
Re	1.3E+04	[-]	Jet Reynolds Number
$\mathbf{Q_{in}}$	372.3	[W]	Nominal Power Input
$\mathbf{Q_{out}}$	317.1	[W]	Power Out = $\dot{m}\ c_p(T_{out} - T_{in})$
% Losses	15%	[-]	Heat Loss
q''_{nom}	0.22	[MW/m^2]	Nominal Incident Heat Flux
q''_{net}	0.21	[MW/m^2]	Measured Incident Heat Flux
$\mathbf{P_{rot}}$	62	[psig]	Rotameter Pressure
$\mathbf{P_{out}}$	59	[psig]	Outlet Pressure
?P	1.7	[psi]	Measured Pressure Drop
$\mathbf{T_{in}}$	22.6	[^{o}C]	Inlet Temperature
$\mathbf{T_{out}}$	57.4	[^{o}C]	Outlet Temperature
$\mathbf{T_1}$	104.8	[^{o}C]	Embedded TC Ref. 1 in brass
$\mathbf{T_2}$	99.3	[^{o}C]	Embedded TC Ref. 2 in brass
$\mathbf{T_3}$	94.0	[^{o}C]	Embedded TC Ref. 3 in brass
$\mathbf{T_4}$	100.5	[^{o}C]	Embedded TC Ref. 4 in brass
$\mathbf{T_5}$	102.3	[^{o}C]	Embedded TC Ref. 5 in brass
$\mathbf{T_6}$	174.3	[^{o}C]	TC Ref. 6 in copper "neck"
$\mathbf{T_7}$	178.7	[^{o}C]	TC Ref. 7 in copper "neck"
$\mathbf{T_8}$	181.8	[^{o}C]	TC Ref. 8 in copper "neck"
$\mathbf{T_9}$	179.8	[^{o}C]	TC Ref. 9 in copper "neck"
$\mathbf{T_{10}}$	181.1	[^{o}C]	TC Ref. 10 in copper "neck"
$\mathbf{T_{11}}$	183.0	[^{o}C]	TC Ref. 11 in copper "neck"
$\mathbf{T_{peak\_1}}$	201.4	[^{o}C]	Peak Copper Temperature TC 1
$\mathbf{T_{peak\_2}}$	201.2	[^{o}C]	Peak Copper Temperature TC 2

Table B.28 Experimental data for Slot-*100-2*

	Value	Units	Description
$\dot{m}$	26.2	[g/s]	Measured Mass Flow Rate
Re	3.7E+04	[-]	Jet Reynolds Number
$\mathbf{Q_{in}}$	822.1	[W]	Nominal Power Input
$\mathbf{Q_{out}}$	721.9	[W]	Power Out = $\dot{m}\ c_p(T_{out} - T_{in})$
% Losses	12%	[-]	Heat Loss
q''_{nom}	0.49	[MW/m^2]	Nominal Incident Heat Flux
q''_{net}	0.47	[MW/m^2]	Measured Incident Heat Flux
$\mathbf{P_{rot}}$	57	[psig]	Rotameter Pressure
$\mathbf{P_{out}}$	37	[psig]	Outlet Pressure
?P	15.5	[psi]	Measured Pressure Drop
$\mathbf{T_{in}}$	22.6	[^{o}C]	Inlet Temperature
$\mathbf{T_{out}}$	49.9	[^{o}C]	Outlet Temperature
$\mathbf{T_1}$	137.3	[^{o}C]	Embedded TC Ref. 1 in brass
$\mathbf{T_2}$	127.7	[^{o}C]	Embedded TC Ref. 2 in brass
$\mathbf{T_3}$	159.6	[^{o}C]	Embedded TC Ref. 3 in brass
$\mathbf{T_4}$	134.8	[^{o}C]	Embedded TC Ref. 4 in brass
$\mathbf{T_5}$	130.4	[^{o}C]	Embedded TC Ref. 5 in brass
$\mathbf{T_6}$	280.7	[^{o}C]	TC Ref. 6 in copper "neck"
$\mathbf{T_7}$	290.3	[^{o}C]	TC Ref. 7 in copper "neck"
$\mathbf{T_8}$	297.0	[^{o}C]	TC Ref. 8 in copper "neck"
$\mathbf{T_9}$	293.9	[^{o}C]	TC Ref. 9 in copper "neck"
$\mathbf{T_{10}}$	296.7	[^{o}C]	TC Ref. 10 in copper "neck"
$\mathbf{T_{11}}$	300.9	[^{o}C]	TC Ref. 11 in copper "neck"
$\mathbf{T_{peak\_1}}$	340.6	[^{o}C]	Peak Copper Temperature TC 1
$\mathbf{T_{peak\_2}}$	340.3	[^{o}C]	Peak Copper Temperature TC 2

APPENDIX C

NUMERICAL DATA AND CALCULATED QUANTITIES

Appendix C provides the numerical data and calculated quantities for each option described in Section 4.6 for the array of holes test module.

C.1 Low Flow/ Low Power Test Condition

Table C.1: "Experimental" Surface Temperatures for *Holes-2*

	T_{1S} [^oC]	T_{2S} [^oC]	T_{3S} [^oC]	T_{4S} [^oC]	T_{5S} [^oC]
Surface TC	191.1	195.3	188.5	194.7	195.9

Table C.2: Numerical Data for Low Flow/Low Power SS0

Location (i)	**Units**	**1**	**2**	**3**	**4**	**5**
T_i	[^oC]	165.9	165.8	165.8	166.2	166.2
q''_{CFD_i}	[W/m^2]	170325	366457	69179	39043	148405
h_{exp_i}	[W/m^2-K]	1016	2133	419	228	861
h_{CFD_i}	[W/m^2-K]	1193	2584	483	271	1036
% Difference	[-]	15%	17%	13%	16%	17%

Table C.3: Numerical Data for Low Flow/Low Power SSV

Location (i)	Units	1	2	3	4	5
T_i	[^oC]	166.0	166.0	166.0	166.4	166.4
q''_{CFD_i}	[W/m^2]	170911	370224	68314	39275	147544
h_{exp_i}	[W/m^2-K]	1020	2155	414	229	856
h_{CFD_i}	[W/m^2-K]	1197	2608	476	273	1029
% Difference	[-]	15%	17%	13%	16%	17%

Table C.4: Numerical Data for Low Flow/Low Power SNV

Location (i)	Units	1	2	3	4	5
T_i	[^oC]	164.3	164.3	163.9	164.2	164.6
q''_{CFD_i}	[W/m^2]	160219	345331	68957	41649	138382.6
h_{exp_i}	[W/m^2-K]	956	2010	418	243	803
h_{CFD_i}	[W/m^2-K]	1135	2459	488	293	977
% Difference	[-]	16%	18%	14%	17%	18%

Table C.5: Numerical Data for Low Flow/Low Power SNVP

Location (i)	Units	1	2	3	4	5
T_i	[^oC]	164.5	164.7	164.3	164.7	164.9
q''_{CFD_i}	[W/m^2]	162239	338076	67405	39936	139740
h_{exp_i}	[W/m^2-K]	968	1968	409	233	811
h_{CFD_i}	[W/m^2-K]	1148	2399	475	280	984
% Difference	[-]	16%	18%	14%	17%	18%

Table C.6: Numerical Data for Low Flow/Low Power RNV

Location (i)	Units	1	2	3	4	5
T_i	[^oC]	167.2	167.6	166.5	166.8	167.4
q''_{CFD_i}	[W/m^2]	145945	119895	72603	45428	135004
h_{exp_i}	[W/m^2-K]	871	698	440	265	783
h_{CFD_i}	[W/m^2-K]	1012	829	505	314	934
% Difference	[-]	14%	16%	13%	16%	16%

Table C.7: Numerical Data for Low Flow/Low Power SAVV

Location (i)	Units	1	2	3	4	5
T_i	[^{o}C]	184.8	185.2	184.1	184.4	185.1
q''_{CFD_i}	[W/m^2]	129825	74114	69323	47768	121919
h_{exp_i}	[W/m^2-K]	774	431	420	279	707
h_{CFD_i}	[W/m^2-K]	802	457	429	295	751
% Difference	[-]	3%	6%	2%	5%	6%

Table C.8: Numerical Data for Low Flow/Low Power SS0L

Location (i)	Units	1	2	3	4	5
T_i	[^{o}C]	164.4	164.3	164.3	164.7	164.7
q''_{CFD_i}	[W/m^2]	168000	392520	67869	39588	147925
h_{exp_i}	[W/m^2-K]	1000	2285	412	232	859
h_{CFD_i}	[W/m^2-K]	1190	2799	479	278	1044
% Difference	[-]	16%	18%	14%	17%	18%

C.2 Medium Flow/Medium Power Test Condition

Table C.9: "Experimental" Surface Temperatures for *Holes-5*

	T_{1S} [^{o}C]	T_{2S} [^{o}C]	T_{3S} [^{o}C]	T_{4S} [^{o}C]	T_{5S} [^{o}C]
Surface TC	208.0	215.7	204.2	219.3	216.4

Table C.10: Numerical Data for Medium Flow/Medium Power SS0

Location (i)	Units	1	2	3	4	5
T_i	[^oC]	173.2	172.2	174.3	175.3	173.9
q''_{CFD_i}	[W/m^2]	462943	970400	199816	115819	403361
h_{exp_i}	[W/m^2-K]	2501	5035	1102	590	2085
h_{CFD_i}	[W/m^2-K]	3082	6699	1327	761	2709
% Difference	[-]	19%	25%	17%	22%	23%

Table C.11: Numerical Data for Medium Flow/Medium Power SNV

Location (i)	Units	1	2	3	4	5
T_i	[^oC]	179.3	178.5	179.5	180.4	179.7
q''_{CFD_i}	[W/m^2]	431411	918612	202054	124920	385975
h_{exp_i}	[W/m^2-K]	2330	4766	1115	636	1995
h_{CFD_i}	[W/m^2-K]	2800	6066	1297	794	2493
% Difference	[-]	17%	21%	14%	20%	20%

Table C.12: Numerical Data for Medium Flow/Medium Power SAVV

Location (i)	Units	1	2	3	4	5
T_i	[^oC]	212.4	212.8	211.6	212.3	212.0
q''_{CFD_i}	[W/m^2]	346956	160409	199997	131343	322828
h_{exp_i}	[W/m^2-K]	1874	832	1103	669	1668
h_{CFD_i}	[W/m^2-K]	1848	853	1064	694	1712
% Difference	[-]	-1%	2%	-4%	4%	3%

C.3 High Flow/High Power Test Condition

Table C.13: "Experimental" Surface Temperatures for *Holes-9*

	T_{1S} [°C]	T_{2S} [°C]	T_{3S} [°C]	T_{4S} [°C]	T_{5S} [°C]
Surface TC	196.0	205.3	192.0	205.7	209.8

Table C.14: Numerical Data for High Flow/High Power SS0

Location (i)	**Units**	**1**	**2**	**3**	**4**	**5**
T_i	[°C]	161.3	159.5	162.9	164.1	161.8
q''_{CFD_i}	[W/m^2]	622742	1389826	277457	164112	538750
h_{exp_i}	[W/m^2-K]	3589	7602	1637	896	2876
h_{CFD_i}	[W/m^2-K]	4623	10693	2003	1167	3966
% Difference	[-]	22%	29%	18%	23%	27%

Table C.15: Numerical Data for High Flow/High Power SSV

Location (i)	**Units**	**1**	**2**	**3**	**4**	**5**
T_i	[°C]	162.9	161.2	164.2	165.4	163.3
q''_{CFD_i}	[W/m^2]	622249	1426870	284005	166469	551060
h_{exp_i}	[W/m^2-K]	3586	7804	1675	909	2942
h_{CFD_i}	[W/m^2-K]	4566	10823	2031	1172	4014
% Difference	[-]	21%	28%	18%	22%	27%

Table C.16: Numerical Data for High Flow/High Power SSV2

Location (i)	Units	1	2	3	4	5
T_i	[^oC]	161.5	159.6	163.0	164.2	162.0
q''_{CFD_i}	[W/m^2]	611386	1460662	276490	163382	527868
h_{exp_i}	[W/m^2-K]	3524	7989	1631	892	2818
h_{CFD_i}	[W/m^2-K]	4531	11241	1994	1160	3879
% Difference	[-]	22%	29%	18%	23%	27%

Table C.17: Numerical Data for High Flow/High Power SSVP

Location (i)	Units	1	2	3	4	5
T_i	[^oC]	282.8	282.8	284.6	285.5	284.1
q''_{CFD_i}	[W/m^2]	531245	1226272	233524	128312	435255
h_{exp_i}	[W/m^2-K]	3062	6707	1378	700	2324
h_{CFD_i}	[W/m^2-K]	2069	4823	896	489	1682
% Difference	[-]	-48%	-39%	-54%	-43%	-38%

Table C.18: Numerical Data for High Flow/High Power SNV

Location (i)	Units	1	2	3	4	5
T_i	[^oC]	171.1	169.8	171.6	172.7	171.4
q''_{CFD_i}	[W/m^2]	577281	1330694	283804	177896	516506
h_{exp_i}	[W/m^2-K]	3327	7278	1674	971	2757
h_{CFD_i}	[W/m^2-K]	3988	9447	1928	1193	3546
% Difference	[-]	17%	23%	13%	19%	22%

Table C.19: Numerical Data for High Flow/High Power SNVL

Location (i)	Units	1	2	3	4	5
T_i	[^oC]	168.0	166.8	168.5	169.6	168.4
q''_{CFD_i}	[W/m^2]	577012	1327341	288007	177320	516544
h_{exp_i}	[W/m^2-K]	3326	7260	1699	968	2758
h_{CFD_i}	[W/m^2-K]	4072	9628	1999	1214	3622
% Difference	[-]	18%	25%	15%	20%	24%

Table C.20: Numerical Data for High Flow/High Power SAVV

Location (i)	Units	1	2	3	4	5
T_i	[^oC]	205.7	205.8	204.8	205.7	206.2
q''_{CFD_i}	[W/m^2]	465360	204874	275088	185648	441890
h_{exp_i}	[W/m^2-K]	2682	1121	1623	1013	2359
h_{CFD_i}	[W/m^2-K]	2584	1139	1525	2443	1019
% Difference	[-]	-4%	2%	-6%	3%	1%

BIBLIOGRAPHY

Abdel-Khalik, S. I., et al., "Thermal-Hydraulic Studies in Support of the ARIES-CS T-Tube Divertor Design," *Fusion Sci. Tech.* **54**, 864–877, 2008.

Baxi, C. B. and Wong, C. "Review of Helium Cooling for Fusion Reactor Applications". Fusion Eng. Des., **51-52**:319–324, 2000.

Beitelmal, A. H., "Analysis of an Impinging Two-Dimensional Jet," J. Heat Transfer **128**, 307-311, 2006.

Boccaccini L.V., et al. "He-cooled divertor concepts," US-Japan Workshop on Fusion Power Plants and Related Advanced Technologies, Tokyo, Japan, 11-13 Jan. 2005.

Crosatti, L., "Experimental and Numerical Investigation of Gas-Cooled Divertor Modules," Ph.D. thesis, Georgia Institute of Technology, 2008.

EFDA-JET. "Focus On: Plasma Edge," 2008. [http://www.jet.efda.org/pages/focus/plasma-edge/index.html], accessed October 2008.

FLUENT. "FLUENT 6.2 Documentation", 2004. [http://www.fluent.com], accessed October 2008.

Gardon, R. and Akfirat, J. C. "Heat transfer characteristics of impinging two-dimensional air jets". J. Heat Transfer, **88,** 101–108, 1966.

Hermsmeyer, S. and Kleefeldt, K. "Review and Comparative Assessment of Helium Cooled Divertor Concepts," FZKA 6597, 2001.

Hermsmeyer, S. and Malang, S. "Gas-cooled high performance divertor for a power plant". Fusion Eng. Des., **197**, 61–62, 2002.

Ihli, T., et al., "Design and Performance Study of the Helium-Cooled T-Tube Divertor Concept," *Fusion Eng.Des.* **82**, 249–264, 2007.

ITER. "Official ITER website", April 2008. [http://www.iter.org] accessed October 2008.

Karditas, P. and Taylor, N., "Thermal Fluid Finite Element Calculations for the European PPCs Diverto Concepts," 15th TOFE, Washington D.C., 17-21 Nov. 2002.

Kruessmann, R., et al. “Conceptual design of a he-cooled divertor with integrated flow and heat transfer promoters”. PPCS Subtask TW3-TRP-001-D2, Part II Detailed Version, FZKA 6975, 2004.

Norajitra, P., et. al, “Status of He-cooled Divertor Development (PPCS Subtask TW4-TRP-001-D2, FZKA 7100, 2005a.

Norajitra, P., et al. “Status of he-cooled divertor development”. FZKA 7100, TW4-TRP-001-D2, 2005b.

Norajitra, P., et al., “He-Cooled Divertor for DEMO: Experimental Verification of the Conceptual Modular Design,” *Fusion Eng. Des.* **81**, 341-346, 2006.

San, J. Y. and Lai, M. D. “Optimum jet-to-jet spacing of heat transfer for staggered arrays of impinging air jets”. International Journal Of Heat And Mass Transfer, **44,** 3997–4007, 2001.

San, J. Y. and Shiao, W. Z. “Effects of jet plate size and plate spacing on the stagnation Nusselt number for a confined circular air jet impinging on a flat plate”. International Journal Of Heat And Mass Transfer, **49** (19-20):3477–3486, 2006.

Sharafat, S., et al., “Ultra Low Pressure-Drop Helium-Cooled Porous Tungsten PFC,” Fusion Sci. Tech. **52**, 559-565, 2007.

Sharafat, S., UCLA, “Personal Communication,” 2007b.

Sharafat, S., UCLA, “Personal Communication,” 2008.

Stacey, W. M., J. Fusion: An introduction to the physics and technology of mag- netic confinement fusion. John Wiley & Sons, 1984.

Ultramet, “Refractory Open-Cell Foams: Carbon, Ceramic, and Metal,” Ultramet Advanced Materials Solutions, [http://ultramet.com/refractoryopencells_ceramic.html], accessed September 18, 2008.

Wang, X. R., et al., “Updates of Helium-Cooled Flat Plate Divertor Design and Analysis,” ARIES-Pathways Meeting, Madison, WI, May 28-29, [http://wwwferp.ucsd.edu/ARIES/MEETINGS/0805/Wang.pdf], accessed September 2008.

Wang, X. R., et al., “Design Optimization of High-Performance Helium-Cooled Divertor Plate Concept,” TOFE 18, San Francisco, CA, Sept. 28 – Oct. 2, 2008b.

Weathers, J.B., “Thermal Performance of Helium-Cooled Divertors for Magnetic Fusion Applications,” Master’s thesis, Georgia Institute of Technology, 2007.

Williams, B., Ultramet, "Personal Communication," 2008.